EXPLORING COMMON ARCHITECTURE OF THE BRAIN BY MULTISCALE AND MULTIMODAL FUSION

by

SHU ZHANG

(Under the Direction of Tianming Liu)

ABSTRACT

There have been significant interests in the representation of structural or functional profiles for establishment of common architecture (structural/functional correspondences) across individuals and populations in the brain mapping field. However, due to the considerable variability of structural and functional architectures in brains, it is challenging for the earlier studies to jointly represent the connectome-scale profiles to establish a common cortical architecture which can comprehensively encode both brain structure and function. To address this challenge, in this dissertation, I developed four novel computational approaches to explore the common architecture of the brain from three different scales, including landmark level, local region level and network level, respectively. Experimental results based on the four approaches demonstrated that common architecture of the brain can be successfully identified by multimodal fusion at different scales. Those common architectures have both functional and structural consistency across the subjects and those common architectures will bring new insights to understand the brain architecture and its working mechanisms, which can be further used in many neuroimaging fields, e.g., brain disease diagnosis; treatment, and follow up.

INDEX WORDS: Common architecture, Function, Structure, Multiscale, Multimodal

EXPLORING COMMON ARCHITECTURE OF THE BRAIN BY MULTISCALE AND MULTIMODAL FUSION

by

SHU ZHANG

B.E., Northwestern Polytechnical University, China, 2011

A Dissertation Submitted to the Graduate Faculty of The University of Georgia in Partial Fulfillment of the Requirements for the Degree

DOCTOR OF PHILOSOPHY

ATHENS, GEORGIA

2018

© 2018

Shu Zhang

All Rights Reserved

EXPLORING COMMON ARCHITECTURE OF THE BRAIN BY MULTISCALE AND MULTIMODAL FUSION

by

SHU ZHANG

Major Professor: Tianming Liu

Committee: Suchendra M. Bhandarkar

Qun Zhao

Electronic Version Approved:

Suzanne Barbour

Dean of the Graduate School

The University of Georgia

August 2018

DEDICATION

This work is dedicated to my family for their longstanding support. This work is also dedicated to all the researchers in the fields of brain imaging, cognitive neuroscience, psychology, psychiatry and brain mapping who needs to systematically study the common architecture of the brain.

ACKNOWLEDGEMENTS

I would like to express my sincere gratitude to my major professor, Dr. Tianming Liu. He is a scholarly mentor and beneficial friend of mine. I will remember forever the days I spent in the CAID lab under the supervising from Dr. Tianming Liu. He taught me how to do the research and how to be a real researcher. I learned that to be successful, I need hard working, optimistic attitude and never give up. These will be the principles of my life.

I would like to thank my dissertation committee: Dr. Suchendra M. Bhandarkar and Dr. Qun Zhao. Thank you very much for your insightful comments and encouragement. Their thorough guidance helps me to acknowledge how to listen, think and communicate with professional researchers and helps me to broaden my horizons in my research field.

I would like to thank all my colleagues in the CAID group and those who have contributed to this dissertation. So many precious memories came out of my mind. These memories will be my great wealth. At last, I will thank my family. Thanks for my parents, they always support me and trust me. Thanks for my wife and my daughter, your accompanying is the most important thing.

TABLE OF CONTENTS

Page

ACKNOWLEDGEMENTS v

LIST OF TABLES viii

LIST OF FIGURES ix

CHAPTER

1 INTRODUCTION AND LITERATURE REVIEW 1

1.1 Dissertation Statement 1

1.2 Contributions 4

1.3 Dissertation Outline 5

2 A JOINT REPRESENTATION OF CONNECTOME-SCALE STRUCTURAL AND FUNCTIONAL PROFILES FOR IDENTIFICATION OF CONSISTENT CORTICAL LANDMARKS IN MACAQUE BRAIN 6

2.1 Introduction 7

2.2 Materials and Methods 11

2.3 Experimental Results 26

2.4 Discussion and Conclusion 37

3 JOINT REPRESENTATION OF CONSISTENT STRUCTURAL AND FUNCTIONAL PROFILES FOR IDENTIFICATION OF COMMON CORTICAL LANDMARKS 41

3.1 Introduction 42

3.2 Materials and Methods....46
3.3 Experimental Results....54
3.4 Discussion and Conclusion....69
4 EXPLORING FIBER SKELETONS VIA JOINT REPRESENTATION OF FUNCTIONAL NETWORKS AND STRUCTURAL CONNECTIVITY....72
4.1 Introduction....73
4.2 Materials and Methods....75
4.3 Experimental Results....82
4.4 Discussion and Conclusion....89
5 DISCOVERING HIERARCHICAL COMMON BRAIN NETWORKS VIA MULTIMODAL DEEP BELIEF NETWORK....91
5.1 Introduction....92
5.2 Materials and Methods....97
5.3 Experimental Results....107
5.4 Discussion and Conclusion....118
6 DISCUSSION AND CONCLUSION....121
REFERENCES....124
APPENDICES
A SUPPLEMENTAL MATERIALS FOR CHAPTER 3....135
B SUPPLEMENTAL MATERIALS FOR CHAPTER 5....142

LIST OF TABLES

Page

Table 2.1: Interpretation of the functional peak points in the five example functional networks in Figure 2.7a using two parcellation maps (INIA19 NeuroMaps and CBCatel15).....29

Table 2.2: The average percentage of functional activity value difference of each landmark before and after optimization compared with the peak value across the six subjects in the two groups. The value is represented as mean±SD 37

Table 3.1: The locations of the 55 consistent cortical landmarks in MNI standard space (mm)...68

Table 3.2: The distributions of 55 landmarks on the brain 68

Table 3.3: The number of the landmarks for main functional behaviors.....69

Table 4.1: Similarity of fiber skeleton across the subjects using trace-map algorithm 84

Table 4.2: Similarity of local fiber patterns across the subjects through trace-map algorithm 86

Table 4.3: Average Jaccard overlap rate of functional networks which corresponding to the local fiber patterns..... 89

Table A.1: The locations of the 55 consistent cortical landmarks in MNI standard space (mm)138

Table A.2: The functions of the 55 consistent cortical landmarks in MNI standard space (mm)140

Table B.1: Correlation within group and between groups of functional connectivity maps from Figure B.5 147

LIST OF FIGURES

Page

Figure 2.1: The pipeline of the proposed computational framework of joint representation of connectome-scale structural and functional profiles for landmark identification.....12

Figure 2.2: The computational framework of dictionary learning and sparse coding of whole-brain rsfMRI signals for identification of functional brain networks. (a) The aggregated whole-brain rsfMRI signals matrix **X** of one subject. (b) The obtained dictionary matrix **D**. Each column is a dictionary atom representing the temporal pattern. (c) The obtained sparse coefficient matrix **α**. Each element of **α** represents the functional activity value. Each row of **α** can be mapped back to brain volume to represent the spatial distribution pattern of a functional network.....16

Figure 2.3: The pipeline of 'trace-map' representation of the fiber bundle of the landmark for representation of structural profile. (a) An example cortical landmark (green bubble) and the whole-brain DTI-derived axonal fibers. (b) The extracted fiber bundle of the example landmark. (c) Points distribution by projection of the principal orientation of each fiber in the fiber bundle on the unit sphere. (d) Point density (d_i) for each of 48 quasi-equal areas. (e) The 48 dimensional 'trace-map' histogram vector containing the 48-points density values. 20

Figure 2.4: Illustration of the effectiveness of the proposed landmark optimization framework based on one example landmark before and after optimization.....24

Figure 2.5: The spatial patterns of 34 examples of the identified group-wise consistent functional networks across macaque brains in the INIA19 template space. Each sub-figure (separated by dashed lines) shows one network averaged across subjects with three representative axial slices 26

Figure 2.6: 12 examples of identified group-wise consistent and common functional brain network templates (T) and the corresponding networks in three individual subjects. For each network, its spatial pattern is shown in a representative axial slice.....28

Figure 2.7: Identified consistent and common functional brain networks and the functional peak points used as initialized landmarks 30

Figure 2.8: Indices and locations of the identified 100 landmarks on one example brain. Some landmarks are hidden by the cortical surface and they are shown at the locations by black/white arrows 32

Figure 2.9: Identified 100 consistent landmarks. (a) All 100 landmarks (blue bubbles) across different subjects. (b) Eight example landmarks (represented by eight different color bubbles) shown on one example surface. (c)-(j): The fiber connection patterns of each example landmark across all subjects, respectively 33

Figure 2.10: Another three examples of landmarks and their fiber connection patterns across different subjects in (a)-(c), respectively 34

Figure 2.11: The mean correlation value of structural fiber connection 'trace-map' 35

Figure 2.12: The 100 finalized landmarks (green bubbles) and 107 initialized landmarks (red bubbles) co-visualized on one example subject brain in three views in (a)-(c), respectively 36

Figure 3.1: Conceptual illustration of joint representation of connectome-scale structural and functional profiles for identification of consistent cortical landmarks by fusing DICCCOL and HAFNI methods 45

Figure 3.2: The pipeline of the proposed computational framework. Please refer to the details of each step in the main text.....47

Figure 3.3: The 32 identified common consistent functional brain networks. Six axial slices in each row represent one functional network. The name of the network is shown on the top left. E is short for emotion task, G for gambling task, L for language task, M for motor task, R for relational task, S for social task, W for working memory task, and RS for resting state 50

Figure 3.4: Illustration of using groupwise registration for initialized landmarks. (a) Three initialized landmarks in three subjects. (b) Registered and aligned landmarks.....52

Figure 3.5: The pipeline of 'trace-map' representation for representation of structural connectivity profile of landmarks 54

Figure 3.6: Visualization of 57 consistent and common cortical landmarks in 8 subjects. Specifically, in this figure, 8 of those 57 common landmarks are highlighted with different colored circles to provide correspondences in different subject brains. 55

Figure 3.7: DTI-derived fiber bundles of those 8 highlighted landmarks (by colored circles) in Figure 3.6 for 8 subjects. Different rows (from top to bottom) correspond to the black, green, dark blue, pink, yellow, brown, purple, and light blue circles in Figure 3.6, respectively 57

Figure 3.8: Comparison between initialized landmarks and optimized landmarks. In each panel (a&b), one consistent and common cortical landmark is presented by 4 dashed

boxes, each dashed box includes one landmark example in one subject. Blue bubbles are the initialized locations of the functional peak foci, and red ones are the landmarks after the optimization. Location of landmarks are highlighted by the colored arrows 59

Figure 3.9: The locations of the landmarks before and after optimization. (a) and (b) are the two examples 62

Figure 3.10: Two examples of the landmarks before and after optimization 63

Figure 3.11: Identified consistent cortical landmarks in 28 subjects. 55 common landmarks are highlighted with dark red dots. In particular, 8 landmarks are highlighted by 8 different colored circles on the cortical surface to show the consistency of their anatomic locations 65

Figure 3.12: Shapes of fiber bundles connected to the 8 landmarks in 8 subjects. Each row represents the fiber bundles for one corresponding landmark in 8 subjects. Visualization schemes are similar to those in Figure 3.7.....66

Figure 4.1: The proposed framework of joint representation of functional networks (based on fMRI data) and structural connectivity (based on DTI data) to explore the fiber skeleton 75

Figure 4.2: The framework of applying ODL algorithm onto the fMRI signals. (A) Obtain signals from fMRI images. (B) Dictionary matrix. (C) Coefficient matrix 77

Figure 4.3: Pipeline of ‘trace-map’ representation of the fiber bundle of the landmark for representation of structural profile. (a) An example of fiber bundle and cortical surface. (b) Points distribution by projection of the principal orientation of each fiber in the fiber bundle on the uniform spherical surface. (c) 48 equally areas from

one uniform spherical surface are represented. (d) 48 vectors are used to represent one fiber bundle 80
Figure 4.4: The main skeleton of the fiber connections of one individual case. (A) The cortical surface of the brain. (B) Main skeleton of the fiber connections on level of 500. (C) Main skeleton of the fiber connections on level of 5,000. (D) Main skeleton of the fiber connections on level of 10,000 83
Figure 4.5: The main skeleton of the fiber connections of 24 subjects on level of 5000. Each main skeleton is shown separately 83
Figure 4.6: An example of the main skeleton and its local fiber patterns. (A) The main skeleton of the fiber connections. (B) 11 consistent local fiber patterns. Index of local pattern is provided 85
Figure 4.7: Local fiber patterns across the subjects 86
Figure 4.8: Local fiber pattern and its related functional networks. (A) An overview of fiber skeleton and an example of the local fiber pattern (B) Functional networks which corresponding to the local fiber patterns across the subjects. Color bar is shown on the right 87
Figure 4.9: Local fiber pattern and its related functional networks 88
Figure 4.10: Local fiber pattern and its related functional networks 88
Figure 4.11: Local fiber pattern and its related functional networks 89
Figure 5.1: The flowchart of proposed method 98
Figure 5.2: Eight examples of common brain networks obtained from DBN model layer 1. Each row represents a corresponding network from 10 subjects. The average functional consistency for all the common networks in layer 1 is 0.61 109

Figure 5.3: Eight examples of common brain networks obtained from DBN model layer 2. The average functional consistency for all the common networks in layer 2 is 0.68.....109
Figure 5.4: Eight examples of common brain networks obtained from DBN model layer 3. The average functional consistency for all the common networks in layer 3 is 0.88.....110
Figure 5.5: Examples of presenting functional and structural consistency for common brain networks. Shape of the fiber bundles is used to present the structural consistency; network overlap rates are used to present the functional consistency.....111
Figure 5.6: Two examples of hierarchical representation for specific common brain networks in top layer (layer 3). Functional and structural profiles are corresponding from left to right. A-U are networks from corresponding layers.....113
Figure 5.7: Validation of proposed algorithm by comparing the corresponding common brain networks obtained in layer 1 from two experiments 115
Figure 5.8: Comparison of DBN maps and HAFNI maps in visual function.....117
Figure 5.9: Meta-analysis results of three typical functional networks 118
Figure A.1: Two examples of the landmarks before and after optimization. (a) is corresponding to S1 network in Figure 3.3 in the main text, and (b) is corresponding to M5 network in Figure 3.3 in the main text 136
Figure A.2: Two examples of the landmarks before and after optimization. (a) is corresponding to E3 network in Figure 3.3 in the main text, and (b) is corresponding to R2 network in Figure 3.3 in the main text 137
Figure B.1: The framework of applying ODL algorithm onto the fMRI signals. (A) Obtain signals from fMRI images. (B) Dictionary matrix. (C) Coefficient matrix. 143
Figure B.2: The composition of 2800 functional networks from one subject 144

Figure B.3: The process of generating functional connectivity map for one seed vertex. (A) The location of seed vertex. (B) Selected functional networks. Yellow regions on the cortical surface are the activation areas. (C) Functional connectivity map of seed vertex. (D) Two examples about how functional connectivity maps are generated.145

Figure B.4: The process of using functional descriptor to describe functional connectivity maps. (A) Functional connectivity map and its seed vertex. (B) Project each direction on the uniform spherical surface. (C) An example of uniform spherical surface with dots. (D) Divided the surface of the unit sphere into 144 equally area (one area is shown by the purple diamond). Each area contains certain number of dots. (E) The distribution of number of dots in each area 146

Figure B.5: Three different groups of functional connectivity maps. Each group contains two similar functional connectivity maps; seed vertex is fixed and shown as the red dots... 147

Figure B.6: Validation of the functional trace-map descriptor. (A) Functional connectivity map of the seed vertex (seed vertex is shown in red square). (B) Neighborhood vertices of the seed vertex (shown in the yellow). (C) Correlation of functional trace-map between seed vertex and all other vertices from the cortex. The color bar for C is 0.5 to 1 (green to red), smaller than 0.5 is set to blue 148

CHAPTER 1

INTRODUCTION AND LITERATURE REVIEW

1.1 Dissertation Statement

After decades of active research, motivated by employing the interactional principle of brain structure and function (e.g. Passingham et al., 2002; Von, 1994), constructing a common architecture reflecting both brain structural and functional organizations across individuals and populations has been of significant interest in the brain mapping field. With the help of advanced multimodal neuroimaging techniques, we are able to quantitatively represent whole-brain structural (e.g., mapping fiber connections using diffusion tensor imaging (DTI) (Le et al., 1985; Hagmann et al., 2003; Schmahmann et al., 2007; Hagmann et al., 2008; Zhu et al., 2012a; Zhu et al., 2014a; Jiang et al., 2015b; Zhang T et al., 2016)) and functional profiles (e.g., mapping functional localizations using functional MRI (fMRI) (Ogawa et al., 1992; Belliveau et al., 1991; Calhoun et al., 2001; Beckmann et al.,2005; Calhoun et al., 2009; Lv et al., 2015a; Zhao et al., 2015; Zhang S et al., 2016; Zhao et al., 2016)) of the same brain and many efforts have been done to build common cortical landmarks of human brain. A variety of studies have attempted to construct a connectome-scale and common representation of human brain based on either structural or functional profiles. For example, previous studies have identified hundreds of cortical landmarks across different populations, each of which possesses consistent DTI-derived fiber connectivity patterns (Zhu et al., 2012a). Furthermore, functional connectome-scale brain networks have also been effectively and robustly reconstructed by using sparse learning method applied to the fMRI data (Lv et al., 2015a). Recently, multimodal fusion is becoming more and

more popular to study the brain functional and structural information simultaneously. Given the complementary information embedded in structural and functional connectomics data, it is natural and well-justified to combine multimodal information together to investigate brain connectivities and their relationships simultaneously (Chen et al., 2013; Zhu et al., 2014b). So far, based on the existing multimodal fusion studies (e.g. Zhu et al., 2014b; Sui J et al., 2012; Rykhlevskaia et al., 2008), the strongly believe is that multimodal brain connectomics research will revolutionize the fundamental understanding of the structure and function of the brain and their relationships, and eventually shed novel insights into treating, curing, and preventing many devastating brain disorders. However, due to the considerable variability of structural and functional architectures (or we can say on spatial and temporal perspectives) in human brain (Liu et al., 2011), it is very challenging to jointly represent the connectome-scale structural and functional profiles to establish a common cortical architecture for the whole brain which can comprehensively encode both brain structure and function (Zhu et al., 2014b). Thus, multimodal brain connectome analysis is still in its infancy. There is a huge barrier for researchers to further reveal the fundamental understanding of the brain structure, function and their relationships. In my view, the significant barrier is lack of an efficient framework to integrate the information from different modalities together.

Inspired by the multimodal fusion theory and our previous connectome-scale and common representation on both structural (DTI) and functional (fMRI) perspectives, in order to address abovementioned problems, I developed four novel efficient computational approaches to jointly represent connectome-scale functional and structural profiles for the identification of common architecture of the brain in this dissertation, aiming to build common architectures of the brain in multiscale based on multimodal analysis and explore the relationship between brain

structure and function at the mechanism level. In summary, there are three different scales. They are landmark scale, local region scale and network scale. For the landmark scale and local region scale, common architectures are designed, established and optimized by the integration of DICCCOL system and HAFNI system, three different novel and efficient computational approaches are proposed in the dissertation. However, for the network scale, to obtain the brain networks from the whole brain cortical vertices and identify those consistent networks across the individuals and populations, tremendous computing ability is highly demanded. Inspired by recent great success of deep learning methods and their superb computing power (Bengio et al., 2012; Goodfellow et al., 2014; Graves et al., 2013; Greff et al., 2017; He et al., 2016; He et al., 2017; Hinton 2002; Hinton 2006; Hinton et al., 2009; Hinton and Salakhutdinov 2006), several deep learning models have been developed in our group, such as 1D CNN model for fMRI time series (Huang et al., 2017), RBM and DBN models for fMRI time series data (Hu et al., 2018; Li et al., 2018), 3D CNN models for spatial brain networks, and applied them on fMRI data (Zhao et al., 2017a, Zhao et al., 2017b, Zhao et al., 2018). Our previous studies have showed that deep learning models exhibited superiority in extracting meaningful hierarchical structures from brain imaging data. Thus, a novel computational framework to learn common architectures of brain networks from multimodal fusion via Deep Belief Network (DBN) model is proposed. In total, 4 novel computational frameworks are designed to identify the common architecture of the brain from three difference scales in this dissertation.

1.2 Contributions

Common architecture of the brain is studied using multimodal fusion (combine fMRI and DTI) from three scales, which are landmark scale, local region scale and network scale, respectively.

For the landmark scale, this dissertation firstly proposed two novel computational frameworks to jointly represent connectome-scale functional and structural profiles for the identification of a set of consistent and common cortical landmarks with both reasonably accurate structural and functional correspondences across different macaque brains based on multimodal DTI and fMRI data. The second framework is designed to optimize the first proposed computational framework and make it work better for human brains and larger dataset. The solution introduces the groupwise registration algorithms into the framework.

For the local region scale, instead of studying on the landmarks, common architecture on the brain local regions are explored and highlighted from joint representation of functional and structural profiles. A novel computational framework is designed to combine functional and structural profiles together to obtain the most active fiber connection patterns. Their local fiber connection patterns and related brain regions show the common and consistent functional/structural characteristics.

For the network scale, since we know our brain works on the network level, so the aim is to obtain common networks across the subjects from the multimodalities. Thus, a novel computational framework to explore both functional and structural connectivity and thus to learn hierarchical latent features and associated representations via Deep Belief Network (DBN) model is designed.

1.3 Dissertation Outline

Chapter 1 provides background and literature review of exploring common architecture of the brain by multiscale and multimodal fusion.

Chapter 2 proposes a novel computational framework to jointly represent connectome-scale functional and structural profiles for the identification of a set of consistent and common cortical landmarks with both reasonably accurate structural and functional correspondences across different macaque brains based on multimodal DTI and fMRI data.

Chapter 3 proposes an effective computational framework, which especially works for big dataset, to jointly represent the structural and functional profiles for identification of consistent and common cortical landmarks with both structural and functional correspondences across different human brains based on DTI and fMRI data. Compared with the framework addressed in the Chapter 2, this proposed framework is regarded as a new generation solution.

Chapter 4 proposes a novel computational framework to combine functional and structural profiles together to obtain the most active fiber connection patterns, and then obtain consistent and common local fiber connections and their related brain regions.

Chapter 5 proposes a novel computational framework to explore both functional and structural connectivity on the voxel level and thus to learn hierarchical latent features and associated representations via the Deep Belief Network (DBN) model.

Chapter 6 provides the conclusion and discussion for the dissertation.

CHAPTER 2

A JOINT REPRESENTATION OF CONNECTOME-SCALE STRUCTURAL AND FUNCTIONAL PROFILES FOR IDENTIFICATION OF CONSISTENT CORTICAL LANDMARKS IN MACAQUE BRAIN[1]

[1]Shu Zhang, Xi Jiang, Wei Zhang, Tuo Zhang, Hanbo Chen, Yu Zhao, Jinglei Lv, Lei Guo, Brittany R Howell, Mar M. Sanchez, Xiaoping Hu, Tianming Liu. Joint Representation of Connectome-scale Structural and Functional Profiles for Identification of Consistent Cortical Landmarks in Macaque Brain.

Submitted to Brain Image and Behavior, October 11, 2017.

Abstract

Discovery and representation of common structural and functional cortical architectures has been a significant yet challenging problem for years. Due to the remarkable variability of structural and functional cortical architectures in human brain, it is challenging to jointly represent a common cortical architecture which can comprehensively encode both structure and function characteristics. Considering that macaque monkey brain has much less variability in structure and function compared with human brain, in this chapter, we propose a novel computational framework to apply our DICCCOL (Dense Individualized and Common Connectivity-based Cortical Landmarks) and HAFNI (Holistic Atlases of Functional Networks and Interactions) frameworks on macaque brains, in order to jointly represent structural and functional connectome-scale profiles for identification of a set of consistent and common cortical landmarks across different macaque brains based on multimodal DTI and resting state fMRI (rsfMRI) data. Experimental results demonstrate that 100 consistent and common cortical landmarks are successfully identified via the proposed framework, each of which has reasonably accurate anatomical, structural fiber connection pattern, and functional correspondences across different macaque brains. This set of 100 landmarks offer novel insights into the structural and functional cortical architectures in macaque brains.

2.1 Introduction

Representation of structural and functional profiles for the establishment of a common structural and functional cortical architecture across individuals and populations has been of significant interest in the brain mapping field. Thanks to advanced multimodal neuroimaging techniques for quantitatively representing the whole-brain structural profiles (e.g., mapping the

fiber connections using diffusion tensor imaging (DTI) (Mori and Zhang, 2006)) or the functional profiles (e.g., mapping functional localizations using functional MRI (fMRI) (Logothetis, 2008)) of the same brain, a variety of our recent studies have attempted to construct a connectome-scale, common representation of the human brain based on either structural or functional profiles (e.g., Zhu et al., 2011; Zhu et al., 2012a; Yuan et al., 2013; Li et al., 2013; Jiang et al., 2014a; Jiang et al., 2015b; Lv et al., 2015a; Lv et al., 2015b; Lv et al., 2015c; Zhang et al., 2016). For example, for the structural profiles, our previous work (Zhu et al., 2012a) successfully identified 358 consistent and common cortical landmarks across different human brains, each of which possesses group-wise consistent DTI-derived fiber connection patterns. This set of 358 landmarks was named as 'Dense Individualized and Common Connectivity-based Cortical Landmarks (DICCCOL)' (Zhu et al., 2012a). Afterwards, more constraints (e.g., anatomy identity) were integrated into the landmark identification procedure and many other meaningful landmarks were identified and named as 'anatomy-guided DICCCOL (A-DICCCOL)' (Jiang et al., 2015b). These two sets of dense landmarks are complementary and jointly represent the connectome-scale structural architecture of human brains. For the functional profiles, our recent works (Lv et al., 2015a; Lv et al., 2015b) aggregated all hundreds of thousands of fMRI (either task fMRI or resting state fMRI) signals within the whole brain of one subject into a big data matrix, and decomposed the big signal matrix into an over-complete dictionary basis matrix and a sparse reference weight matrix via an efficient and effective online dictionary learning and sparse representation framework. It has been shown that connectome-scale well-characterized functional brain networks (including both task-evoked networks and intrinsic connectivity networks) can be effectively and robustly reconstructed via the computational framework (Lv et al., 2015a; Lv et al., 2015b; Zhang et al 2013). This novel

strategy which aims to construct the connectome-scale functional architecture of human brains was named as 'Holistic Atlases of Functional Networks and Interactions (HAFNI)' (Lv et al., 2015a). In addition, there have been intensive literature studies demonstrating the close relationship between the white matter (WM) structures and gray matter (GM) functions. To extensively study the relationship between brain structure and function, fusing DTI and fMRI data has received increasing interest recently. The major advantage of multimodal data fusion studies compared with the single modality study is integrating the complimentary structural and functional information together to study the common characteristics of functional and structural profiles and revealing the common structural and functional brain architecture. However, due to the remarkable variability of structural and functional architectures in human brain (Liu 2011), it is still challenging to jointly represent the connectome-scale structural (e.g., DICCCOL) and functional (e.g., HAFNI) profiles to establish a common cortical architecture which can comprehensively encode both structure and function characteristics in human brains.

Alternatively, the macaque brain has much less variability between structure and function across different individuals compared with the human brain (e.g., Armstrong et al., 1991; Baaré et al., 2001; Chen et al., 2012; Zhang et al., 2012; Zhang et al., 2009; Zilles et al., 1988; Sereno and Tootell et al., 2005; Schoenemann et al., 2006), and it has been widely adopted as a critical nonhuman primate model to study brain structure and function (e.g., Van Essen et al., 2001; Van Essen 2004; Van Essen et al., 2011; Felleman and Van Essen 1991; Paxinos and Franklin 2004; Galletti et al. 1999; Preuss and Goldman-Rakic 1991; Lyon and Kaas 2002; Baylis et al., 1987; Kolster et al., 2009; Ferry et al., 2000). Moreover, a variety of recent studies have demonstrated the close relationship between DTI-derived fiber connections and fMRI-derived functions in macaque brains (e.g., Lee et al., 2003; Khachaturian et al., 2010; Passingham et al., 2009;

Calabrese et al., 2015; Zhang et al., 2013; Zhang D et al., 2013; Li et al., 2011). These findings directly support the neuroscience theory that each brain's cytoarchitectonic area has a unique set of extrinsic inputs and outputs, named as "connectional fingerprint" concept, which largely determines the functions of each brain area (Passingham et al., 2002). Therefore, it might be suitable and feasible to jointly represent the structural and functional profiles with multimodal DTI/fMRI data to discover common structural and functional cortical architectures in macaque brains.

Based on the above rationale, the goal of this chapter is to apply our DICCCOL and HAFNI frameworks to macaque brains to jointly represent the structural and functional profiles for identification of a set of consistent and common cortical landmarks with both reasonably good structural and functional correspondences across different macaque brains. The major contributions and novelty of this work, in comparison with prior DICCCOL and HAFNI frameworks, are as follows. First, the landmark locations are initialized in macaques with connectome-scale functional network peaks derived from HAFNI, instead of applying random initialization or manual labelling in previous studies (e.g., DICCCOL identification in human brains (Zhu et al., 2012a; Jiang et al., 2015b)). The major advantage of initializing landmark locations with functional network peaks is that it enables and facilitates the joint representation of structural connectivity and function afterwards. Since HAFNI provides dense connectome-scale functional networks and the associated functional peaks which are consistent across different subjects, it is possible that those dense functional network peaks also exhibit consistent structural connection patterns in macaque brains. Second, during the groupwise landmark location optimization procedure based on the initialized locations, meaningful anatomical identity, functional information, DTI-derived structural fiber connection pattern, and spatial

consistency constraints are integrated. These meaningful constraints ensure that the finalized landmarks with optimized locations have reasonable anatomical, structural fiber connection pattern, and functional correspondences across different macaque brains. Totally, we identified 100 consistent structural and functional landmarks and all of them have been publicly released online at: http://caid.cs.uga.edu/~szhang/dicccol.html. These dense landmarks encode the joint connectome-scale structural and functional profiles of macaque brains and shed novel insights into the regularity and variability of cortical architectures in the developing primate brain.

2.2 Materials and Methods

The framework of joint representation of connectome-scale structural and functional profiles for identification of consistent landmarks includes three major steps (marked as 1-3 in Figure 2.1): (1) representation of connectome-scale functional profiles based on resting state fMRI (rsfMRI) data for landmark location initialization (Section 2.2.2), (2) joint constraint of connectome-scale structural, functional, and anatomical profiles based on MRI/DTI data for landmark location optimization (Section 2.2.3), and (3) evaluation and determination of optimized landmark (Section 2.2.4). The section of materials and methods is organized by following these 3 major steps, respectively.

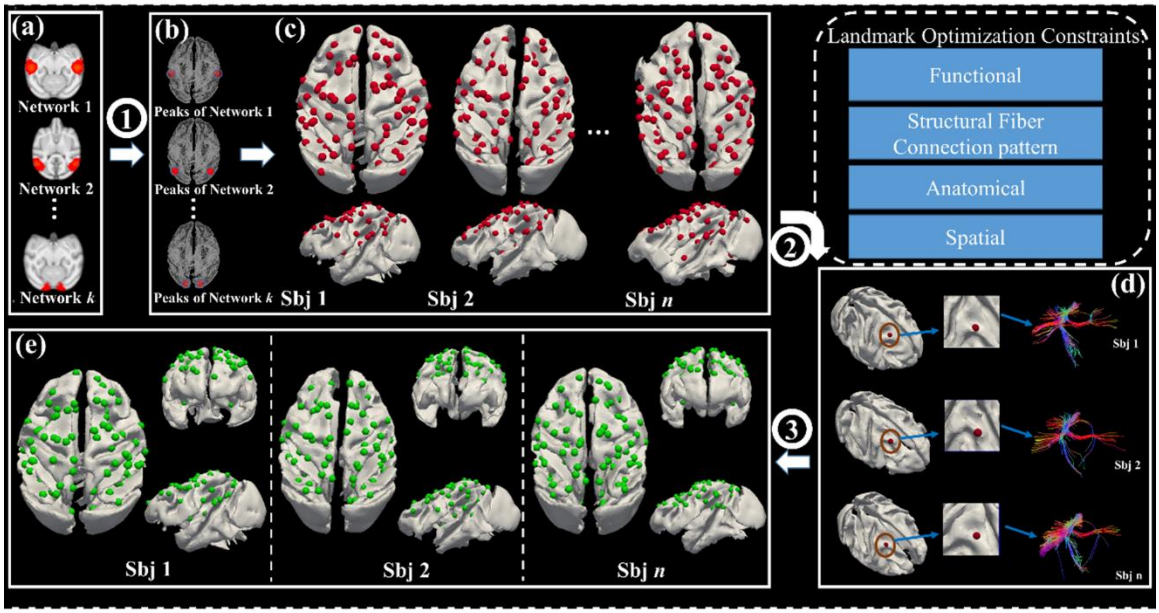

Figure 2.1. The pipeline of the proposed computational framework of joint representation of connectome-scale structural and functional profiles for landmark identification. The three major steps: representation of connectome-scale functional profiles based on resting state fMRI (rsfMRI) data for landmark location initialization (step 1), joint constraint of connectome-scale structural, functional, and anatomical profiles based on MRI and DTI data for landmark location optimization (step 2), and evaluation and determination of optimized landmark (step 3) are labeled as 1-3, respectively. (a) Identified connectome-scale group-wise consistent functional networks across individual subjects. Axial slices of spatial maps of 3 example networks in the template space are shown for illustration. (b) Identified peak foci in the components of each functional network. The peak foci of the selected illustration networks are shown in red dots. (c) All identified peak foci are mapped to individual cortical surfaces as the initial locations of landmarks (represented as red bubbles). (d) Optimization of landmark locations on cortical surfaces based on group-wise consistency of anatomy identity (gyral/sulcal regions), structural fiber connection pattern, and spatial consistency constraints. (e) Finalized consistent and common cortical landmarks (shown as green bubbles) across individual macaque brains which encode joint connectome-scale structural and functional profiles.

2.2.1 Data Acquisition and Preprocessing

The subjects were rhesus monkeys (Macaca mulatta) living in the breeding colony maintained at the Yerkes National Primate Research Center (YNPRC), at Emory University (Lawrenceville, Georgia. Six 6-month-old macaques with multimodal T1-weighted MRI, DTI and rsfMRI scans were used in this study. These subjects represent typically developing, socially-housed rhesus monkeys included in a larger study (Howell et al, 2016; McCormack et al, 2015; Shi et al, 2017). They were raised with their mothers and families for the entire duration of the study in large social groups and they span all social hierarchy strata (high, medium and low ranking families). Standard high fiber, low fat monkey chow and seasonal fruits and vegetables were provided twice daily, in parallel to enrichment items. Water was available ad libitum. All studies were performed in accordance with the Animal Welfare Act and the U.S. Department of Health and Human Services "Guide for the Care and Use of Laboratory Animals", and approved by the Emory University Institutional Animal Care and Use Committee (IACUC).

Images were acquired on a 3T Siemens Trio scanner (Malvern, PA) at the YNPRC Imaging Center using an 8-channel array, transmit and receive knee volume coil. The subjects were scanned supine under isoflurane anesthesia (standardized to the lowest possible -0.8-1% isoflurane, inhalation to minimize effects on functional connectivity). A custom-made head holder with ear bars and a mouth piece were used to secure and prevent movement of the head in order to avoid motion artifacts. Animals were intubated, administered dextrose/NaCl (I.V.) for hydration, placed over an MRI-compatible heating pad to maintain temperature and physiological measures monitored during the scans. After each subject was scanned and

completely recovered from anesthesia, it was returned to its mother, and the mother-infant dyad returned to their social group.

The neuroimaging parameters are as follows. T1-weighted MRI data were acquired with a magnetization prepared rapid gradient echo (MPRAGE) sequence with repetition time(TR)/inversion time/echo time(TE) = 3000/950/3.31 msec, flip angle = 8°, matrix is 192×192×128, and resolution is 0.6×0.6×0.6 mm^3 with 4 averages. DTI data were collected with a single-shot dual spin-echo EPI sequence with GRAPPA (R=3), b value = 1000 sec/mm^2, 62 directions of diffusion-weighting gradients, repetition time (TR)/echo time (TE) = 5000/90 msec, FOV (field of view) is 83.2×83.2 mm^2, matrix size is 64×64×43 covering the whole brain, and resolution is 1.3×1.3×1.3 mm^3 with zero gap, and 12 averages. One image without diffusion weighting (b=0 sec/mm^2) was acquired with matching imaging parameters for each average of diffusion-weighted images. The rsfMRI scans were acquired using an echo planar imaging (EPI) sequence, with TR/TE = 2060/25 msec, matrix = 85×104×65, resolution = 1.5×1.5×1.5 mm^3, and 2x15 min scans with a total volume number (time points) per scan of 400.

The preprocessing of T1-weighted MRI data includes skull stripping, motion correction, tissue segmentation, and white matter surface reconstruction via FSL (http://fsl.fmrib.ox.ac.uk) and FreeSurfer (http://surfer.nmr.mgh.harvard.edu). For DTI data, skull stripping, eddy correction, and axonal pathway orientation estimation were performed via FSL-FDT. MedINRIA (https://med.inria.fr/) was then adopted to reconstruct DTI-derived whole-brain deterministic fibers. For rsfMRI data, skull stripping, motion correction, spatial smoothing, temporal pre-whitening, slice timing correction, global drift removal, and band-pass filtering similar as those in (Mantini et al., 2011) were performed using both publicly available FSL toolkits and in-house developed tools (Li et al, 2016). We used the INIA19 macaque brain atlas (Rohlfing et al., 2012)

as the template space for anatomical reference and aligned all functional network patterns in individual fMRI spaces to this common atlas space via linear registration (using FSL-FLIRT) to identify consistent functional networks and associated peak foci. For each subject, those peak foci in the INIA19 template space were aligned and mapped onto the reconstructed cortical surface in individual MRI space via linear registration. In order to utilize the DTI-derived whole-brain deterministic fibers as structural profiles, the functional peak foci and cortical surface in individual MRI space are further aligned to individual DTI space for joint representation of the structural and functional profiles.

2.2.2 Representation of Functional Profiles for Landmark Initialization

There are two steps for the representation of connectome-scale functional profiles for landmark location initialization. First, connectome-scale group-wise consistent functional networks across individual macaque brains are identified via our recent HAFNI framework of dictionary learning and sparse coding of whole-brain rsfMRI data (Lv et al., 2015a; Lv et al., 2015b). Second, the connectome-scale functional peak foci with the largest functional activity value in each component of each functional network are identified. Those identified connectome-scale functional peak foci which have functional correspondences across different subjects are mapped to individual cortical surfaces as the initial locations of landmarks. The details of representation of the connectome-scale functional profiles are as follows.

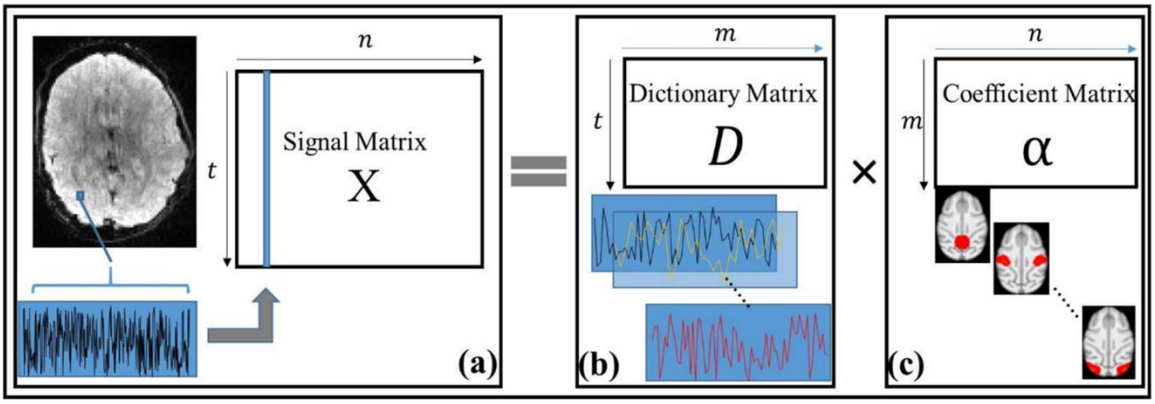

Figure 2.2. The computational framework of dictionary learning and sparse coding of whole-brain rsfMRI signals for identification of functional brain networks. (a) The aggregated whole-brain rsfMRI signals matrix **X** of one subject. (b) The obtained dictionary matrix **D**. Each column is a dictionary atom representing the temporal pattern. (c) The obtained sparse coefficient matrix **α**. Each element of **α** represents the functional activity value. Each row of **α** can be mapped back to brain volume to represent the spatial distribution pattern of a functional network.

Dictionary learning and sparse coding approaches have been successfully applied for brain fMRI time series analysis and functional brain network identification (e.g., Lee et al., 2003; Oikonomou et al., 2012; Abolghasemi et al., 2013; Zhao S et al., 2015; Zhang S et al., 2016; Jiang et al., 2014b; Jiang et al., 2015a; Jiang et al., 2015c; Lv et al., 2015a; Lv et al., 2015b). Based on our recent dictionary learning and sparse coding framework (Lv et al., 2015a; Lv et al., 2015b), the whole-brain fMRI signal matrix of a single subject can be represented as a dictionary matrix *D* and a sparse coefficient matrix *α* as illustrated in Figure 2.2. Specifically, the rsfMRI signal in each voxel of whole-brain fMRI data in one subject is extracted and normalized to zero mean and standard deviation of 1 (Lv et al., 2015b). Then the whole-brain normalized signals are arranged into a matrix $\mathbf{X} \in R^{t \times n}$ (Figure 2.2a) with n columns containing *n* rsfMRI signals from *n* voxels. *t* is the rsfMRI time points. By using the publicly available online dictionary learning

toolbox (Mairal et al., 2010), each column of X is decomposed and represented as sparse linear combination of dictionary atoms from a learned dictionary matrix D so that $\mathbf{X} = \mathbf{D} \times \boldsymbol{\alpha}$, where $\mathbf{D} \in R^{t \times m}$ is the learned dictionary matrix (m is the dictionary size) (Figure 2.2b) and $\boldsymbol{\alpha} \in R^{m \times n}$ (Figure 2.2c) is the sparse coefficient matrix. Each element of α represents the functional activity value. Each row of α can be mapped back to the brain volume as a functional brain network pattern (Figure 2.2c). According to the experience from previous study (Lv et al., 2015a), we empirically set the same m=400 for the macaque brain rsfMRI data. Moreover, once we obtain m functional brain network patterns for each single subject, we align all patterns across all subjects to the INIA19 template space via linear registration and adopt the widely used k-means clustering method to cluster all patterns in order to obtain those group-wise consistent functional brain network patterns across different subjects. Specifically, the cluster number is set as 400 which is equal to the dictionary size. After discarding those obvious noise or artifact network patterns conformed by visual inspection, k-means clustering is performed to obtain 400 clusters based on the remaining network patterns. All functional network spatial patterns within each of the 400 clusters are double checked to ensure that they have similar spatial patterns. Then we discard specific clusters based on a relatively strict criterion requiring each retained cluster to contain at least one network pattern from each subject, since we aim to identify the consistent functional brain networks across all subjects. The retained clusters are further inspected by two groups of experts to discard possible noise patterns/artifacts clusters. Those finalized clusters which are agreed by all experts are considered meaningful network patterns. Finally, the groupwise consistent functional network is obtained by averaging all network spatial patterns within each of the finalized clusters.

After identifying the connectome-scale consistent functional brain networks in the INIA19 template space, we identified the functional peak foci (voxels) with the highest functional activity value in each component of each functional network identified. As illustrated in Figure 2.1a-2.1b, we first automatically identify the functional components in each functional network by labeling the number of components of each functional network pattern using the widely adopted connected component labeling (CCL) algorithm implemented in FSL toolbox (http://fsl.fmrib.ox.ac.uk). The basic idea is that by searching the neighborhood of all voxels involved in a specific functional network, those connected voxels involved in the functional network are assigned to the same component. In this way, each functional network may have one or more components (e.g., the network 1 in Figure 2.1a has two components). Note that in order to obtain meaningful stable and consistent functional components across different subjects, we only consider those components with more than 200 connected voxels. The other components with less than 200 connected voxels are viewed as noise and discarded. Second, we identified the peak voxel with the largest functional activity value in each retained component as the representative of the component. In this way, we obtained the connectome-scale functional peak foci based on the connectome-scale consistent functional brain networks. Finally, we transformed the connectome-scale functional peak foci from the INIA19 template space to each individual MRI space using linear registration, and mapped the connectome-scale functional peak foci onto the cortical surface as mesh vertices for each individual subject. Those mapped mesh vertices derived from identified connectome-scale consistent functional brain networks via representing the functional profiles have reasonable functional correspondences across different subjects and serve as the initial locations of cortical landmarks for the next step of optimization.

2.2.3 Joint Constraint of Structural and Functional Profiles for Landmark Optimization

In this chapter, the structural profile is represented as the 'trace-map' of DTI-derived fiber bundles (Zhu et al., 2012b; Chen et al., 2013; Jiang et al., 2015b). To be self-contained, here the 'trace-map' representation and comparison of the DTI-derived structural fiber connection pattern is briefly demonstrated. As illustrated in Figure 2.3, for each landmark which is represented as a sphere centered at a mesh cortical vertex with a predefined radius (empirically defined as 5.5 mm in this chapter) (Zhu et al., 2012a; Jiang et al., 2015b) (Figure 2.3a), we extract the DTI-derived fiber bundle passing through the sphere (Figure 2.3b), which represents the structural fiber connection pattern of this landmark. In order to quantify the shape of the fiber bundle and compare the fiber bundles across different landmarks, we adopt our 'trace-map' model (Chen et al., 2013; Zhu et al., 2012b) to represent the fiber bundle with a 48-dimensional vector. Specifically, the principal orientation of each fiber in the fiber bundle is firstly projected onto the standard surface of a unit sphere (Figure 2.3c). The global shape information of the fiber bundle is represented as the points distributed on the unit sphere. Then, the surface of the unit sphere is segmented into 48 quasi-equal areas with a diamond shape (Figure 2.3d) (Gorski et al., 2005). The number of points in each area are counted to calculate distribution density. A 48 dimensional histogram vector $tr = [d_1, d_2 \dots d_{48}]$ containing the 48 point density values, namely 'trace-map' (Figure 2.3e), is finally obtained as the structural profile of a landmark. As a result, the comparison between complicated shapes of fiber bundles is effectively converted to the comparison of the similarity of two 48 dimensional trace-map vectors. More details are referred to (Chen et al., 2013; Zhu et al., 2012a). The DTI-derived structural fiber connection profile similarity will be integrated into the procedure landmark optimization as a constraint.

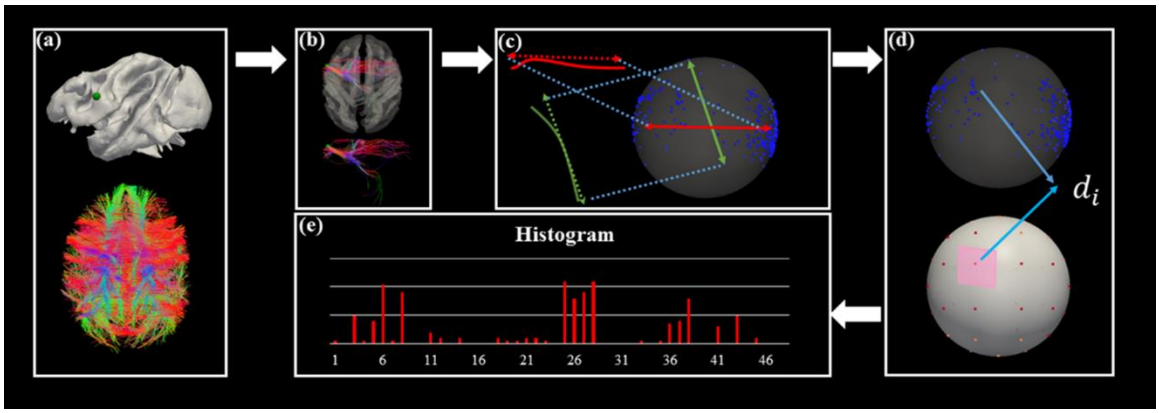

Figure 2.3. The pipeline of 'trace-map' representation of the fiber bundle of the landmark for representation of structural profile. (a) An example cortical landmark (green bubble) and the whole-brain DTI-derived axonal fibers. (b) The extracted fiber bundle of the example landmark. (c) Points distribution by projection of the principal orientation of each fiber in the fiber bundle on the unit sphere. (d) Point density (d_i) for each of 48 quasi-equal areas. (e) The 48 dimensional 'trace-map' histogram vector containing the 48-points density values.

Based on the initial landmarks derived from identified connectome-scale consistent functional brain networks (Section 2.2.2), we optimize their locations via integrating meaningful anatomical, functional, structural fiber connection pattern, and spatial consistency constraints so that the optimized landmarks possess anatomical, structural fiber connection pattern, and functional correspondences across different macaque brains. Specifically, we search all possible combinations of candidate landmark locations (cortical mesh vertices) within their local morphological neighborhoods across different subjects, and seek the optimal solution of the combination of landmark locations across subjects under the following four constraints. First, as demonstrated in Section 2.2.2, since each set of corresponding landmarks across different subjects are initialized by the common functional network peaks, the functional activity values of the corresponding landmarks should not decrease much compared with the peak value after optimization to retain the functional consistency. Second, the corresponding landmarks across

different subjects should have maximally similar DTI-derived fiber connection pattern after optimization to retain the structural consistency (Zhu et al., 2012a; Jiang et al., 2015b). Third, the corresponding landmarks across different subjects should locate on the same gyral/sulcal regions after optimization to preserve the macro-anatomical identity (Jiang et al., 2015b). Fourth, the corresponding landmarks should move within a small size of the morphological neighborhood of their initial locations after optimization to preserve the globally spatial correspondence (Zhu et al., 2012a; Jiang et al., 2015b). These constraints are jointly modeled as an energy minimization problem. Note that we perform landmark optimization for each corresponding landmark separately. In this chapter, we argue that 4-ring neighbor size is suitable for the macaque brain in this study due to the following two main reasons. First, in our previous DICCCOL paper in human brains (Zhu et al., 2012a), we used 5-ring neighbor size which comes up about 30 candidate vertices. Such searching area size was demonstrated to be guaranteed for the optimal landmark identification (Zhu et al., 2012a). In this work, considering the relatively smaller size of macaque brain compared with human brain and to maintain the anatomical consistency, we used 4-ring neighbor size which also comes up more than 30 candidate vertices, which guarantee the identification of optimal landmarks on macaque brains. It is not always better to enlarge the search area since large search area will lead to the inconsistent anatomical information of the landmark, i.e., the landmarks will locate on different gyral/sulcal areas. The second one is the computing cost. Since the optimal landmark location combination across different individual brains is searched at the group level, the computing cost will increase exponentially with the number of rings of search area increasing. In conclusion, 4-rings is suitable in this work.

Specifically, we assume v_{0i}^{p} is the initial location of landmark p in subject i (i=1..N), v_i^p is the set of candidate locations within the morphological neighborhood $C_{v_{0i}^{p}}$ of v_{0i}^{p} ($v_i^p \in C_{v_{0i}^{p}}$),

the functional activity value of v_{0i}^{p} is $z_{v_{0i}^{p}}$ (peak value), and the functional activity value of v_i^p is $z_{v_i^p}$. In this work, we consider 4-ring neighbors of v_{0i}^{p}, i.e., about 30 mesh vertices as the candidate locations for optimization of landmark *p* in subject *i*. First, the landmark can only move within the neighborhood, i.e., $v_i^p \in C_{v_{0i}^{p}}$, and it is used as the spatial constraint. Second, in order to retain the functional consistency, the difference between $Z_{v_{0i}^{p}}$ and $Z_{v_i^p}$ should be small, i.e., $(Z_{v_{0i}^{p}} - Z_{v_i^p})/Z_{v_{0i}^{p}} \leq \lambda$. Third, the principal curvature value of v_i^p is noted by $pcurv_{v_i^p} \begin{cases} \geq 0, \ p \in gyrus \\ < 0, \ p \in sulcus \end{cases}$, and $pcurv_{v_i^p} \times pcurv_{v_j^p} \geq 0$ of a corresponding landmark between subject *i* and *j* is used as the anatomical constraint. The rationale is that since we can obtain the gyral/sulcal information of a specific initialized landmark according to its location in the INIA19 template space (Section 2.2.2), the corresponding landmarks mapped to all subjects should preserve the same gyral/sulcal information during landmark optimization. Finally, we define the structural fiber connection pattern similarity constraint $E_s(p)$ (Zhu et al., 2012a; Jiang et al., 2015b) for landmark *p* as

$$E_s(p) = 1 - \frac{\sum_{i,j=1\ldots k\ldots N, i\neq j} corr\left(\boldsymbol{tr}(v_i^p), \boldsymbol{tr}(v_j^p)\right)}{N * (N-1)} \tag{2-1}$$

Where corr(.) is the Pearson's correlation value between the 'trace-map' vectors of vertices v_i^p and v_j^p in subject *i* and *j*, respectively. *N* is the total number of subjects. The group-wise variance of the four jointly modeled constraints is then mathematically represented as the energy *E*:

$$E(p) = 1 - \frac{\sum_{i,j=1\ldots k\ldots N, i\neq j} corr\left(\boldsymbol{tr}(v_i^p), \boldsymbol{tr}(v_j^p)\right)}{N * (N-1)} \tag{2-2}$$

$$s.t.\frac{Z_{v_0{}_k^p} - Z_{v_k^p}}{Z_{v_0{}_k^p}} \leq \lambda, v_k^p \in v_0{}_k^p, pcurv_{v_i^p} \times pcurv_{v_j^p} \geq 0$$

Our aim is to minimize the energy $E(p)$:

$$\min_{i,j \in C,\ i \neq j, pcurv_{v_i^p} \times pcurv_{v_j^p} \geq 0} 1 - \frac{\sum_{i,j=1 \ldots k \ldots N, i \neq j} corr\left(\boldsymbol{tr}(v_i^p), \boldsymbol{tr}(v_j^p)\right)}{N * (N-1)} \tag{2-3}$$

Where the constraint $C = \{k | k = 1..N, s.t. (Z_{v_0{}_k^p} - Z_{v_k^p})/Z_{v_0{}_k^p} \leq \lambda, v_k^p \in v_0{}_k^p\}$

The details of solving Eq. (2-3) are as follows. For each iteration, we search all possible combinations of candidate landmark locations across all subjects for landmark *p*, and find an optimal combination of landmark locations which has a minimum $E(p)$. If the Euclidean distance between the landmark locations with minimum $E(p)$ of two consecutive iterations across all subjects is less than or equal to a threshold *ε*, the iterations are stopped. We set *ε* =2mm since the Euclidean distance of two adjacent cortical mesh vertices is around 2 mm. We empirically set λ=50%. The whole procedure will stop once convergence. Note that since we perform landmark optimization for each corresponding landmark across different subjects separately, we check the Euclidean distance between two neighboring optimized landmarks in each single subject. If the distance is less than or equal to *ε* =2mm across all single subjects, these two landmarks are considered as merged and only one landmark is retained.

Figure 2.4 illustrates the effectiveness of the proposed landmark optimization framework based on one example landmark. Figure 2.4a shows the fiber connection patterns of one corresponding optimized landmark in two example subjects. Figure 2.4b shows the locations of the same corresponding optimized landmarks on the surfaces of the two subjects. Figure 2.4c-2.4d illustrate the fiber connection patterns and locations of the corresponding landmark of a third subject before and after optimization. After integrating the fiber connection pattern

similarity constraint, the optimized landmark has better fiber connection pattern similarity than that before optimization (Figure 2.4c) compared with Figure 2.4a. After integrating anatomical constraint, the optimized landmark is from gyral region to sulcal region (Figure 2.4d) which is identical to that of other subjects in Figure 2.4b. Moreover, Figure 2.4e shows the locations of the same corresponding landmark in the functional volume space before and after optimization. We can see that from visual inspection the functional activity value after optimization does not decrease much compared with the peak point of initialized landmark.

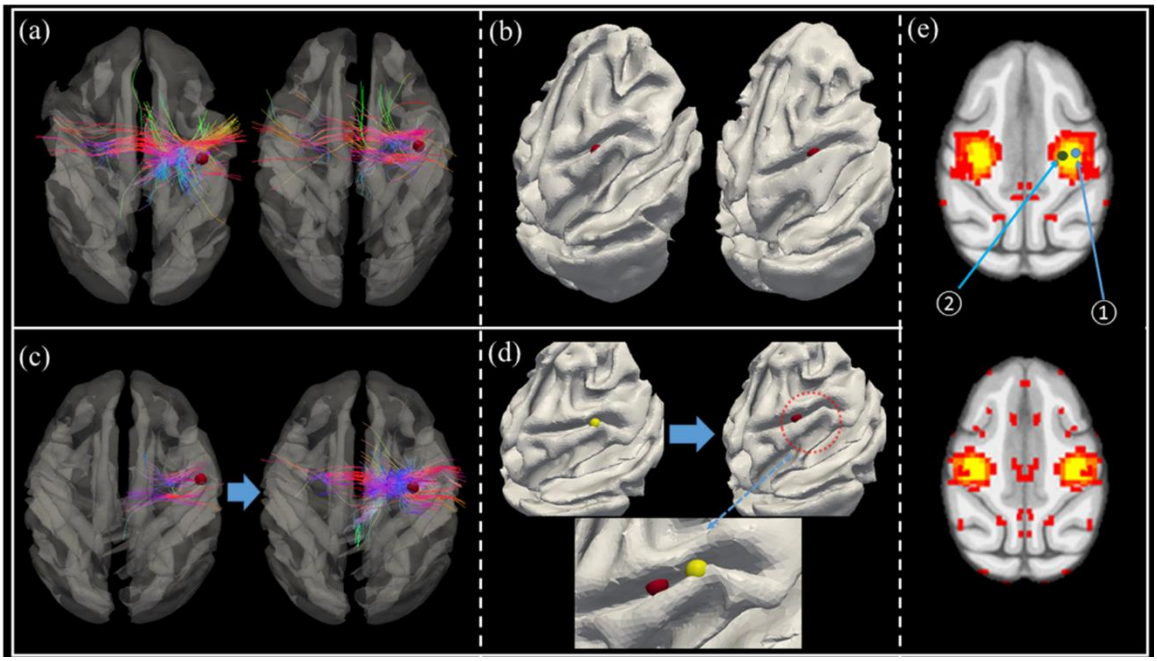

Figure 2.4. Illustration of the effectiveness of the proposed landmark optimization framework based on one example landmark before and after optimization. (a) The fiber connection patterns of one corresponding optimized landmark (red bubble) in two example subjects. (b) The locations of the same corresponding optimized landmarks on the surfaces of the two subjects. (c) The fiber connection pattern of the corresponding landmark of a third subject before and after optimization. The left one is before the optimization and the other one is after the optimization. (d) The locations of the corresponding landmark of a third subject before (yellow bubble) and after (red bubble) optimization. (e) The locations of the same corresponding landmark in the functional volume space before (1) and after (2) optimization.

2.2.4 Consistent Landmarks Inspection and Determination

In order to identify those optimized landmarks which truly jointly encode the connectome-scale structural and functional profiles, we randomly separated all six available subjects into two groups (four individuals per group; two subjects are in both groups in order to examine the stability and reproducibility of landmark optimization, so six subjects and eight individuals in total), and perform the landmark optimization scheme in Section 2.2.3 for the two groups separately. In this way, two independent groups of optimized corresponding landmarks are obtained. Then, we determine those common and consistent landmarks which are reproducible across the two groups of subjects via both quantitative and qualitative measurements similar as those in (Zhu et al., 2012a; Jiang et al., 2015b). Specifically, for each corresponding landmark, we calculated the functional activity value difference and 'trace-map' correlation as discussed in Section 2.2.3 across all subjects in both groups to check the functional and structural consistency. If the value is statistically different (two-sample t-test, $p=0.05$) between two groups, this landmark will be considered instable and discarded (Zhu et al., 2012a; Jiang et al., 2015b). Moreover, we adopted in-house visualization tool (Li et al., 2012) to visually examine the anatomical identity and spatial consistency of corresponding landmarks across all subjects in the two groups by two independent groups of experts. In details, there are two major criteria for the visual examination of anatomical identity and spatial consistency. The first one is to check the consistency of spatial locations (within the same reasonable anatomical region) of the identified corresponding common landmarks across different subjects. The second one is to double check whether all the corresponding landmarks are located on the same gyri/sulci or not. These steps are checked by the experts as the final inspection. Those finally retained landmarks agreed by all experts have reasonably consistent anatomical, structural, and functional profiles

across different subjects. The finalized landmarks reasonably encode the joint representation of connectome-scale structural and functional profiles.

2.3 Experimental Results

2.3.1 Connectome-scale Consistent Functional Networks

Based on the methods described in Section 2.2.2, 70 group-wise consistent and common functional brain networks across different subjects are successfully identified. Figure 2.5 shows the spatial patterns of 34 examples of the identified groupwise consistent functional networks in the INIA19 template space. The spatial patterns of all 70 consistent functional networks are publicly released online at: http://hafni.cs.uga.edu/MonkeyNewICNs/MonkeyBrain_NewTemplateComponentsMap_Shu_presentation.html.

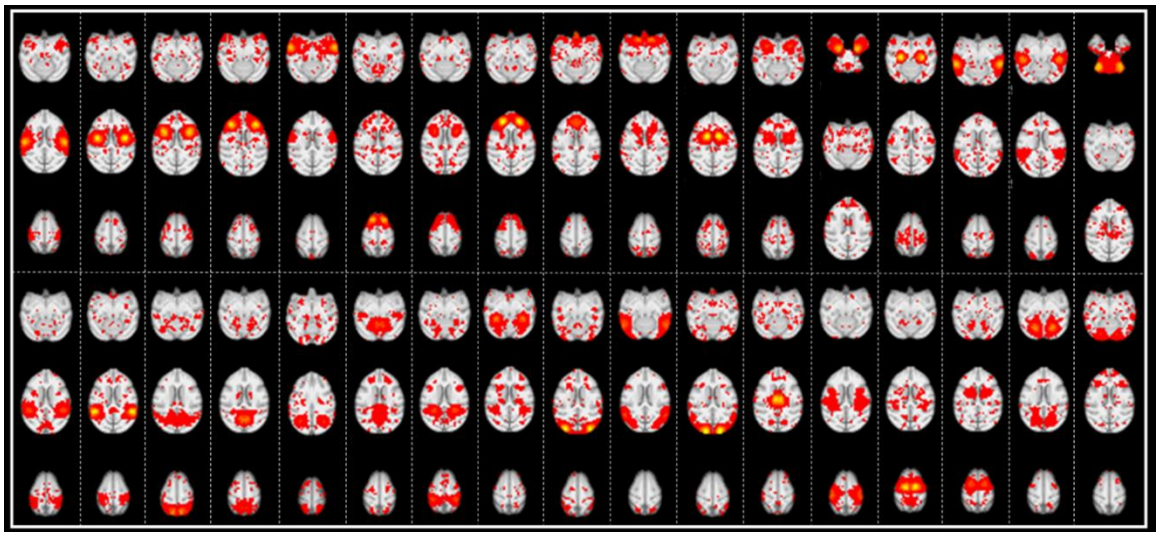

Figure 2.5. The spatial patterns of 34 examples of the identified group-wise consistent functional networks across macaque brains in the INIA19 template space. Each sub-figure (separated by dashed lines) shows one network averaged across subjects with three representative axial slices.

Figure 2.6 shows the spatial patterns of 12 examples of the corresponding identified functional brain networks in the template space and in individuals. Another five examples are shown in Figure 2.7a. All the consistent functional networks are released online at: http://hafni.cs.uga.edu/MonkeyNewICNs/MonkeyBrain_NewTemplateComponentsMap_Shu_presentation.html. The results are organized with 7 columns, in which templates are shown on the first column and the other six columns are representing the identified individual networks. By visual inspection, each functional network shows reasonably consistent spatial pattern across different subjects. Quantitatively, the spatial pattern similarity is measured as the spatial overlap rate R(S,G) between the functional network spatial pattern of a specific subject (S) and the corresponding group-averaged spatial pattern template (G):

$$R(S,G) = \frac{|S \cap G|}{|G|} \tag{2-4}$$

Note that S and G are converted from continuous values to discrete labels (all values smaller than or equal to 0 are labeled as 0, and others are labeled as 1). The mean spatial overlap rate of all 70 functional networks across all subjects is as high as 0.336.

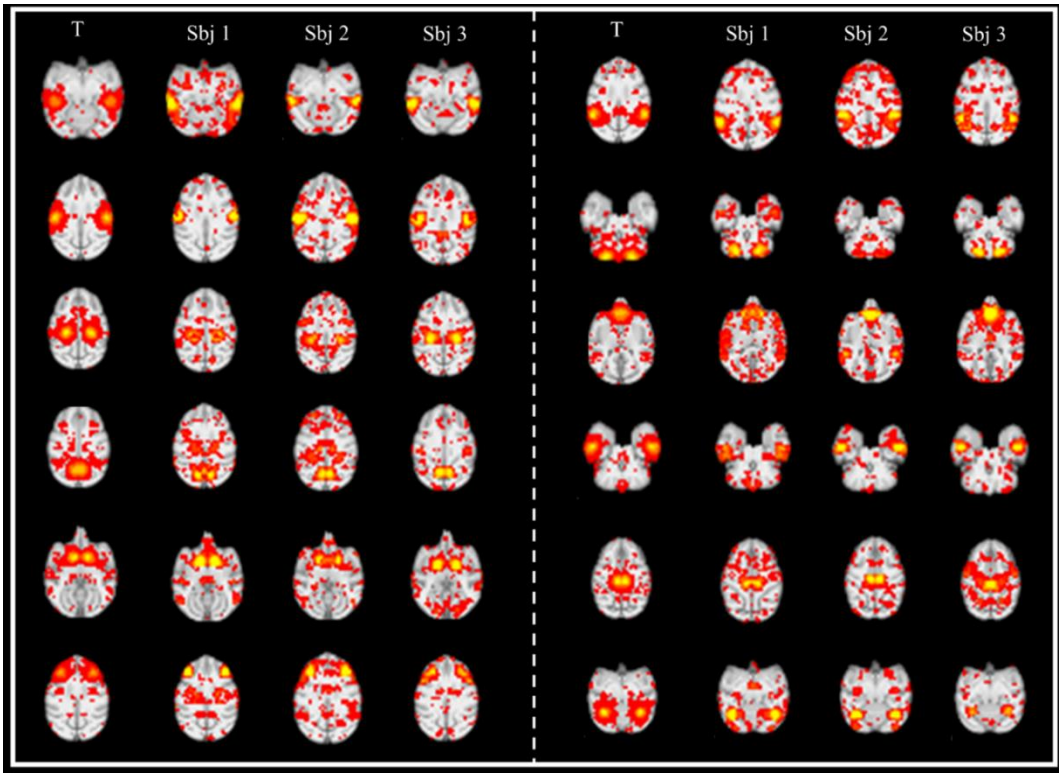

Figure 2.6. 12 examples of identified group-wise consistent and common functional brain network templates (T) and the corresponding networks in three individual subjects. For each network, its spatial pattern is shown in a representative axial slice.

Based on the 70 connectome-scale functional network patterns, 107 connectome-scale and consistent functional peak points were identified and mapped to individual cortical surfaces as the initialized landmarks. Figure 2.7a shows the identified functional peak points and the mapped landmarks derived from five example functional networks, respectively. We can see that the corresponding landmarks have rough correspondences on the cortical surfaces across different subjects. Figure 2.7b shows all 107 initialized landmarks in the six macaque brains based on the 107 connectome-scale and consistent functional peak points. As a preliminary step, we interpret the 107 connectome-scale and consistent functional peak points using two publicly available parcellation maps: INIA19 NeuroMaps (Rohlfing et al., 2012) and CBCatel15

(Calabrese et al., 2015), since they provide relatively finer-scale brain parcellations (Rohlfing et al., 2012; Calabrese et al., 2015). Table 2.1 shows the interpretations of the functional peak points based on the five example functional networks in Figure 2.7a.

Table 2.1. Interpretation of the functional peak points in the five example functional networks in Figure 2.7a using two parcellation maps (INIA19 NeuroMaps and CBCatel15).

Network	**No. of landmarks**	**INIA19 NeuroMaps**	**CBCatel15**
#1	2	l_occipital_white_matter; r_occipital_white_matter	parietal area PE; parietal area PEa
# 2	2	l_superior_temporal_gyrus; r_superior_temporal_gyrus	parietal area PF, opercular part ; parietal area PF (cortex)
# 3	2	l_cerebral_white_matter; r_cerebral_white_matter	depth intraparietal area; dorsal parietal area
# 4	2	l_frontal_white_matter; r_frontal_white_matter	occipitoparietal area; dorsal parietal area
# 5	2	l_inferior_temporal_gyrus; r_inferior_temporal_gyrus	parietal area PG; parietal area PFG

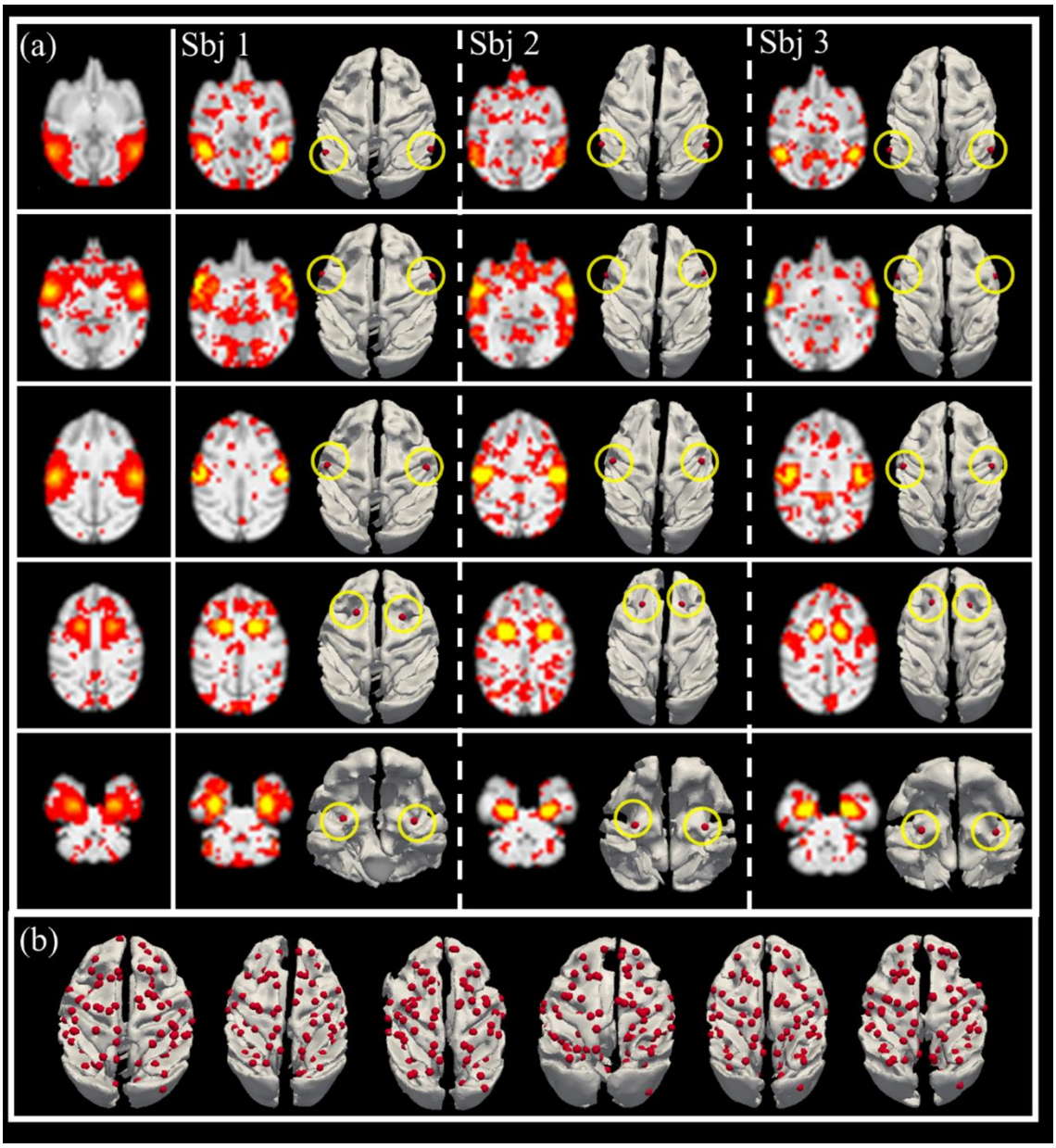

Figure 2.7. Identified consistent and common functional brain networks and the functional peak points used as initialized landmarks. (a) Five examples of functional brain networks. Each row shows the spatial pattern of one functional network template and the corresponding spatial patterns in three example individual brains. The identified functional peak points mapped onto individual surfaces are represented as red bubbles and highlighted by yellow circles. (b) All 107 initialized landmarks based on the 107 connectome-scale and consistent functional peak points in the six macaque brains.

2.3.2 Consistent Cortical Landmarks via Joint Representation of Connectome-scale Structural and Functional Profiles

We jointly represented the connectome-scale structural and functional profiles for identification of the consistent cortical landmarks as demonstrated in Sections 2.2.3 and 2.2.4. In total, we identified 100 consistent and common landmarks across subjects. The indices and locations of these 100 landmarks are shown in Figure 2.8. Figure 2.9a shows all 100 landmarks across all subjects in the two groups. We randomly selected eight example landmarks (Figure 2.9b) and visualized their fiber connection patterns in Figure 2.9c-2.9j, respectively. From visual inspection, we can see that the fiber connection pattern of the corresponding landmark is similar across different subjects. Quantitatively, the mean correlation value of 'trace-map' (Eq. (2-1)) across any pair of the eight individuals in two groups is 0.667, 0.677, 0.785, 0.768, 0.8041, 0.8247, 0.8151, and 0.6147 for the eight example landmarks, respectively. Figure 2.10 shows another three example landmarks and their fiber connection patterns. The visualization of all 100 landmarks is released at: http://caid.cs.uga.edu/~szhang/dicccol.html. All fiber connection patterns of 100 landmarks across different subjects are at: http://caid.cs.uga.edu/~szhang/fiber.html. The mean correlation value of 'trace-map' across any pair of the eight individuals in two groups for all 100 landmarks in shown in Figure 2.11(a). The overall mean correlation value of all 100 landmarks is 0.71. In conclusion, the 100 landmarks possess reasonably consistent structural profiles (DTI-derived fiber connection pattern) across different subjects. The functional, anatomical, and the spatial consistency of the 100 landmarks will be discussed in detail in the next section.

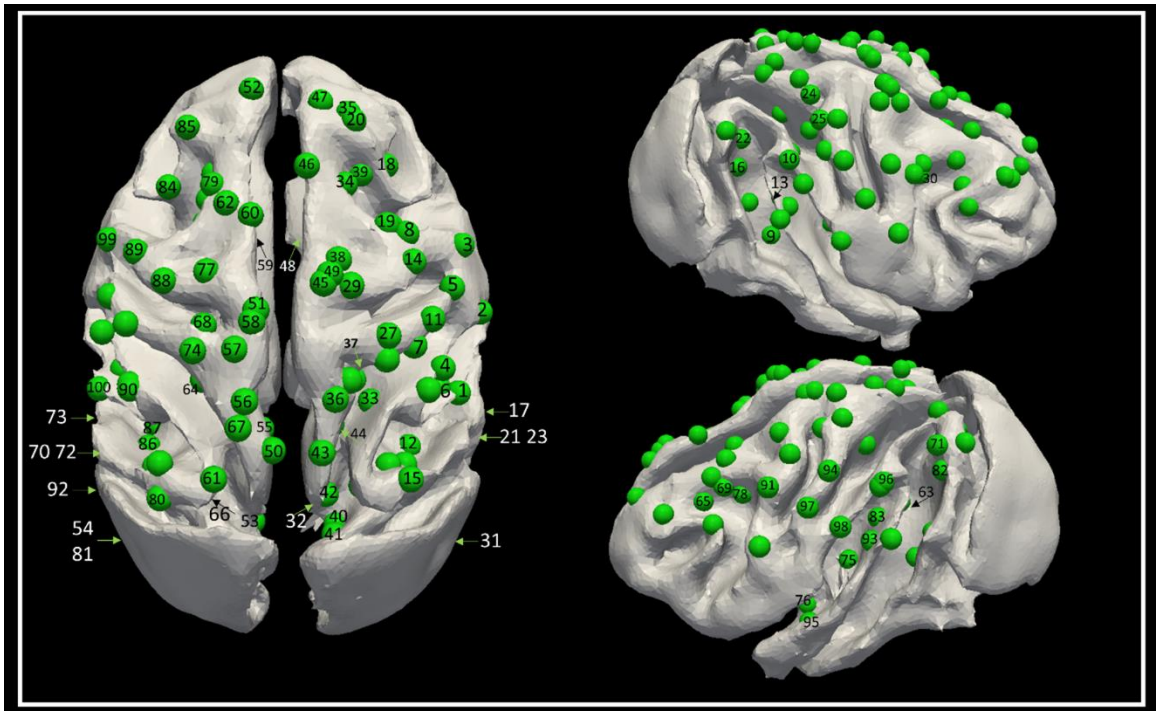

Figure 2.8. Indices and locations of the identified 100 landmarks on one example brain. Some landmarks are hidden by the cortical surface and they are shown at the locations by black/white arrows.

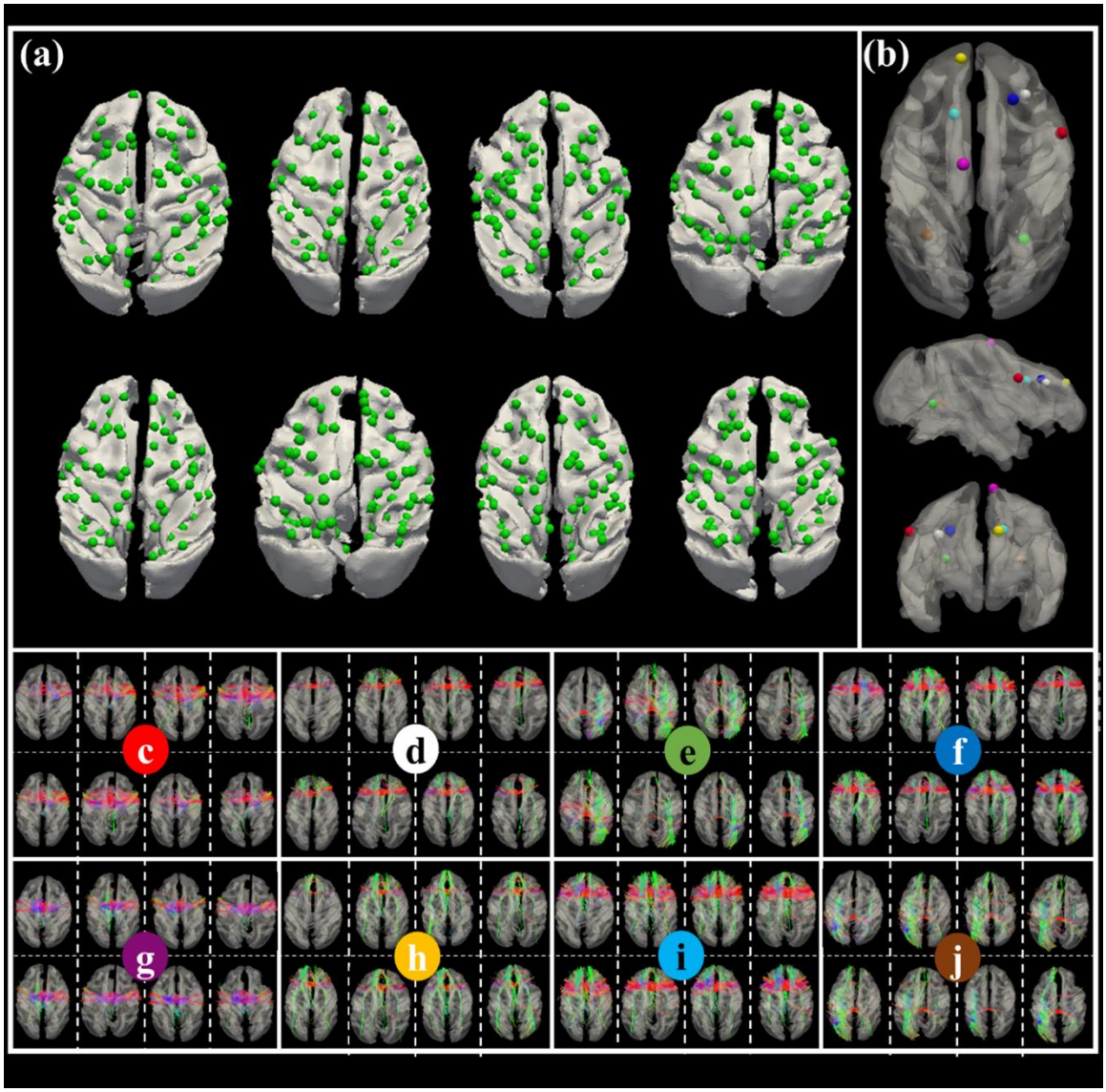

Figure 2.9. Identified 100 consistent landmarks. (a) All 100 landmarks (blue bubbles) across different subjects. (b) Eight example landmarks (represented by eight different color bubbles) shown on one example surface. (c)-(j): The fiber connection patterns of each example landmark across all subjects, respectively.

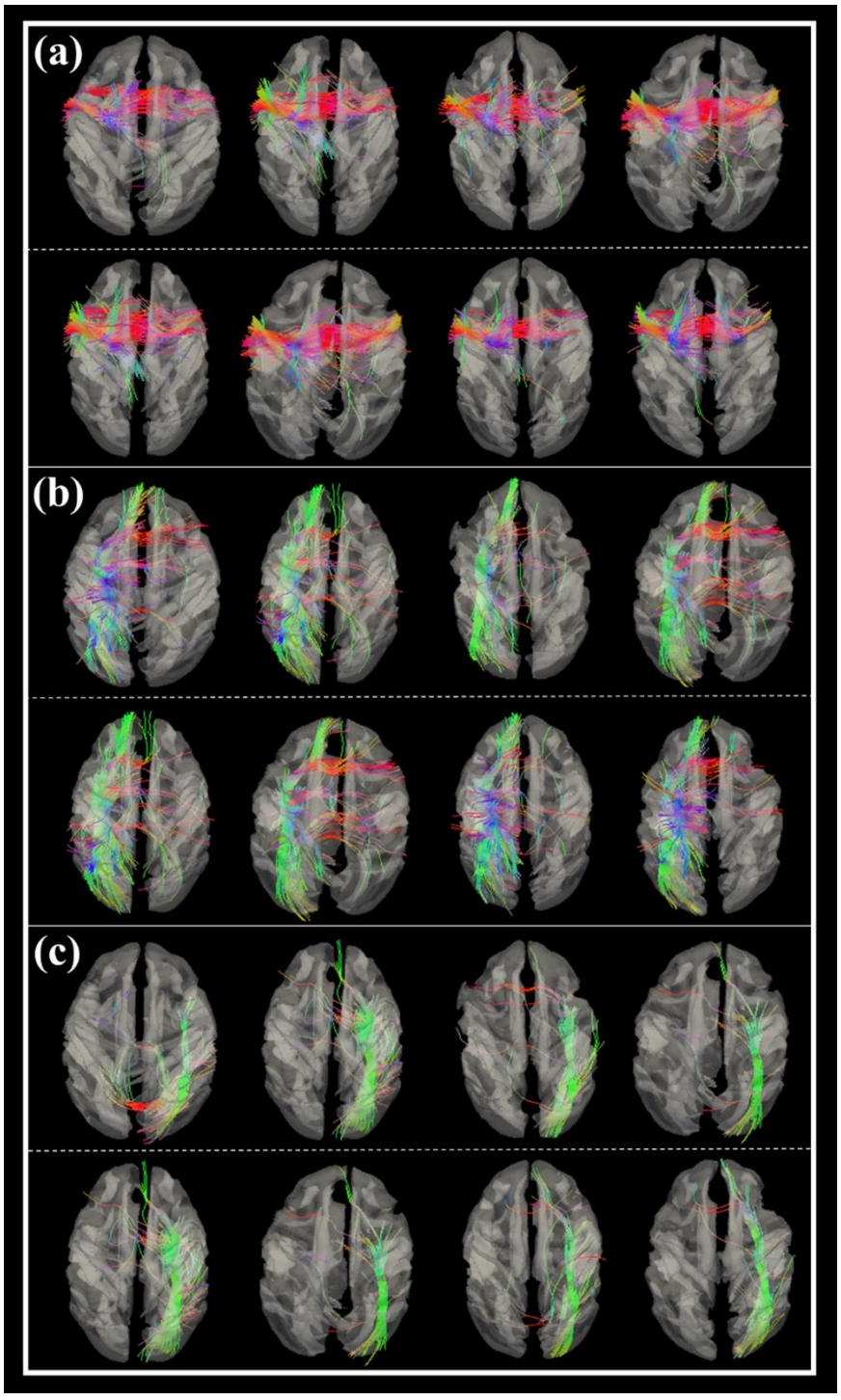

Figure 2.10. Another three examples of landmarks and their fiber connection patterns across different subjects in (a)-(c), respectively.

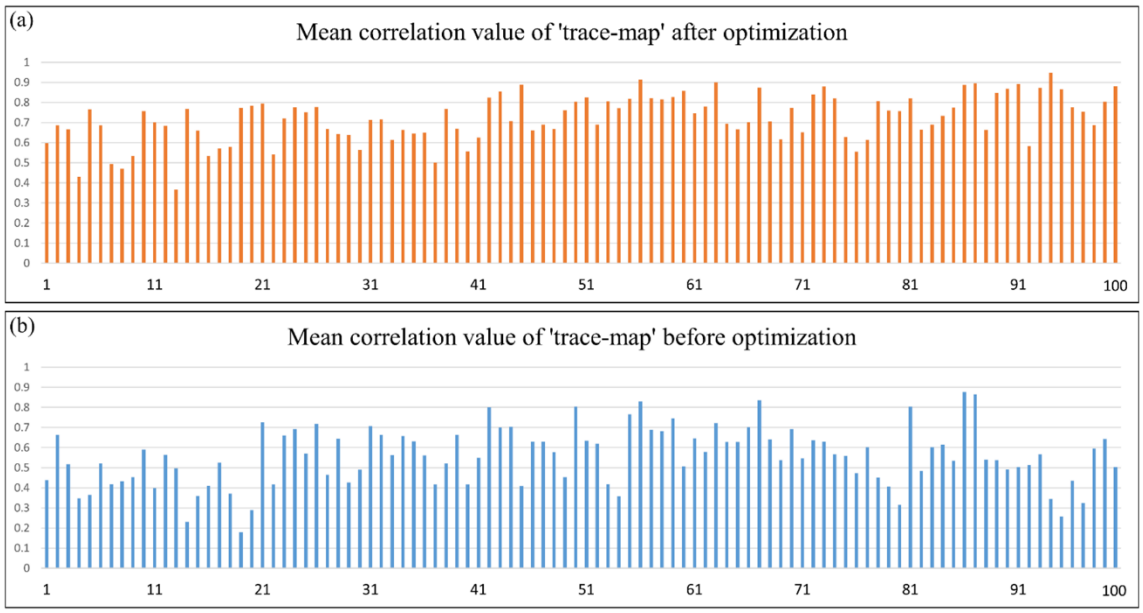

Figure 2.11. The mean correlation value of structural fiber connection 'trace-map'. (a) The mean correlation value of 'trace-map' across any pair of the individuals within two groups for all 100 landmarks after optimization. The horizontal axis represents the 100 landmarks and vertical axis represents the mean correlation value of 'trace-map' across any pair of the individuals for each landmark. (b) The mean correlation value of structural fiber connection 'trace-map' across any pair of the individuals for all 100 landmarks before optimization. The horizontal axis represents the 100 landmarks and vertical axis represents the mean correlation value of 'trace-map' across any pair of the individuals for each landmark.

2.3.3 Effectiveness of Joint Representation of Connectome-scale Structural and Functional Profiles

In this section, we quantitatively examine the effectiveness of the proposed joint representation of connectome-scale structural and functional profiles. To briefly illustrate the difference of identified areas, Figure 2.12 co-visualizes all 100 finalized landmarks and 107 initialized landmarks on one example brain.

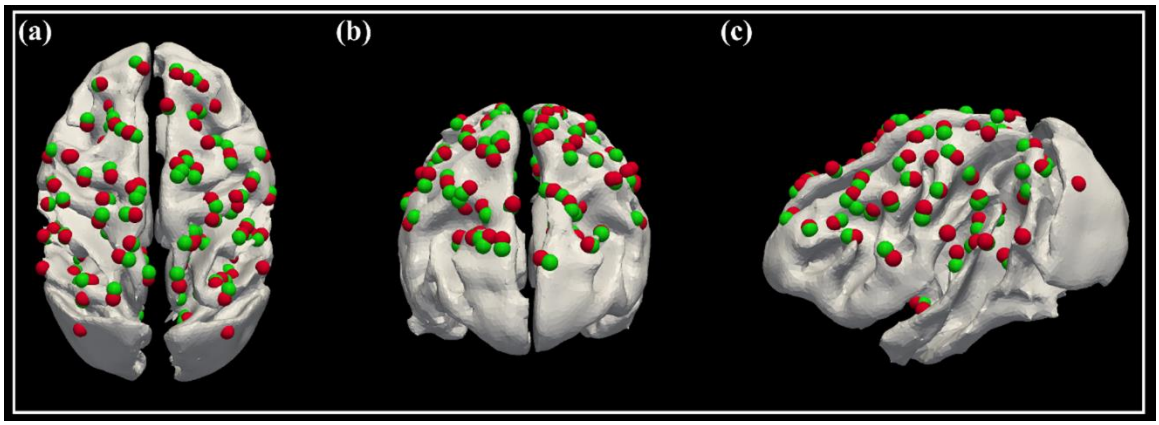

Figure 2.12. The 100 finalized landmarks (green bubbles) and 107 initialized landmarks (red bubbles) co-visualized on one example subject brain in three views in (a)-(c), respectively.

Quantitatively, we first measure and compare the mean correlation value of structural fiber connection 'trace-map' of the 100 landmarks before and after optimization. As shown in Figure 2.11(b), there are 63 out of 100 landmarks whose mean correlation value is significantly increased (p=0.05) after optimization. The rest of landmarks have comparable trace-map values before and after optimization. The averaged correlation of the landmarks is 0.71±0.1275 after optimization and 0.60±0.1625 before optimization.

Second, we calculate the percentage of functional activity value difference of each landmark before and after optimization compared with the functional peak value ($(z_{v_{0i}^p} - z_{v_i^p}) / z_{v_{0i}^p}$ as demonstrated in Section 2.2.2). As reported in Table 2.2, the percentage is as high as ~80% across the two groups, indicating that the functional activity values are not changed much after landmark optimization to preserve the functional consistency.

Table 2.2. The average percentage of functional activity value difference of each landmark before and after optimization compared with the peak value across the six subjects in the two groups. The value is represented as mean±SD.

Group 1 (subject ID)	1	2	3	4
value	**0.9±0.168**	**0.88±0.188**	**0.85±0.213**	**0.85±0.216**
Group 2 (subject ID)	2	4	5	6
value	**0.87±0.2140**	**0.86±0.2103**	**0.87±0.19**	**0.87±0.19**

Third, we calculate the Euclidean distance of spatial location movement of the 100 landmarks before and after optimization. The mean distance of all 100 landmarks is 1.466 mm, indicating that the 100 landmarks can achieve reasonable functional, structural, anatomical, and spatial consistency within a small range from the initialized locations. This finding also indicates that connectome-scale structural profile is reasonably consistent once the functional profile is consistent. This finding also proves the 'fingerprint' concept (Passingham et al., 2002) in connectome-scale, which premises that each brain's cytoarchitectonic area has a unique set of extrinsic inputs and outputs that largely determines the functions that each brain area performs.

In conclusion, both quantitative and qualitative measurements demonstrate the effectiveness of the proposed joint representation of connectome-scale structural and functional profiles. The identified 100 landmarks effectively represent the joint anatomical, structural, and functional profiles across different macaque brains.

2.4 Discussion and Conclusion

In this study, we jointly represented the connectome-scale structural and functional profiles via a computational framework for identification of consistent cortical landmarks in

macaques. We initialized the landmark locations with connectome-scale functional network peaks derived from representation of functional profiles via HAFNI, instead of random initialization or manual labelling in previous studies (e.g., DICCCOL identification in human brains). In this way, the initialized landmarks have functional correspondences and thus provide a foundation for the joint representation of connectome-scale structural and functional connectivity afterwards. During the landmark optimization procedure, we integrated four meaningful constraints: anatomical, structural fiber connection pattern, functional connectivity, and spatial information so that the identified landmarks comprehensively encode anatomical, structural and functional consistency. By applying the proposed computational framework, we have identified 100 consistent and common cortical landmarks in different macaque brains. This set of 100 landmarks has potential to represent common structural/functional macaque cortical architecture for advancements in the neuroscience and brain mapping fields.

The experimental results have demonstrated that the connectome-scale consistent functional brain network patterns across different subjects are successfully identified via our proposed framework, indicating that there exists functional regularity and consistency across different macaque brains. Based on these connectome-scale consistent functional network peaks as initialized landmark locations, the results have shown that a set of landmarks can achieve convergence of functional, structural fiber connection pattern, anatomical, and spatial consistency after the proposed landmark optimization. Our experimental results further demonstrate that there is reasonable regularity among brain function, structural fiber connection pattern, and anatomy within and between the individual macaques, which further proves the ‘fingerprint’ concept (Passingham et al., 2002) in connectome-scale. This is also the premise that

we performed joint representation of connectome-scale structural and functional profiles in macaque brains.

The focus of this study is on the methodology development of joint representation of connectome-scale structural and resting state functional profiles. The potential applications in the neuroscience and brain mapping fields are open to future studies. For example, in this study, we applied the joint representation framework on six-month macaques and the results were promising. In the future, we can apply the proposed joint representation of connectome-scale structural and functional profiles to examine developmental changes in structural and/or functional connectivity after identifying the landmarks in the same individuals at different ages based on the availability of longitudinal, within-subject, multi-modal DTI and fMRI data. As a result, those consistent landmarks across different ages could potentially map the macaque brain regions with developmental-preserved joint representation of anatomical/structural/functional consistency. Conversely, those landmarks merely existing at specific ages could potentially map macaque brain regions with developmentally-related changes in joint representation of anatomical/structural/functional consistency. A more universal landmark map which can systematically encode both the developmentally preserved and changed joint representation of anatomical/structural/functional consistency of macaque brains can thus be obtained, and would be extremely important for neurodevelopmental studies in this animal model. Another application example includes exploring the regularity and variability of structural/functional connectivity/interaction among different cortical regions (e.g., the gyral/sulcal regions) based on these identified landmarks. Moreover, based on the landmarks which encode the joint connectome-scale structural and functional profiles, we can identify possible connectome-scale structural/functional connectivity alterations in specific cortical regions between groups of

macaques with typical/normative developmental experiences ("control groups") and groups with specific experimental treatments or pathologies (e.g., early life stress (Howell et al., 2013; Howell et al, 2016), and use those connectivity alterations as potential biomarkers for identification of different macaque groups.

Acknowledgement

This work was supported by National Institutes of Health (DA033393, AG042599, MH078105, MH078105-04S1, HD055255), National Science Foundation (IIS-1149260, CBET-1302089, BCS-1439051 and DBI-1564736), and Office of Research Infrastructure Programs/OD grant OD11132 (YNPRC Base grant, formerly RR000165). We want to thank Anne Glenn, Christine Marsteller, Dora Guzman, and the staff at the Yerkes National Primate Research Center (YNPRC) Field Station and Imaging Center for the excellent technical support and animal care provided during these studies. The YNPRC is fully accredited by the Association for the Assessment and Accreditation of Laboratory Animal Care (AAALAC), International.

CHAPTER 3

JOINT REPRESENTATION OF CONSISTENT STRUCTURAL AND FUNCTIONAL PROFILES FOR IDENTIFICATION OF COMMON CORTICAL LANDMARKS [2]

[2]Shu Zhang, Yu Zhao, Xi Jiang, Dinggang Shen, Tianming Liu. Joint representation of consistent structural and functional profiles for identification of common cortical landmarks. Brain Imaging and Behavior. 2017:1-15.

Reprinted here with permission of publisher.

Abstract

In the brain mapping field, there have been significant interests in representation of structural/functional profiles to establish structural/functional landmark correspondences across individuals and populations. For example, from the structural perspective, our previous studies have identified hundreds of consistent DICCCOL (dense individualized and common connectivity-based cortical landmarks) landmarks across individuals and populations, each of which possess consistent DTI-derived fiber connection patterns. From the functional perspective, a large collection of well-characterized HAFNI (holistic atlases of functional networks and interactions) networks based on sparse representation of whole-brain fMRI signals have been identified in our prior studies. However, due to the remarkable variability of structural and functional architectures in human brains, it is challenging for earlier studies to jointly represent the connectome-scale structural and functional profiles for establishing a common cortical architecture which can comprehensively encode both structural and functional characteristics across individuals. To address this challenge, an effective computational framework is proposed to jointly represent the structural and functional profiles for identification of consistent and common cortical landmarks with both structural and functional correspondences across different brains based on DTI and fMRI data. Experimental results demonstrate that 55 structurally and functionally common cortical landmarks can be successfully identified.

3.1 Introduction

After decades of active research, one of the significant challenges in the brain mapping field is to define comparable brain regions, or regions of interest (ROIs), across individual subjects. This same challenge also remains as the major barrier of connectome mapping in the

human brain, that is, lacking of a quantitatively-encoded representation of common brain architectures, e.g., via connectome nodes, that can be precisely replicated and predicted across individuals and populations. Both challenges originate from the tremendous individual variability of the human brains. First, there exists remarkable variability in the human brain anatomy between individuals, which has been studied by multiple research areas such as brain image registration and cortical parcellations (e.g., Brett et al., 2002; Fischl et al., 2002; Jbabdi et al., 2009; Johansen-Berg et al., 2004; Li et al., 2009; Shen and Davatzikos, 2002; Rettmann et al., 2002; Stankiewicz et al., 2010; Van Essen et al., 2005); Second, there is tremendous variability of human brain function across individuals, as discussed in many previous papers, such as in Brett et al., 2002; Pessoa et al., 2012; Anderson et al., 2013.

In attempts to address the abovementioned challenges, we have developed the DICCCOL (dense individualized and common connectivity-based cortical landmarks) (Zhu et al., 2012a; Zhu et al., 2012b; Yuan et al., 2013; Jiang et al., 2015b; Zhang et al., 2016) and HAFNI (holistic atlases of functional networks and interactions) (Lv et al., 2015a; Lv et al., 2015b; Lv et al., 2015c; Zhao et al., 2015; Zhang et al., 2016; Zhao et al., 2016) systems to define common and consistent structural and functional landmarks based on DTI and fMRI data, respectively. Briefly, the DICCCOL studies have identified hundreds of consistent cortical landmarks across human individuals and populations, each of which possess consistent DTI-derived fiber connection patterns (e.g., Zhu et al., 2012a; Zhu et al., 2012b; Yuan et al., 2013; Jiang et al., 2015b). However, this method is focused on the DTI data only and the functional roles of those DICCCOLs remain to be elucidated. More recently, the HAFNI studies found that connectome-scale well-characterized functional brain networks (including both task-evoked networks and intrinsic connectivity networks) can be effectively and robustly reconstructed by using sparse

coding on the fMRI data (Lv et al., 2015a; Zhang et al., 2013; Zhang et al., 2016; Zhao et al., 2015; Zhao et al., 2016). However, the series of HAFNI studies were based on fMRI data only and the structural underpinning of these consistent functional networks remains to be revealed.

To address the abovementioned weaknesses of DICCCOL and HAFNI systems while leveraging their major strengths, in this chapter, a novel computational framework to jointly represent connectome-scale functional and structural profiles is proposed for identification of consistent and common cortical landmarks with both reasonably accurate structural and functional correspondences across different human brains based on multimodal DTI and fMRI data. This framework has the following major methodological novelties over the DICCCOL and HAFNI systems alone. First, instead of using roughly sampled grid points in a template brain as the initialized landmarks in the original DICCCOL discovery system (illustrated as blue dots shown in Figure 3.1-③), in this work, the aim is to add the functional guidance informed by HAFNI networks into the step of initializing landmarks (as shown in Step ① and Step ② of Figure 3.1). That is, the peak foci (as illustrated as yellow dots in Step ② of Figure 3.1) derived from HAFNI networks is used to initialize the landmarks. Then, those landmarks are initialized with functional meaning and annotations, followed by a groupwise optimization procedure to determine their final locations in a group of subjects. Second, a groupwise image registration scheme will be applied (as illustrated in Step ② of Figure 3.1) to efficiently decide the final corresponding locations of those initialized landmarks in the specific individual image spaces of all of the subjects. Finally, a new set of HAFNI-informed common and consistent DICCCOL cortical landmarks across human individuals and populations are obtained. These common cortical landmarks jointly represent connectome-scale structural and functional profiles of brain ROIs and also exhibit common structural and functional architectures of the human brain.

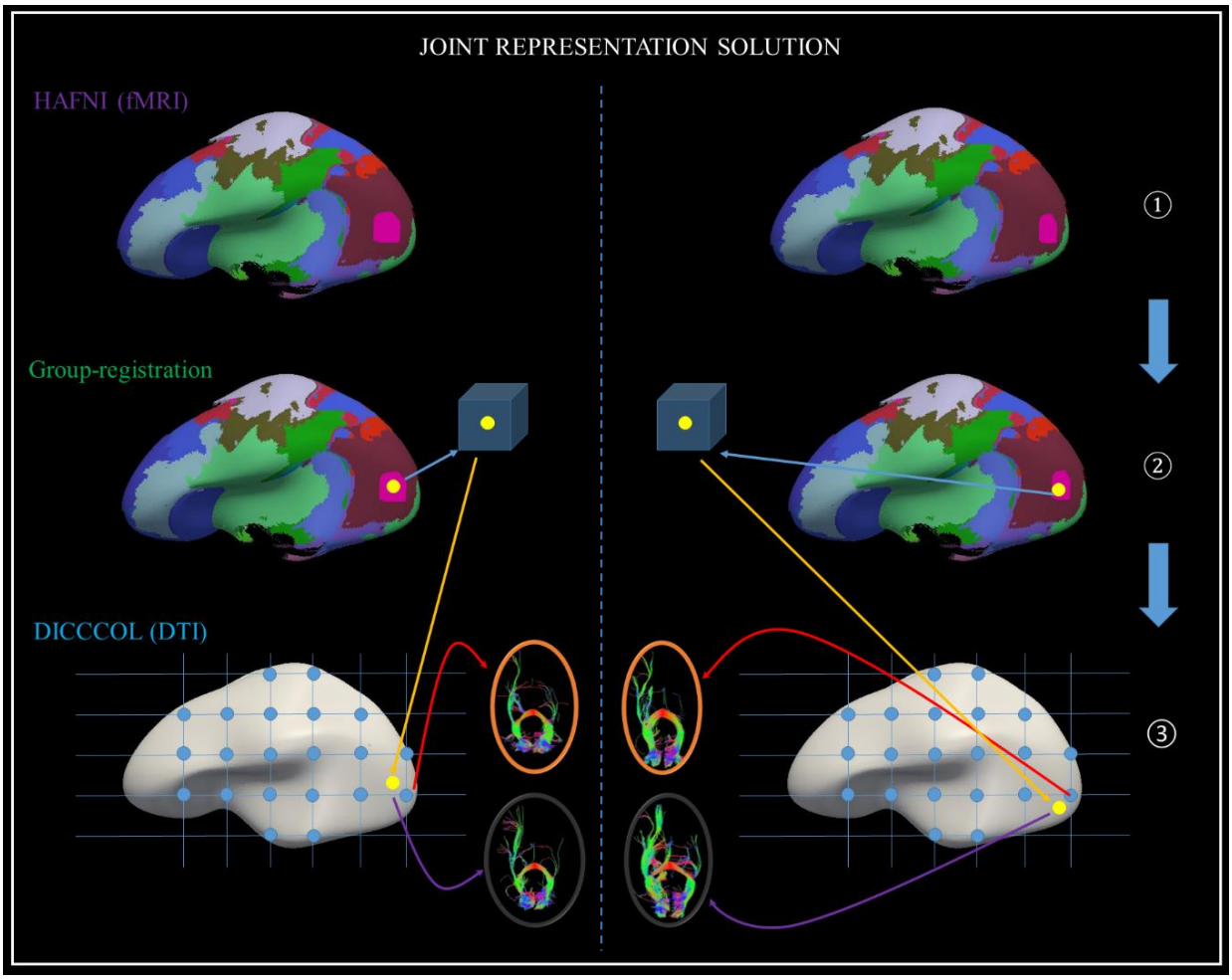

Figure 3.1. Conceptual illustration of joint representation of connectome-scale structural and functional profiles for identification of consistent cortical landmarks by fusing DICCCOL and HAFNI methods. There are three major steps in this framework: using HAFNI method to derive functional peak foci (Step ①), groupwise registration of those functional foci in a group of subjects (Step ②), and using DICCCOL methods to optimize the initialized landmarks (Step ③) towards their final locations with both functional and structural consistency. Here, two exemplar individual subjects are shown and separate by the dashed blue line. In Step ①, consistent HAFNI networks are coded by corresponding colors in two exemplar subjects. In Step ②, yellow dots on the inflate cortical surfaces represent the HAFNI peak foci for one functional network (pink one). The groupwise registration will be applied on all the ROIs represented by the yellow dots across individual subjects. In Step ③, landmark initialization will be based on the corresponding functional foci (yellow dots) after groupwise registration in Step ②, and

landmark optimization will be performed based on the groupwise consistency of structural connectivity patterns.

3.2 Materials and Methods

3.2.1 Overview

The three steps in the conceptual illustration of the framework in Figure 3.1 are further specifically detailed in Figure 3.2 (marked as Step1-3 in Figure 3.2). In Step 1, sparse representation of whole-brain fMRI data is conducted in each subject (a), after which relatively consistent HAFNI networks are identified for all involved subjects (b). Then, a cubic ROI is generated for those most consistent HAFNI network peak foci for each subject (c). Notably, each cubic ROI is defined in an individual's own image space with rough correspondence across different brains. In Step 2, an effective groupwise registration method is employed to register the corresponding ROIs from different subjects into a common space. These registered ROIs will be used to initialize the landmarks in each subject for the next step of landmark optimization in Step 3(e). In Step 3, the joint constraint of consistent connectome-scale structural and functional profiles for each initialized ROI will be enforced for landmark location optimization methodologies. For each subject with multimodal DTI and fMRI data, a landmark identification procedure (e-f) can be performed to locate those HAFNI-informed DICCCOL consistent landmarks. The output of this procedure will be the accurately located common and consistent landmarks in each individual brain (g).

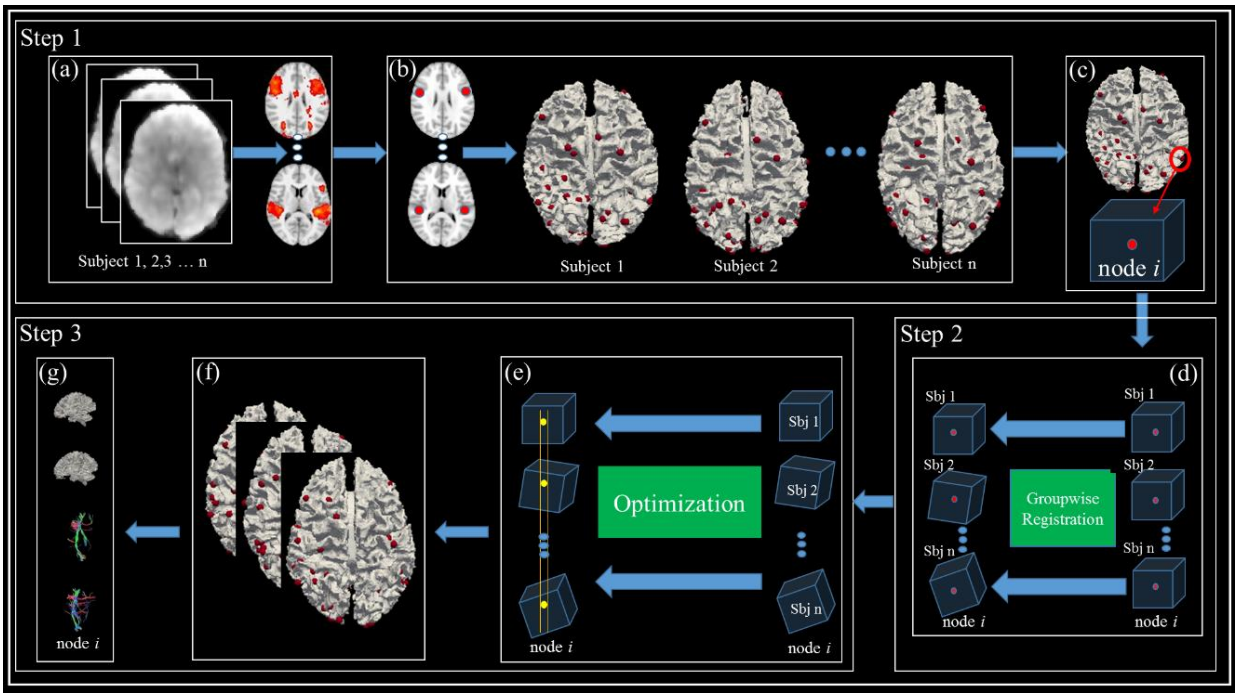

Figure 3.2. The pipeline of the proposed computational framework. Please refer to the details of each step in the main text.

3.2.2 Data Acquisition and Pre-processing

The dataset used in this study was obtained from the Human Connectome Project Q1 release (Barch et al., 2013; Van Essen et al., 2013). The acquisition parameters of task fMRI (tfMRI) data are as follows: 90×104 matrix, 220mm FOV, 72 slices, TR=0.72s, TE=33.1ms, flip angle = 52°, BW=2290 Hz/Px, in-plane FOV = 208×180 mm, 2.0 mm isotropic voxels. For tfMRI images, the preprocessing pipelines include skull removal, motion correction, slice time correction, spatial smoothing, and global drift removal. All of these steps are implemented by FMRIB Software Library (FSL) FEAT (Woolrich et al., 2009). For comparison of results, the general linear model (GLM)-based activation is also performed individually and group-wisely using FSL FEAT. Task stimulus curves are convoluted with the double gamma hemodynamic response function and set as regressors of GLM. The contrast based statistical parametric

mapping is carried out with t-test and $p<0.05$ (with cluster correction) and is used to reject false positive. Multi-level z-scores are used to map multi-scale activations. At the group level, the statistical parametric mapping is carried out with mixed-effect model included in the FSL FEAT tool. For the resting state fMRI (rsfMRI) data, the acquisition parameters are as follows: 2×2×2 mm spatial resolution, 0.72 s temporal resolution, and 1200 time points. The pre-processing of rsfMRI data also include skull removal, motion correction, slice time correction, and spatial smoothing. More detailed rsfMRI preprocessing can be referred to the literature report (Lv et al., 2015a). For diffusion imaging data, the parameters are as follows: Spin-echo EPI, TR 5520 ms, TE 89.5 ms, flip angle 78 deg, refocusing flip angle 160 deg, FOV 210x180 (RO x PE); matrix 168x144 (RO x PE), slice thickness 1.25 mm, 111 slices, 1.25 mm isotropic voxels, Multiband factor 3, and Echo spacing 0.78 ms. Please refer to (Uğurbil et al., 2013; Barch et al., 2013) for more details.

3.2.3 Landmark Initialization

As shown in Figure 3.2a-3.2b, landmark locations are initialized by applying the HAFNI method (Lv et al., 2015a). Briefly, we first obtain 32 group-wise consistent and meaningful functional networks across different human brains via dictionary learning and sparse coding of HCP fMRI data using similar methods in (Lv et al., 2015a). Examples of those 32 consistent networks are shown in Figure 3.3. Then, we automatically identify functional components in each functional network by using the widely adopted connected component labeling (CCL) algorithm implemented in FSL toolbox in each individual brain (http://fsl.fmrib.ox.ac.uk). The basic idea is that, by searching the neighborhood of all voxels involved in a specific functional network, those connected voxels involved in the functional network are assigned to the same component. In this way, each functional network may have one or more components (e.g., each

network in Figure 3.2a has two components). In order to obtain meaningful, stable and consistent functional components across different subjects, we need to carefully consider the smallest size of the components that we should adopt in this work. As we know, small components can be involved in the consistent networks, however, they are possibly very variable across the different subjects, e.g., such small region may not exist in some specific subjects. Thus, we tested the sizes of the components that we should adopt and consider from 100 to 1000 voxels with an interval of 100. When the size approaches 500, all the studied subjects have exactly the same number of the components in each network. Therefore, 500 is a quite acceptable threshold, and those cluster nodes with less than 500 voxels will be discarded in this work. After these common and consistent networks and their connected components are identified in each subject, we identify all the peak foci with the highest functional activities within each network as the initial locations of landmarks to be optimized. Figure 3.3 shows these 32 consistent networks and their peak foci in representative slices.

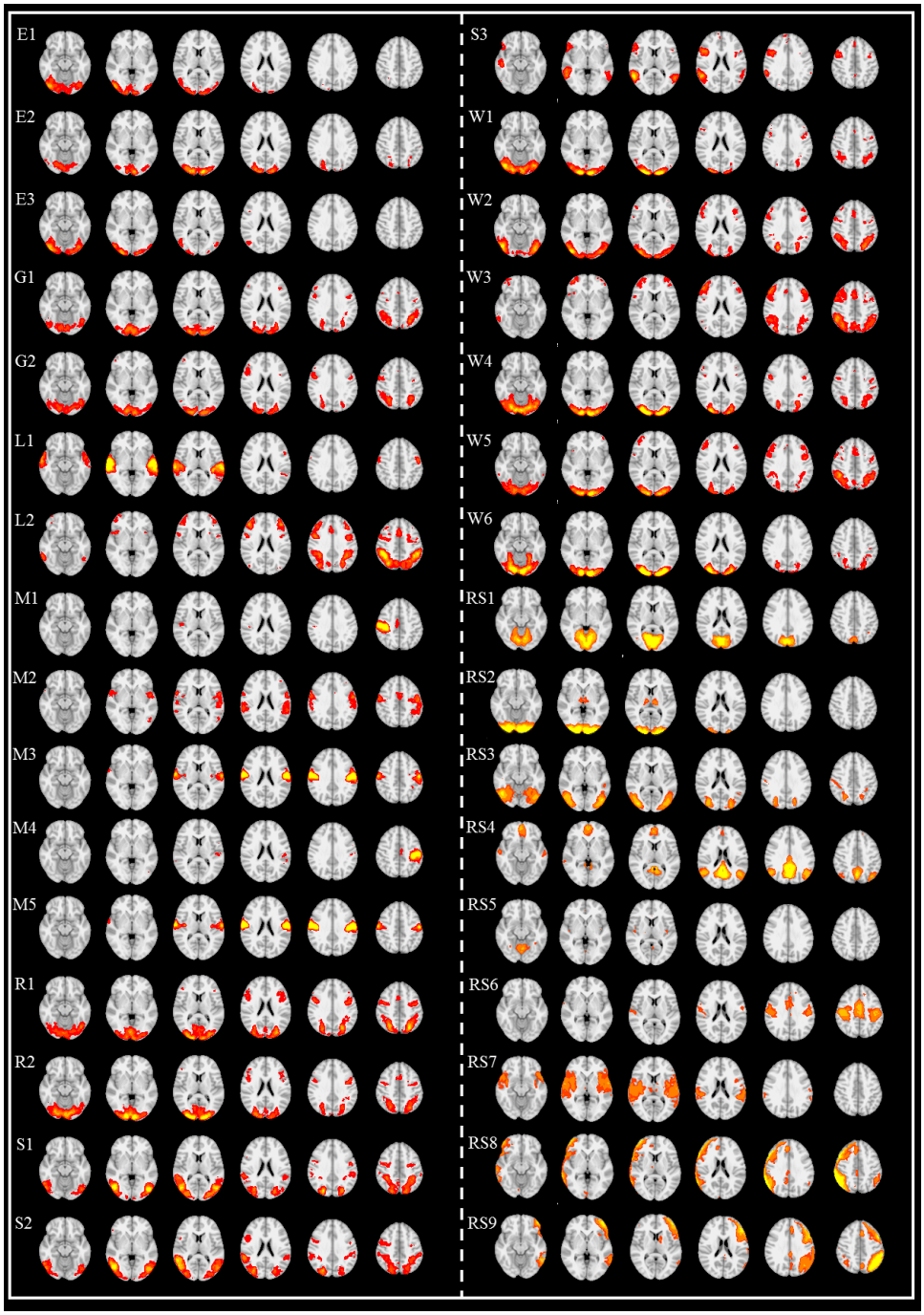

Figure 3.3. The 32 identified common consistent functional brain networks. Six axial slices in each row represent one functional network. The name of the network is shown on the top left. E is short for emotion task, G for gambling task, L for language task, M for motor task, R for relational task, S for social task, W for working memory task, and RS for resting state.

Afterwards, for each of the above initialized landmark, we define an ROI as a 3D cube to include structural and functional profiles around each landmark, as shown in Figure 3.2c. Specifically, within the 3D cube centered on the landmark, the functional network intensities (the loading coefficients after dictionary learning and sparse representation) will be profiled and included. As the fMRI data have already been registered with DTI data for each subject, the DTI-derived fibers that penetrate the 3D cube will be extracted and profiled too. Finally, only those voxels in the 3D cube that possess both strong functional activities and DTI-derived fiber connections will be kept as the key binarized foreground voxels (with the threshold empirically determined) inside the initialized landmark for the next step of group-wise registration.

3.2.4 Groupwise Registration of Initialized Landmarks

As shown in Figure 3.2d, a groupwise registration approach is employed in this study to align the above initialized landmarks in Section 3.2.3. Here, we employ an effective groupwise registration framework that utilizes a hierarchical image clustering and atlas synthesis strategy (Wang et al., 2010). After running the groupwise registration method, all the corresponding initialized landmarks will be mapped into a common space, and thus they will have rough voxel-to-voxel correspondences. The advantage of this approach is that we can not only achieve higher registration accuracy than other pair-wise registration methods (Wang et al., 2010), but also significantly speed up the time-consuming registration process. As illustrated in Figure 3.4, the inputs to the group-wise registration are the initialized 3D cube landmarks with binarized structural and functional profiles in a group of subjects. After the groupwise registration procedure, all of those landmarks are aligned into a common space. It is noted that we obtain and apply a transformation matrix for each landmark, after which they will have rough voxel-to-voxel correspondences across different brains.

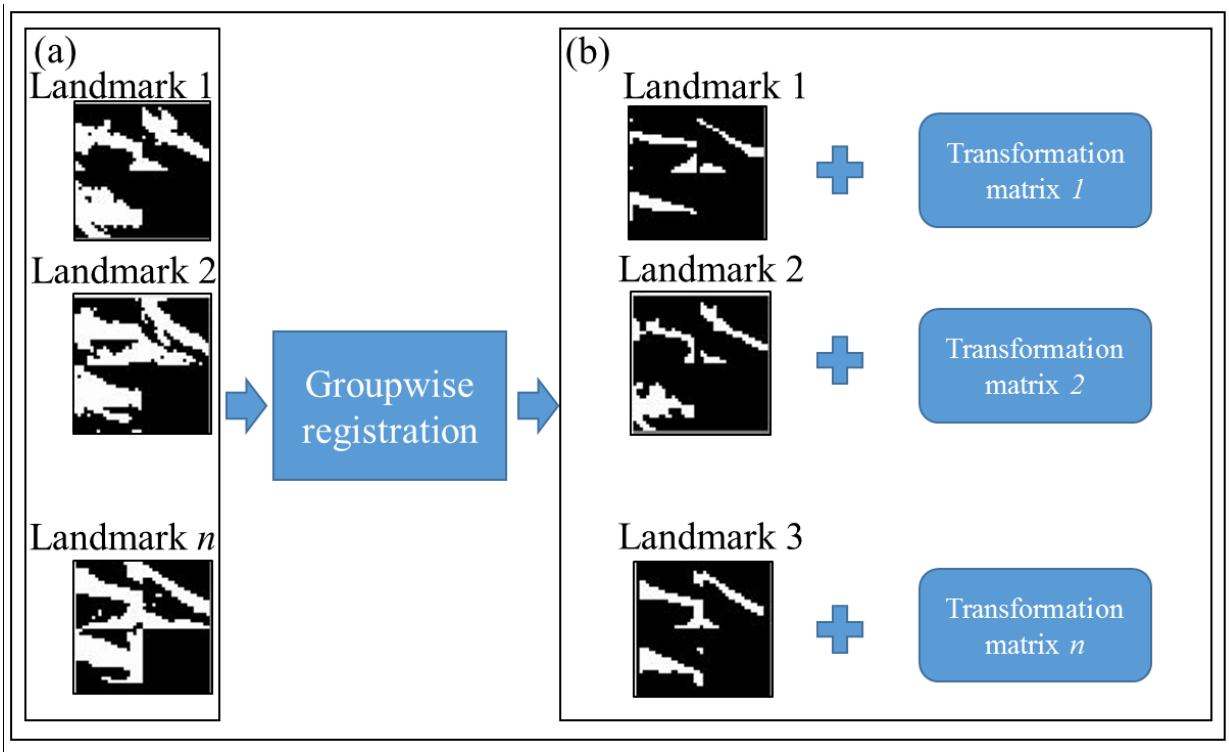

Figure 3.4. Illustration of using groupwise registration for initialized landmarks. (a) Three initialized landmarks in three subjects. (b) Registered and aligned landmarks.

3.2.5 Landmark Optimization

The goal of the optimization step is to adjust the locations of initialized landmarks according to an optimization objective and thus determine the final locations of those landmarks. Specifically, in this study, the aim is to maximize the similarities between the 'trace-maps' of DTI-derived fiber bundles for those initialized landmarks, in a similar way as those in (Chen et al., 2013; Zhu et al., 2012a). To be self-contained, we briefly describe the 'trace-map' representation and comparison of the DTI-derived structural fiber connection pattern. The "trace-map" method is shown in Figure 3.5a-3.5d by projecting each beginning and ending point of each fiber from fiber bundles (Figure 3.5b) onto the uniform spherical surface. Then, we divide the surface into 48 equal areas and construct histogram for each area, which are then represented as the feature vectors. A 48 dimensional histogram vector $\boldsymbol{tr} = [d_1, d_2..d_{48}]$ containing 48

density values, namely ‘trace-map’ (Figure 3.5d), is finally obtained as the structural profile of the landmark under consideration. By calculating the trace-map vectors, fibers penetrating to the landmark can thus be represented by 48-dimension vectors, instead of 3D shapes or images, which enables the quantitative measurements of structural connectivity patterns and similarities for the landmark optimization (Zhu et al., 2012a). The actual landmark optimization procedure within the training samples is briefly illustrated in Figure 3.5e. Since those 3D cube landmarks are already binarized and they have rough voxel-to-voxel correspondence with each other, so the group-mean 3D cube landmark is simply obtained by adding 3D cube landmarks together. Then, voxels from the group-mean 3D cube with large values will be picked up, and the further round of searching is applied onto those voxels to identify the final location of the landmark by pursuing the landmark with maximum average correlation of trace-map vectors among all the subjects. In this way, the optimized landmark is obtained in the common space, and then the transformation matrix will be used to transfer the identified landmark back into the individual DTI surface.

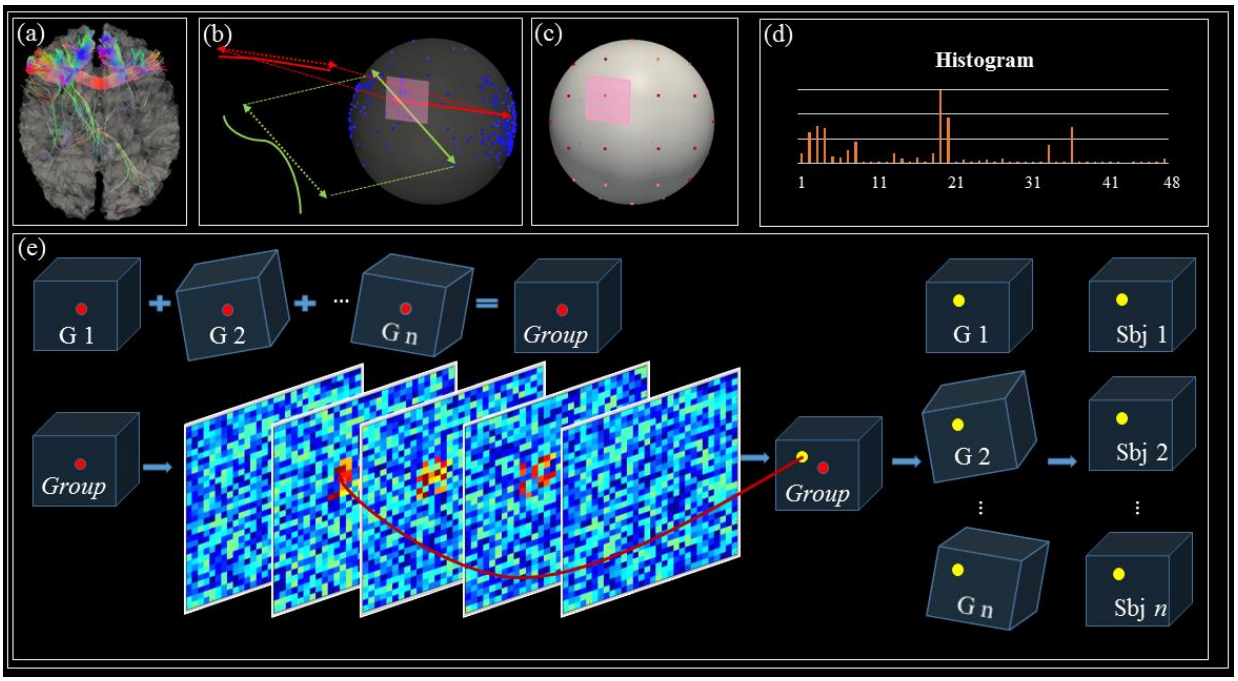

Figure 3.5. The pipeline of 'trace-map' representation for representation of structural connectivity profile of landmarks. (a) An example of a landmark's fiber bundle and cortical surface. (b) Points distribution by projection of the principal orientations of points of each fiber onto the unit sphere. (c) 48 equally-sized areas from one uniform sphere are shown. (d) 48-dimension vectors are used to represent one landmark's fiber bundles. (e) The optimization step. The red bubbles are the initial landmarks, and yellow bubbles represent the locations after optimization. $G_1, G_2 \dots G_n$ are landmarks in common space, and Sbj_1, Sbj_2, Sbj_n are landmarks transformed into individual spaces.

3.3. Experimental Results

3.3.1 Identified Consistent Cortical Landmarks

After applying the computational framework in Sections 3.2.3-3.2.5 on eight randomly selected subjects from HCP dataset, we have identified totally 57 consistent and common cortical landmarks in all 8 subjects, as shown in Figure 3.6 (colored bubbles). Specifically, we originally identified 65 peak foci from 32 consistent common functional brain networks (Figure 3.3), where 57 of them are located on the cortical cortex. After the optimization procedure, all of these 57

cortical peak foci remained as consistent and common cortical landmarks. In this set of 57 landmarks, 30 of them are located on the left hemisphere and the rest are located on the right side, suggesting that these consistent landmarks are relatively symmetrical on both hemispheres. It is noted that more consistent landmarks are distributed in the parietal and occipital lobes, while less consistent landmarks belong to the frontal and temporal lobes, which is in agreement with known neuroscience knowledge that there is more variability in the frontal and temporal lobes.

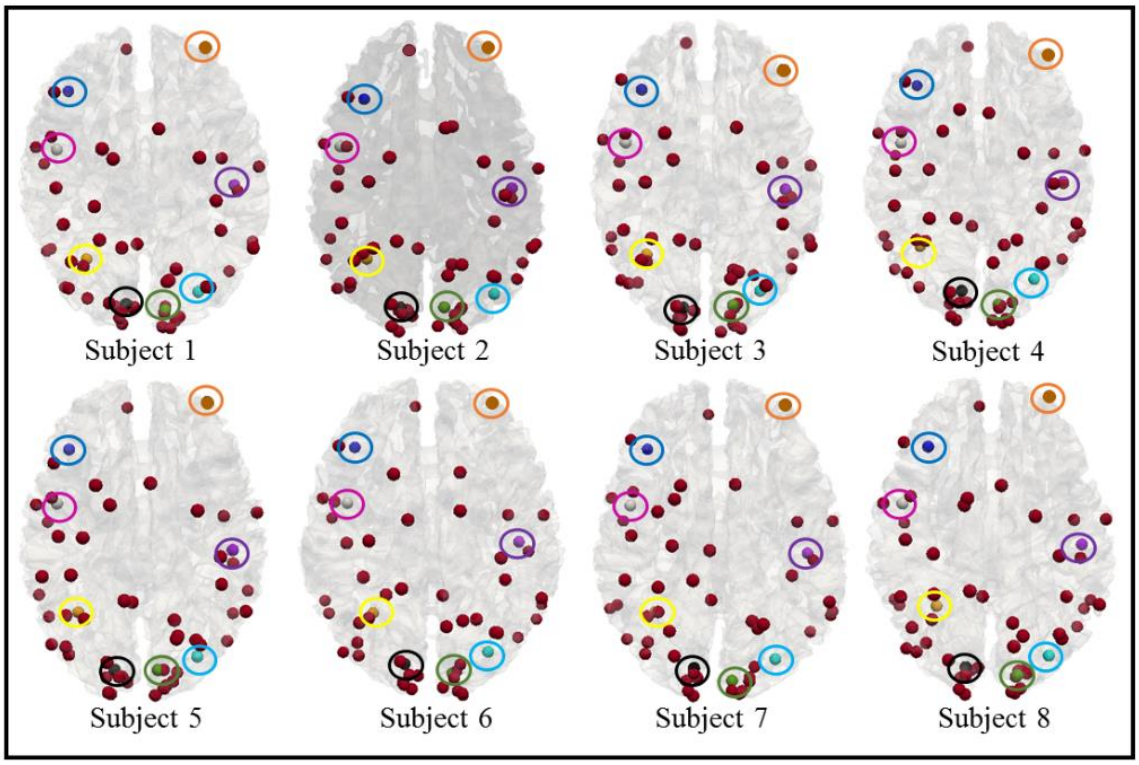

Figure 3.6. Visualization of 57 consistent and common cortical landmarks in 8 subjects. Specifically, in this figure, 8 of those 57 common landmarks are highlighted with different colored circles to provide correspondences in different subject brains.

In order to visualize these consistent and common cortical landmarks in more details, we randomly chose 8 landmarks here as examples. The locations of those 8 selected landmarks are highlighted by the circles with different colors in Figure 3.6. Here, the same color denotes the

correspondence across 8 subjects. In addition, the shapes of the fiber bundles connected to these landmarks are provided in Figure 3.7. From Figure 3.6 and Figure 3.7, we can observe that these consistent and common cortical landmarks have reasonable anatomical and structural connectivity consistency across different subjects, despite their noticeable variability. Quantitatively, the mean correlation of 'trace-map' across any pair of the eight subjects in Figure 3.7 are 0.66, 0.70, 0.50, 0.752, 0.74, 0.80, 0.65 and 0.70, respectively. The overall mean correlation of "trace-map" of all 57 common landmarks in these 8 different subjects is as high as 0.69, which suggests good correspondence of these landmarks across different brains. Besides, the corresponding landmarks across these subjects are from the same functional networks, which means that these landmarks also possess functional correspondence and consistence. In other words, each consistent and common cortical landmark in Fig.6 has three types of consistency: 1) anatomical consistency, 2) structural connectivity consistency and 3) functional consistency. In order to further demonstrate the effectiveness of our proposed framework, these three different aspects will be explained in more details in Sections 3.3.2 to 3.3.4, respectively.

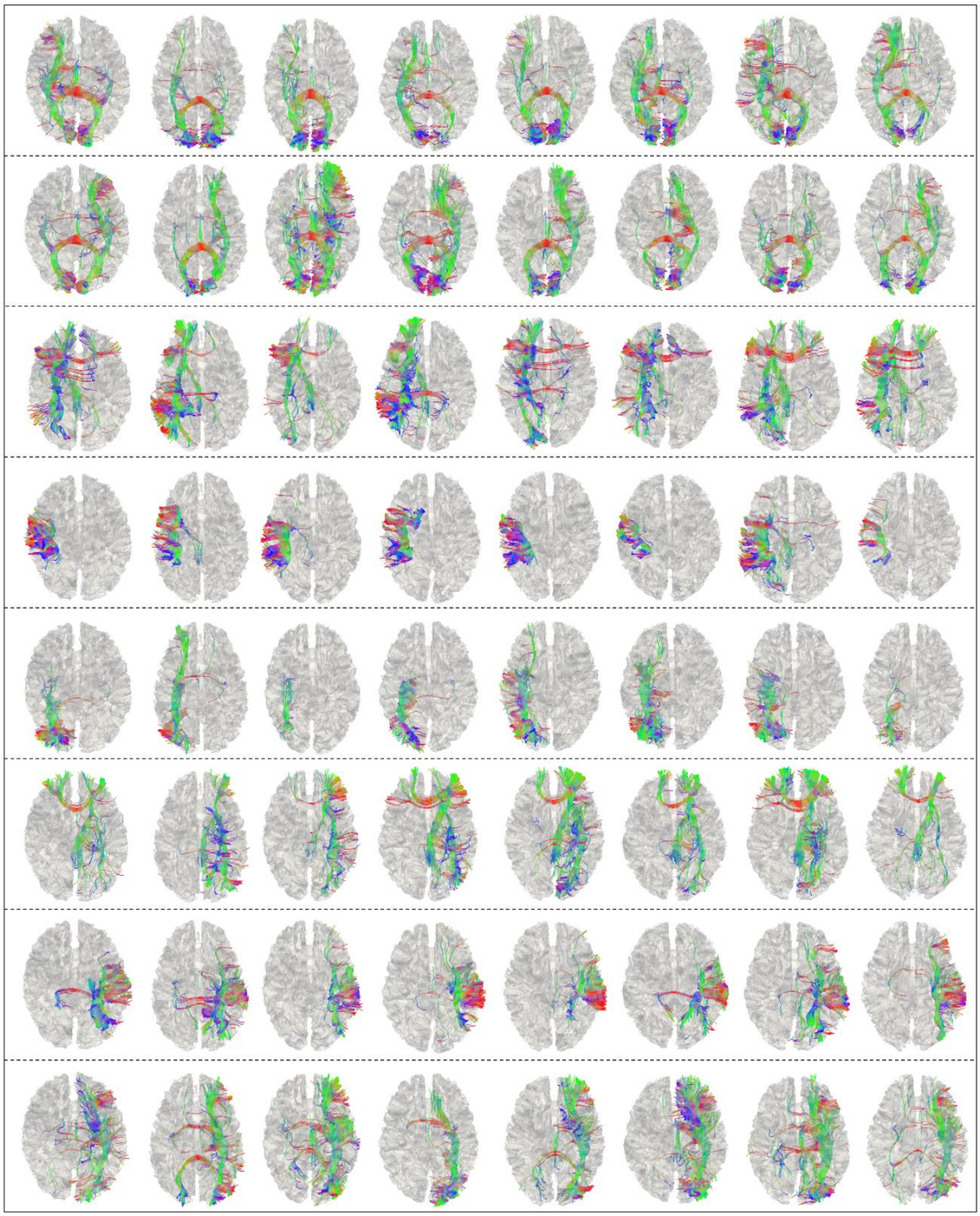

Figure 3.7. DTI-derived fiber bundles of those 8 highlighted landmarks (by colored circles) in Figure 3.6 for 8 subjects. Different rows (from top to bottom) correspond to the black, green, dark blue, pink, yellow, brown, purple, and light blue circles in Figure 3.6, respectively.

3.3.2 Comparisons between Initialized and Optimized Consistent Cortical Landmarks

In order to show the effectiveness of the framework, here we visualize 4 representative examples and their comparisons in Figure 3.8. As we can observe from this figure, there are mainly two scenarios by our optimization framework. One is shown in Figure 3.8a, in which the initialized and optimized landmarks have quite similar locations. That is, there is no big difference between them, and the Euclidean distance of spatial movement of these landmarks before and after optimization is around or less than 2 mm. Interestingly, there is another scenario, which occurs quite often, with significant improvement by our landmark optimization procedure. For instance, the initial landmarks may have inconsistent locations (i.e., blue landmarks of Figure 3.8b), e.g., some of them may distribute on the gyri, but others may locate on the sulci. After applying the optimization framework, the optimized landmarks (red bubbles) are finally located with much better consistency, e.g., as shown in Figure 3.8b, all the landmarks with red color are finally consistently located on the sulci. The Euclidean distance of spatial movement of these landmarks before and after optimization is larger than the first scenario, typically within the range of 2-14 mm. Quantitatively, the Euclidean distance of spatial location movement of all 57 landmarks before and after optimization is 11.45 mm in 8 subjects, indicating that the landmark optimization procedure is really needed to reallocate those 57 initialized landmarks to their corresponding locations in different brains. Here we would like to emphasize that this movement is a reasonable metric to evaluate the performances of difference methods. For example, as we know, the usual movement of landmarks between DICCCOL (Zhu et al., 2012a) method and FSL linear registration algorithm is about 3 mm, however, the functional profiles are not considered in that case. In this work, larger movement is needed due to the objective of pursuing functional consistency.

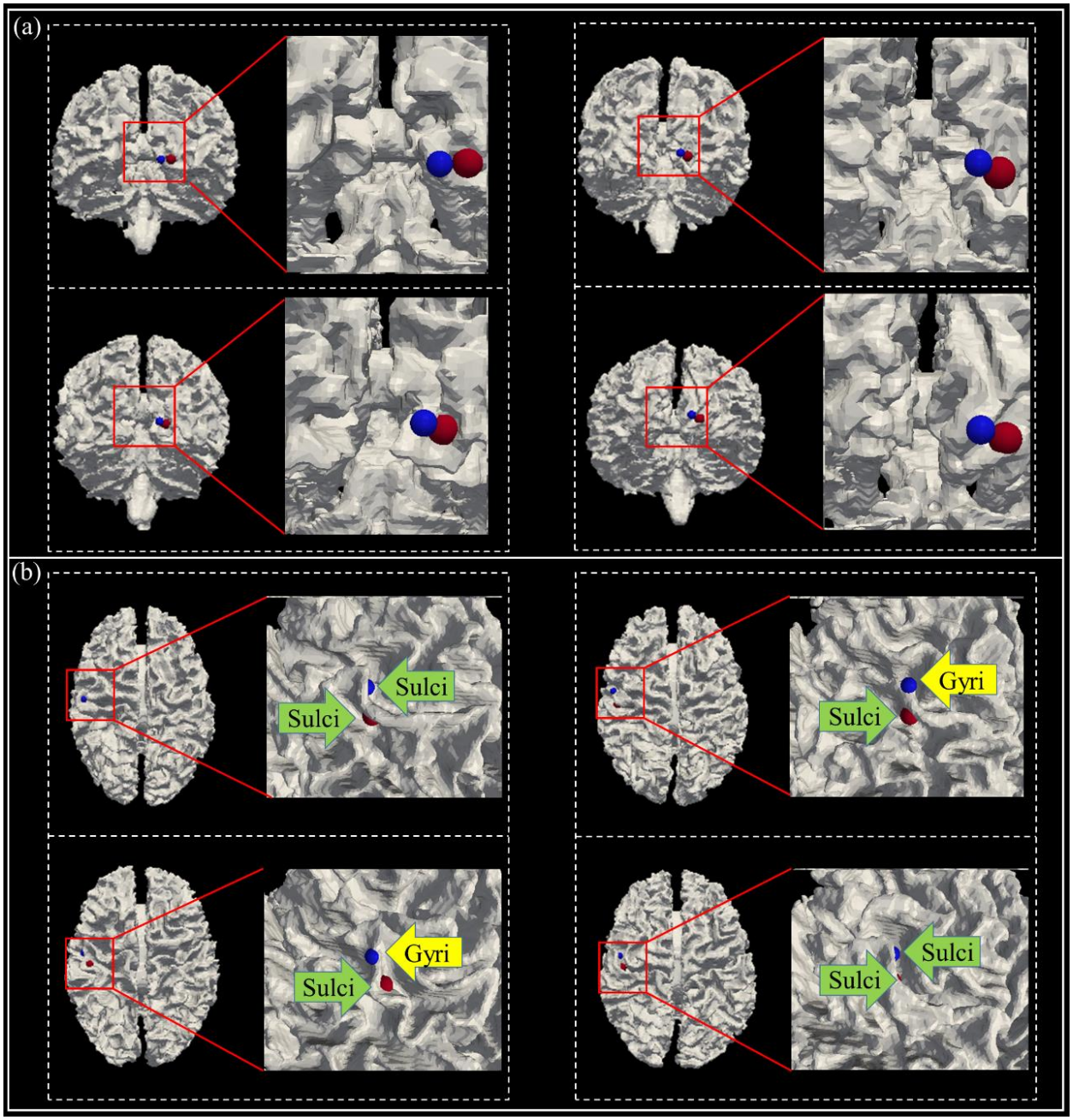

Figure 3.8. Comparison between initialized landmarks and optimized landmarks. In each panel (a&b), one consistent and common cortical landmark is presented by 4 dashed boxes, each dashed box includes one landmark example in one subject. Blue bubbles are the initialized locations of the functional peak foci, and red ones are the landmarks after the optimization. Location of landmarks are highlighted by the colored arrows.

3.3.3 Functional Consistency of Identified Common Cortical Landmarks

In this subsection, we aim to examine the functional consistency of the landmarks before and after optimization. Since we use the functional brain networks to pick up the initial landmarks as mentioned in Section 3.2.3, each initialed landmark is corresponding to one peak focus of a specific group-level common functional network, as shown in Figure 3.3. In our proposed framework, we assume that the final location of initialed landmark will have functional consistency with its initialed landmark, that is, they should belong to the same activation areas on the specific functional network. In order to verify this point clearly, we register each individual functional network onto its own cortical surface and highlight the activated areas with red color. Then, we highlight each pair of landmarks (before and after the optimization step) that we are interested in. From Figure 3.9 and Figure 3.10, 4 sets of landmarks are used as examples to reveal the functional consistency of the identified common landmarks (another 4 examples are shown in the Appendix A Figure A.1 and Figure A.2). It is evident that the optimized landmarks are consistent and meaningful in functional perspective, in that all of the optimized landmarks (green dots) are still located within the corresponding functional activation areas, compared with the initialed ones (yellow dots). Although there are noticeable variabilities among the functional networks in individual brains, the functional consistency of the identified common landmarks can be visually appreciated.

Quantitatively, the average spatial overlap between the consistent common functional brain network and its corresponding individual functional network is 0.334, which is reasonably high based on our experience (Lv et al., 2015a; Zhang et al., 2013; Zhang et al., 2016; Zhao et al., 2015; Zhao et al., 2016). Using the consistent common functional brain networks as a guidance to initialize the landmarks will facilitate the functional consistency of optimized

landmarks. In comparison with the original DICCCOL optimization system (Zhu et al., 2012a; Zhu et al., 2012b; Yuan et al., 2013; Zhu et al., 2014a; Jiang et al., 2015b; Zhang et al., 2016) which used the roughly sampled grid points in a template brain as the initialized landmarks, taking functional profiles into consideration in this proposed framework leads to promising results.

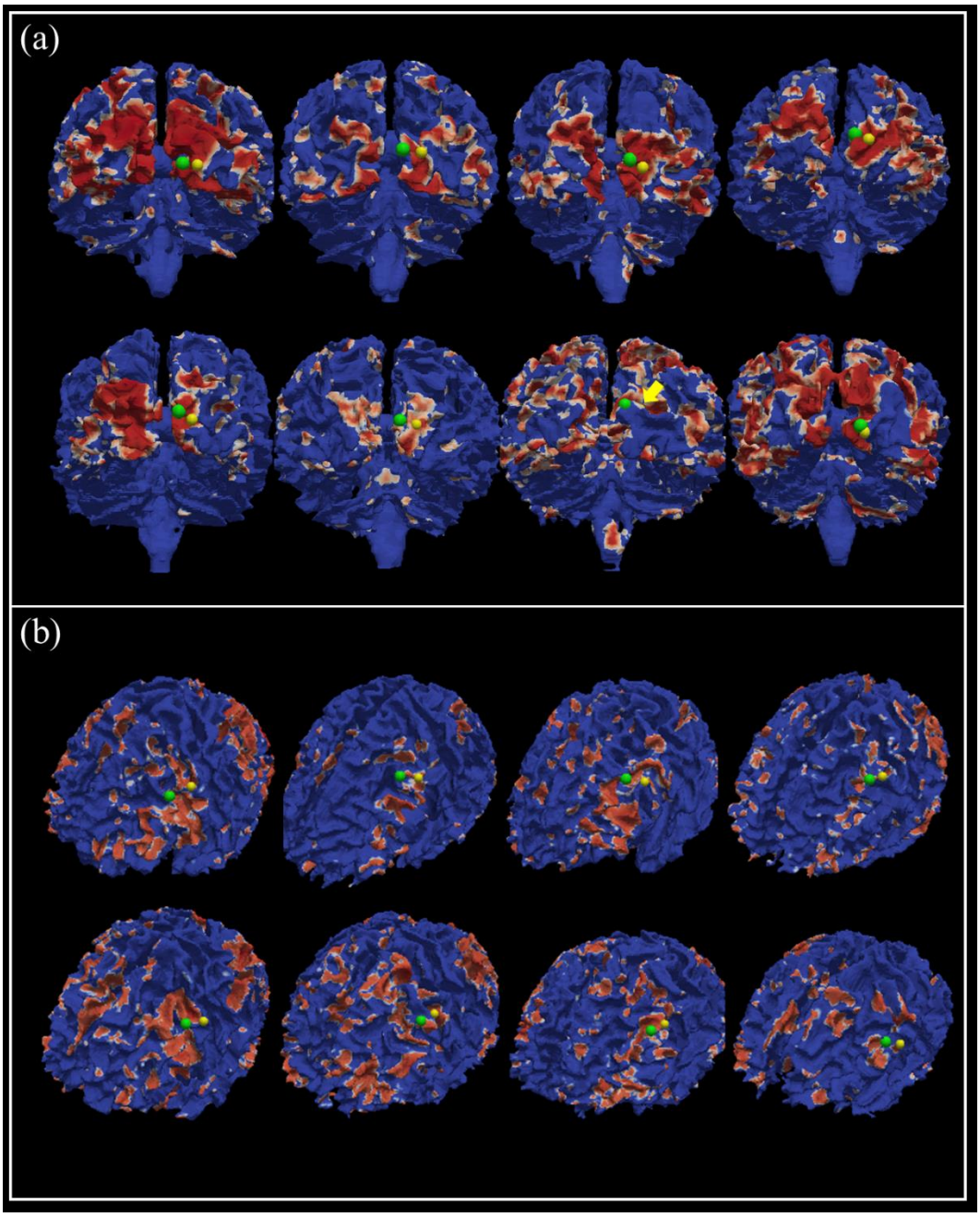

Figure 3.9. The locations of the landmarks before and after optimization. (a) and (b) are the two examples. In each example, 8 function networks are picked up from 8 different subjects, which are corresponding to the same group-level common functional network. Yellow dots are the landmarks before the optimization, and green dots are the optimized landmarks. Red areas represent the highly activated patterns on the cortical surface. The yellow arrow (in panel (a)) is used to show the location of a landmark before the optimization as it is blocked by the gyrus. (a)

is corresponding to G2 network in Figure 3.3, and (b) is corresponding to W3 network in Figure 3.3.

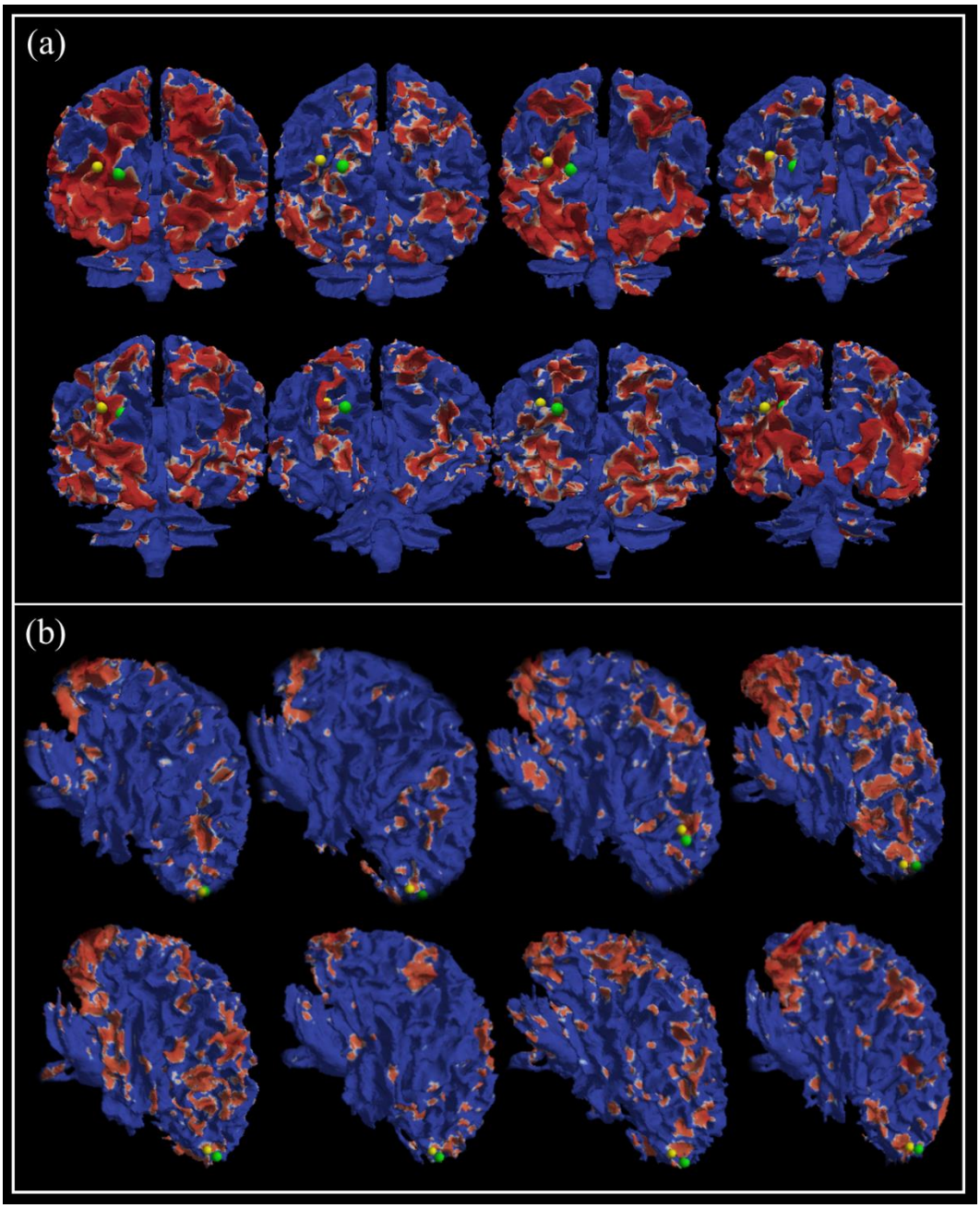

Figure 3.10. Two examples of the landmarks before and after optimization. (a) is corresponding to S2 network in Figure 3.3, and (b) is corresponding to W3 network in Figure 3.3.

3.3.4 Joint Representation of Consistent Cortical Landmarks in Larger Datasets

In the original DICCCOL system (Zhu et al, 2012a), the total number of subjects used in the optimization procedure is 5, which is relatively small, due to the fact that the landmark location search space grows exponentially with the number of subjects. In this proposed framework with groupwise registration procedure in Section 3.2.4, the landmarks are already better aligned into the template space and this step will substantially reduce the search space of landmark location during the optimization procedure. This important improvement can significantly speed up the common landmark discovery process, and thus the new landmark identification framework in this work can deal with a larger number of subjects. In addition to the 8 subjects used in previous results subsections, 20 additional subjects are also included in this subsection to demonstrate the performance and reproducibility of our method.

Figure 3.11 shows the identified consistent cortical landmarks in 28 subjects. Here, 55 landmarks are identified and considered as consistent cortical landmarks. Compared with the results from 8 subjects in Sections 3.3.1-3.3.3, two landmarks are discarded by the groupwise registration procedure. The possible reason is that the functional or structural consistency of these two functional peak foci (used as initialization) are not consistent across 28 subjects. As a consequence, the groupwise registration algorithm will reject these two landmarks. For other 55 consistent landmarks, they are located on similar and corresponding areas as those in Figure 3.6. In order to illustrate the consistency with the results in Figure 3.6, we highlighted in Figure 3.11 the corresponding landmarks using the same colored circles as in Figure 3.6. The anatomical location correspondences of these 55 common landmarks can be visually appreciated. In addition, in Figure 3.12, we choose the same set of 8 landmarks (which are the same as those shown in Figure 3.7) to visualize the fiber bundles connected to the corresponding landmarks.

Figure 3.6, Figure 3.7, Figure 3.11 and Figure 3.12 show that, although the number of the subjects used for landmark optimization grows from 8 to 28, both the locations of identified landmarks and their fiber connection patterns are quite similar within and across these two groups of subjects. Quantitatively, the mean Euclidean distance of spatial location movements of the landmarks before and after optimization of all 55 landmarks is 10.44 mm, which is quite similar to the results reported in Section 3.3.1. For comparing the similarity of the shapes of fiber bundles, we compute the mean correlation of 'trace-map' for all 55 corresponding landmarks obtained in Section 3.3.1 and Section 3.3.3, and achieve as high as 0.70 for mean correlation coefficient. For each corresponding landmark in Figure 3.7 and Figure 3.12 (each row), the average similarity of fiber shapes is 0.87, 0.95, 0.52, 0.93, 0.67, 0.71, 0.82 and 0.93, respectively. These results suggest that our method and results are reproducible using different numbers of subjects.

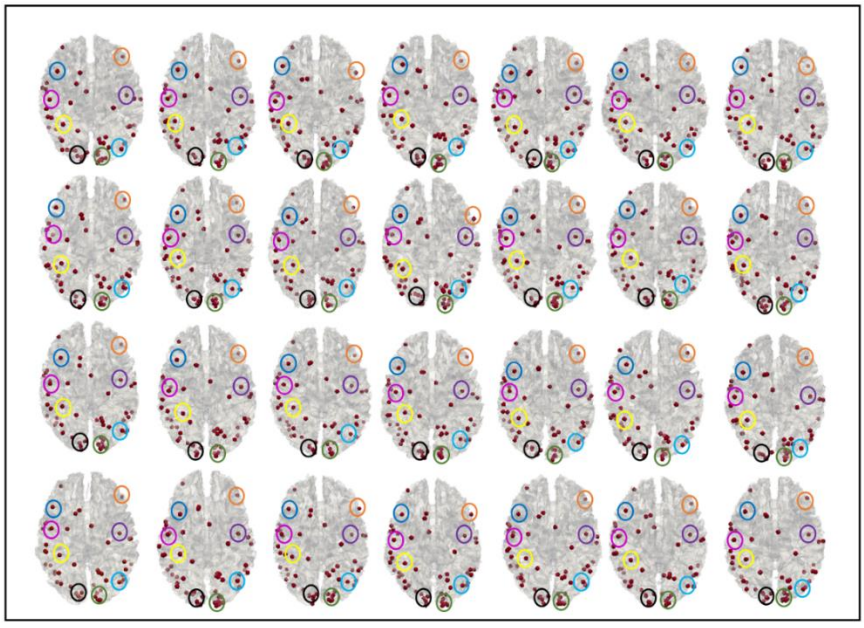

Figure 3.11. Identified consistent cortical landmarks in 28 subjects. 55 common landmarks are highlighted with dark red dots. In particular, 8 landmarks are highlighted by 8 different colored circles on the cortical surface to show the consistency of their anatomic locations.

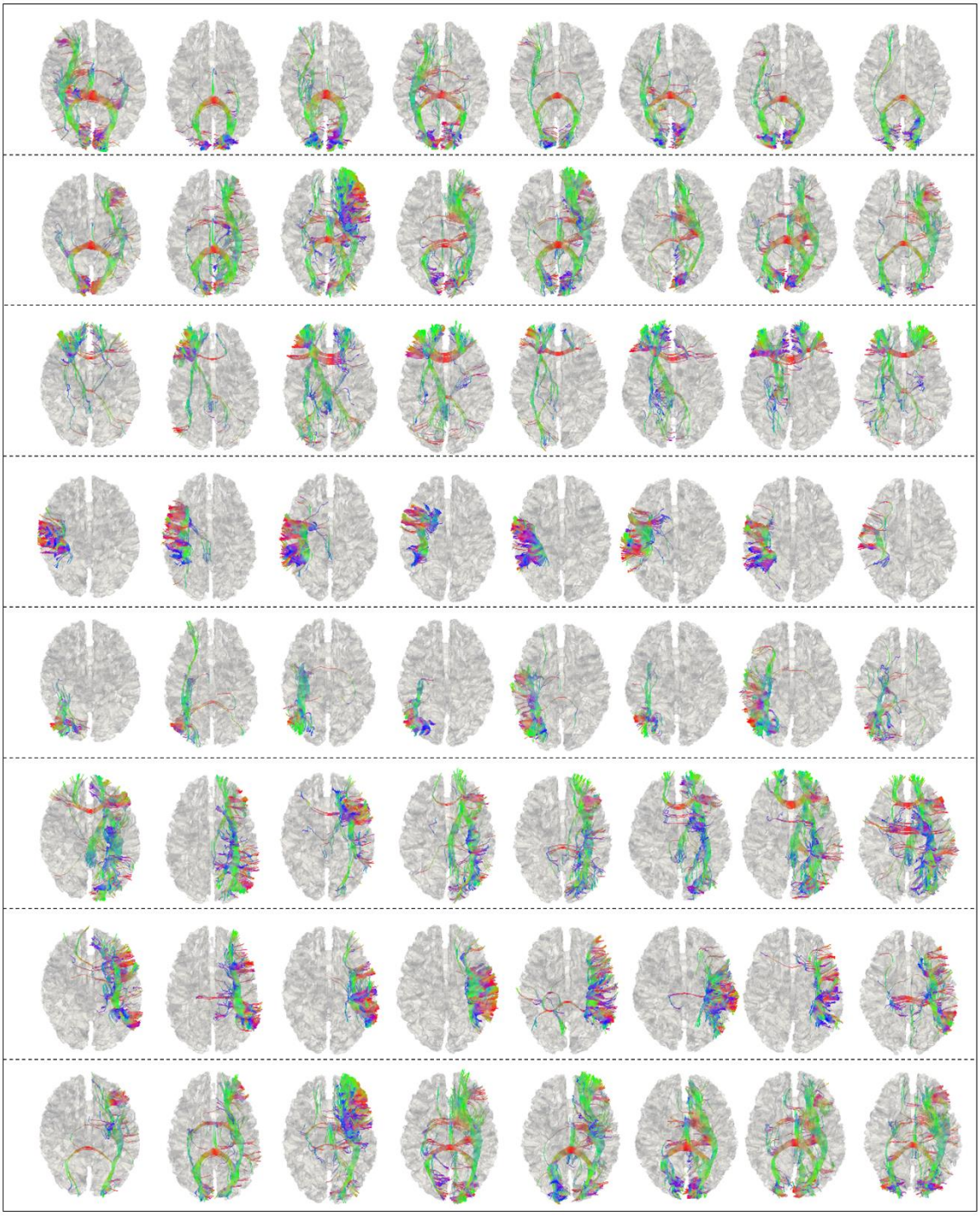

Figure 3.12. Shapes of fiber bundles connected to the 8 landmarks in 8 subjects. Each row represents the fiber bundles for one corresponding landmark in 8 subjects. Visualization schemes are similar to those in Figure 3.7.

3.3.5 Landmark-Based Meta-analysis

In order to acquire more details of functional and structural information of those finalized consistent cortical landmarks and compare the results obtained with other existing experiments, in this section, 55 finalized landmarks are registered onto the MNI standard space by using linear registration from FSL tool (Woolrich et al., 2009). Then meta-analysis method is applied to study those landmarks by using the software Sleuth from brainmap.org (Eickhoff et al., 2009). Here, the ROI width is set to 4 mm. In a structural perspective, among those 55 landmarks, 30 are on the left hemisphere and the rest are on the right hemisphere. The coordinates of 55 consistent cortical landmarks on the MNI standard space are listed in Table 3.1. In addition, among those 55 landmarks, the number of landmarks in each lobe are summarized and shown in Table 3.2.

From Table 3.2, we can clearly see that the occipital lobe has much higher consistency when compared with other lobes. On the other hand, the frontal lobes have relatively larger differences across the subjects. These results are consistent with current knowledge about the variability of cortical lobe functions. Please refer to the Appendix A, Table A.1 for the details of structural locations of each landmark.

In a functional perspective, functional behaviors of each landmark (foci on the MNI space) are summarized by searching more than 3000 literature fMRI papers. In total, 7 main functional behaviors are summarized in Table 3.3. From the Table 3.3, we can see that these functional behaviors are relatively consistent across the subjects. In addition, these functional behaviors contain large number of landmarks, which suggests that these functional behaviors are complex and located on large areas across the whole cortex. Details of functional behaviors for each landmark are listed in Appendix A, Table A.2.

Table 3.1. The locations of the 55 consistent cortical landmarks in MNI standard space (mm).

Index	*x*	*y*	*z*	*Index*	*x*	*y*	*z*	*Index*	*x*	*y*	*z*	*Index*	*x*	*y*	*z*
1	*-6*	*-91*	*-5*	*2*	*13*	*-95*	*-2*	*3*	*-10*	*-97*	*-6*	*4*	*-21*	*-85*	*-13*
5	*10*	*-86*	*-8*	*6*	*-53*	*-16*	*-26*	*7*	*-33*	*38*	*-12*	*8*	*-48*	*-35*	*27*
9	*18*	*-66*	*32*	*10*	*44*	*-54*	*29*	*11*	*-20*	*-29*	*42*	*12*	*-51*	*-5*	*-11*
13	*51*	*-24*	*2*	*14*	*25*	*-34*	*46*	*15*	*-51*	*-12*	*-2*	*16*	*43*	*-20*	*2*
17	*-10*	*4*	*42*	*18*	*-30*	*-70*	*28*	*19*	*-4*	*-86*	*2*	*20*	*36*	*-81*	*16*
21	*-15*	*-92*	*-11*	*22*	*-36*	*-71*	*-15*	*23*	*-13*	*-59*	*42*	*24*	*15*	*-72*	*36*
25	*41*	*-79*	*-17*	*26*	*-50*	*-59*	*-22*	*27*	*-31*	*-82*	*13*	*28*	*11*	*-71*	*34*
29	*45*	*-57*	*-7*	*30*	*-41*	*-61*	*-16*	*31*	*15*	*-95*	*-8*	*32*	*-41*	*-45*	*31*
33	*-14*	*-9*	*47*	*34*	*-26*	*-84*	*2*	*35*	*-10*	*-92*	*-6*	*36*	*9*	*-97*	*6*
37	*10*	*-97*	*-3*	*38*	*-29*	*-51*	*39*	*39*	*-18*	*-86*	*-13*	*40*	*9*	*-90*	*-6*
41	*19*	*-95*	*-11*	*42*	*14*	*-97*	*-6*	*43*	*-35*	*-74*	*-17*	*44*	*43*	*-77*	*-18*
45	*10*	*-69*	*28*	*46*	*49*	*-65*	*19*	*47*	*-44*	*-25*	*32*	*48*	*-4*	*-16*	*37*
49	*-58*	*-11*	*-21*	*50*	*59*	*-25*	*2*	*51*	*-46*	*-44*	*26*	*52*	*-35*	*7*	*27*
53	*21*	*-77*	*28*	*54*	*40*	*28*	*-25*	*55*	*54*	*-56*	*-25*				

Table 3.2. The distributions of 55 landmarks on the brain.

Name of the lobe	*Number of the landmarks*	*Name of the lobe*	*Number of the landmarks*
Occipital	*24*	*Temporal*	*10*
Parietal	*8*	*Posterior*	*5*
Frontal	*4*	*Limbic*	*3*
Insular	*1*		

Table 3.3. The number of the landmarks for main functional behaviors.

Behavioral domain	*Number of landmarks*	*Behavioral domain*	*Number of landmarks*
Cognition	*46*	*Perception*	*26*
Language	*23*	*Vision*	*18*
Emotion	*18*	*Action*	*16*
Memory	*15*		

3.4. Discussion and Conclusion

In this work, the connectome-scale structural and functional profiles is jointly represented via an efficient computational framework for identification of consistent cortical landmarks in human brains. In this framework, functional profiles are first used to localize the initial landmarks for each functional network and each subject, instead of using random initialization or manual labelling as in the previous DICCCOL systems. In this way, initialized landmarks have functional correspondences, and thus they provide a foundation for the joint representation of connectome-scale structural profiles and functional profiles afterwards. Next, for each corresponding initial landmark across all the subjects, ROIs will be established by combining functional and structural profiles, and groupwise registration method is used to significantly reduce the cross-subject variability of the initialized ROIs. Finally, the optimization step is applied to identify the final location of each landmark in each individual brain. We have successfully identified 55 consistent and common cortical landmarks, which can represent a common structural and functional cortical architecture.

The proposed framework could be improved and enhanced in the following directions in the future. First, the number of consistent functional networks used to initialize the landmarks can be significantly increased with the advancement of the HAFNI system. In this work, only 32

consistent and common HAFNI networks were used to select the functional peak foci. In the future, many more HAFNI networks could be discovered and reproduced across individuals and populations, which can be directly used in this landmark discovery framework. Second, in the current study, we focused on the methodology development of joint representation of connectome-scale structural and functional profiles. The potential applications of this framework in clinical fMRI/DTI datasets, e.g., for diagnosis of Alzheimer's disease and Autism, are left to our future studies. For brains with more severe pathologies such as those in brain tumors and stroke, our methods might not be applicable, and as a result, more specific methods should be designed and applied, which could be another possible topic for our future works. We hypothesize that the joint representation of structural and functional cortical architecture by the method proposed in this work can find significant values in those clinical applications by elucidating the altered cortical architectures in brain diseases. Third, in addition to the HCP data, other datasets with both fMRI and DTI modalities can be used and evaluated by our framework in this work. That is, our methods are applicable to a variety of multimodal DTI/fMRI datasets, once the functional networks and structural connectivity patterns can be reliably derived from both modalities.

In summary, we proposed a novel framework for discovering and representing consistent and common cortical landmarks in human brains, and also demonstrated the effectiveness and reproducibility of this representation. This new representation could be potentially widely applicable in many cognitive and clinical neuroscience applications in the future.

Acknowledgement

Funding: This research was supported by the National Institutes of Health (DA-033393, AG-042599) and by the National Science Foundation (NSF CAREER Award IIS-1149260, CBET-1302089, BCS-1439051 and DBI-1564736).

CHAPTER 4

EXPLORING FIBER SKELETONS VIA JOINT REPRESENTATION OF FUNCTIONAL NETWORKS AND STRUCTURAL CONNECTIVITY [3]

[3]Shu Zhang, Tianming Liu, Dajiang Zhu, Exploring Fiber Skeletons via Joint Representation of Functional Networks and Structural Connectivity. International Conference on Medical Image Computing and Computer-Assisted Intervention (MICCAI). Accepted by MICCAI 2018. Reprinted here with permission of publisher, June 6, 2018.

Abstract

Studying human brain connectome has been an important, yet challenging problem due to the intrinsic complexity of the brain function and structure. Many studies have been done to map the brain connectome, like Human Connectome Project (HCP). However, multi-modality (DTI and fMRI) brain connectome analysis is still under-studied. One challenge is the lack of a framework to efficiently link different modalities together. In this chapter, we integrate two research efforts including sparse dictionary learning derived functional networks and structural connectivity into a joint representation of brain connectome. This joint representation then guides the identification of the main skeletons of whole-brain fiber connections, which contributes to the better understanding of the architecture of structural connectome and its local pathways. We applied our framework on the HCP multi-modal DTI/fMRI data and identified main skeleton of whole-brain fiber connections and their 11 local common fiber skeletons, both main skeleton of whole-brain fiber connections and their local fiber pathways are functionally and structurally consistent across individual brains.

4.1 Introduction

Understanding the brain connectome has been significantly important in cognitive and clinical neuroscience (Van Essen et al., 2013; Sporns et al., 2005; Wang et al., 2013). It is fundamentally critical for researchers to understand the organizational architecture of human brains from both structural and functional perspective. With advanced neuroimaging techniques such as MRI, we are able to detect and estimate brain structure/function in vivo. When mapping brain connectivity, functional MRI (fMRI) and Diffusion Tensor Imaging (DTI) are two modalities commonly used. Based on fMRI and DTI datasets, many studies have been done to

investigate the brain connectome using either functional interactions, e.g. correlations (Finn et al., 2015), partial correlations (Zhang et al., 2011) and regression (Zhu et al., 2013), or the strength of white matter connections (Duffau et al., 2015), solely. Numerous reports also have indicated that the structural connectivity patterns "connectional fingerprint" of brain areas can largely determine what functions they perform (Passingham., 2002). However, multimodal (DTI and fMRI) brain connectome analysis is still under-studied. The challenge is the lack of an efficient framework that can integrate the knowledge from two different modalities together.

Here, the proposed computational framework integrates two lines of research efforts including sparse dictionary learning derived functional networks and DTI derived fiber based structural connectivity into a joint representation of brain connectome. In this way, functional connectivity and structural connectivity can be studied and analyzed simultaneously. As illustrated in Figure 4.1, we applied our framework on the Human Connectome Project (HCP) multimodal DTI/fMRI datasets to detect the main skeleton of the white matter pathways that are most active when performing different brain functions. 11 major local fiber patterns are also identified from the main skeleton which have both functional and structural consistency across multiple individuals. The derived white matter skeleton and its local fiber patterns provide a new way to study brain connectome via multimodalities of MRI and shed novel insights on integrating brain structural and functional information.

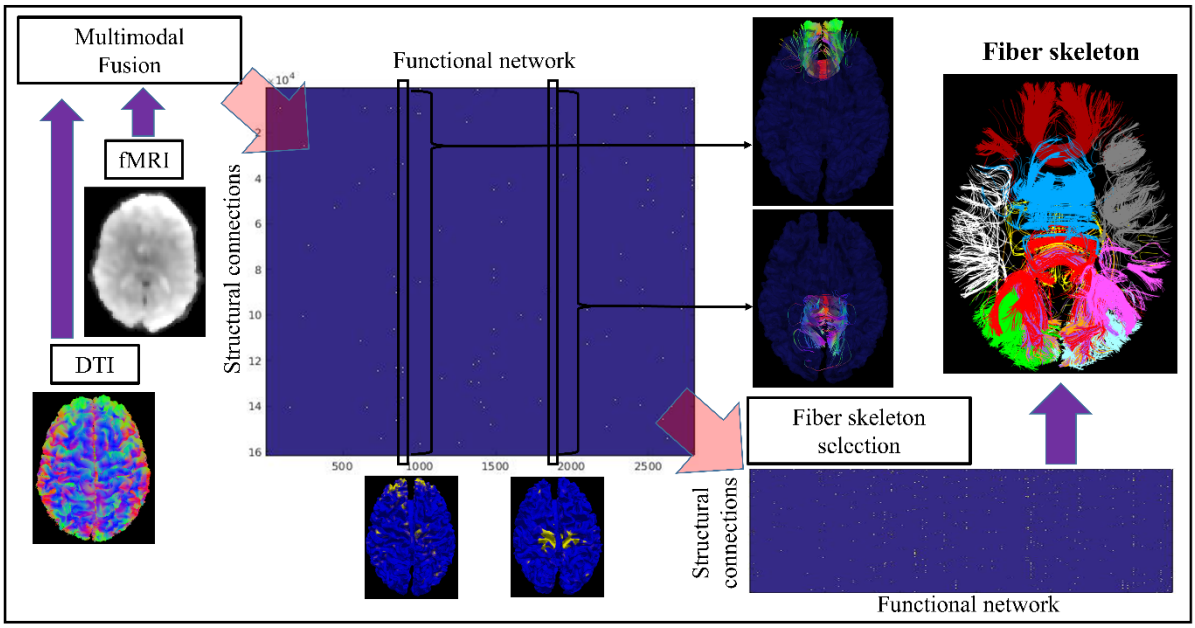

Figure 4.1. The proposed framework of joint representation of functional networks (based on fMRI data) and structural connectivity (based on DTI data) to explore the fiber skeleton. Two main steps are provided, one step is multimodal fusion, another main step is fiber skeleton selection.

4.2 Materials and Methods

4.2.1 Data Acquisition and Preprocessing

For this study the data from HCP 1200 Subjects Data Release (Van Essen et al., 2013) which has seven task-fMRI datasets of 50 participants is used. The tasks include working memory, gambling, motor, language, social cognition, relational processing and emotion processing. For task-fMRI, the acquisition parameters are as follows: 72 slices, TR=0.72s, TE=33.1ms and 2.0 mm isotropic voxels. The acquisition parameters were as follows: 2×2×2 mm spatial resolution, 0.72s temporal resolution and 1,200 time points. For DTI data, spatial resolution=1.25mm×1.25mm×1.25mm. More details of data acquisition and preprocessing may be found in (Woolrich et al., 2001).

4.2.2 Representation of Functional Networks

A brain functional network can be defined as the brain regions that functionally "linked" (Sporns et al., 2004). It has been proven that the dictionary learning and sparse coding approaches are able to successfully identify task-related and resting state brain functional networks even when they have overlaps in both spatial and/or temporal domain (Lv et al., 2015a; Zhang et al., 2013). Based on online dictionary learning (ODL), the whole-brain fMRI signals can be represented as a linear combination of a relatively small number of dictionary signals. The major steps are illustrated in Figure 4.2. Firstly, the whole-brain normalized signals are arranged into a matrix X (Figure 4.2A) with *n* columns (*n* voxels) and each column contains a single fMRI signal with length of *t* (*t* time points). Then X is decomposed into two parts: dictionary matrix D (Figure 4.2B) and a sparse coefficient matrix α (Figure 4.2C). The empirical cost function is summarized in (1), and its aiming of sparse representation using D, $\ell(x_i, D)$ is defined in (2), where λ is a regularization parameter to trade off the regression residual and sparsity level.

$$f_n(D) \triangleq \frac{1}{n}\sum_{i=1}^{n} \ell(x_i, D) \tag{4-1}$$

$$\ell(x_i, D) \triangleq \min_{\alpha^i \in R^m} \frac{1}{2}\|x_i - D\alpha_i\|_2^2 + \lambda\|\alpha_i\|_1 \tag{4-2}$$

Each element of α indicates the extent when the corresponding dictionary atom is involved in representing the actual fMRI signals. As a result, each row of α can be mapped back to the brain volume space as a functional brain network pattern (Figure 4.2C). Because 400 was proven to be an appropriate number of dictionary size for HCP Q1 dataset (Lv et al., 2015a), in this work 400 is set for all task fMRI data. Thus, for each HCP subject, 2,800 functional networks will be obtained from seven tasks.

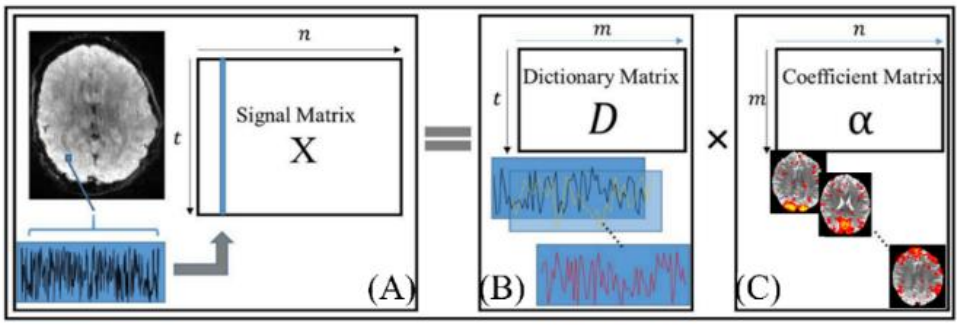

Figure 4.2. The framework of applying ODL algorithm onto the fMRI signals. (A) Obtain signals from fMRI images. (B) Dictionary matrix. (C) Coefficient matrix.

4.2.3 Representation of Structural Connectivity

In this section, we explored DTI derived fibers connecting to the activated areas of each functional network. Since the fibers are under the DTI space, we need to register the individual fMRI data to its own DTI space. Here we adopted a widely used linear registration tool – FLIRT from FSL (Jenkinson et al., 2001). White matter surface can be obtained through the DTI tissue segmentation and DTI cortical surface reconstruction algorithms (Liu et al., 2008). Then we mapped the voxel from the registered fMRI data to its nearest vertex on the cortical surface and thus each surface vertex can be linked to the corresponding functional intensity in the decomposed coefficient matrix in Section 4.2.2. At last, for each cortical surface labeled with functional intensity values, we will examine the whole brain fibers and extract every fiber if both of its ending locations connected to activated regions on cortical surface. A threshold T=0.5 is used to judge if a vertex on the cortical surface is active or not. Similar to the threshold in task activation detection (Lv et al., 2015a), T is set empirically in this work. In this way, the fiber bundles which include all the connections from the activation area of different functional networks could be extracted. A vector N_i can be used to represent the fiber connection of the corresponding functional network i:

$$N_i^j = [f_1, f_2, f_3 \dots f_{n-1}, f_n] \quad (4\text{-}3)$$

where *i* represents the *i*-th functional network, *j* represents the subject index, *f* represents a fiber which is from the whole brain fibers and *n* is the total number of the fibers of subject *j*. The value f will be set to 1 if this fiber has a connection to the *i*-th functional network and 0 otherwise.

4.2.4 Joint Representation of Functional Networks and Structural Connectivity to Identify Main Skeleton of the Brain Connections

In this section, we introduce a novel joint representation approach to integrating the functional and structural connectivity together to explore the main skeleton of fiber connectomes. In the Section 4.2.3, registered functional networks and the related fiber connections can be obtained, here, each fiber connection pattern we achieved was from a single functional network. However, the human brain is widely considered to include a collection of specialized functional networks flexibly interacting when different brain functions are performed (Fair et al., 2009). Thus, instead of studying a single connection pattern derived from single functional network, the need is to find a way to discover the fiber connectome in a global vision. In this work, instead of working on the overlap of the functional networks, we focus on the overlap of fibers. A matrix Y is generated for each subject:

$$Y \in \mathbb{R}^{m*n} \quad (4\text{-}4)$$

n represents the total number of fibers, *m* is the total number of functional networks (2,800 in this work) for each subject and N_i defined in Section 4.2.3 is one row from Y. Each row of Y represents the fiber connections for a single functional network and each column represents the functional networks connecting to the corresponding fibers. Then, the statistics of the elements in each column of the matrix Y can be conducted, thus a histogram vector H can be computed:

$$H = [h_1, h_2, h_3 \dots h_{n-1}, h_n], \; h_i = \sum_{j=1}^{2800} y_{j,i} \quad (4\text{-}5)$$

where h_i is the total number of functional networks that fiber *i* participated, and the more networks *i* participated, the more activated intensity *i* is. Having the fiber connectome matrix Y and its histogram vector H, then we can rank those fibers from most activated fibers to the least activated fibers. Thus, we could identify which fibers tend to be more activated in the functional networks and use them to generate a main skeleton of the brain connectomes. An example named "Fiber skeleton" is shown in the Figure 4.1. It contains 5000 most activated fibers across the whole brain fiber pathways. In order to examine the consistency of the skeleton obtained, the approach is applied on HCP data.

4.2.5 Local Connectome Analysis Based on the Main Skeleton of the Brain Connectomes

The skeleton of brain connectomes describes the main connections across the major brain regions. More importantly, it represents the most commonly used fibers and their connection pathways in multiple functional networks. In order to better understand the main skeleton, further analysis is performed to investigate the local brain areas and connections that the skeleton connects to. To analyze the main skeleton, here we only focus on the fibers from the main skeleton obtained from Section 4.2.4 and examine the relationship between those fibers and functional networks. The main skeleton fiber connection matrix is defined as Y_s:

$$Y_s \in R^{m*n'} \tag{4-6}$$

where n' is the number of fibers from the main skeleton. We extracted each row of Y_s and studied the corresponding functional networks and fiber connections as well. A groupwise k-means clustering algorithm will be adopted on Y_s, local fiber pattern will be identified from equation:

$$c^i := arg\min_j \left\|x^i - \mu_j\right\|^2,\ \mu_j := \frac{\sum_{i=1}^{m} 1\{c^i=j\}x^i}{\sum_{i=1}^{m} 1\{c^i=j\}} \tag{4-7}$$

where *c* is the cluster of *i*, μ_j is the center of cluster *j*, *x* is the sample data. It is worth noting that groupwise k-means clustering algorithm mentioned above means same initial clustering centers

will be used across the subjects to do the clustering for each subject. Only in this way, the clusters from different subjects could have correspondence among each other. The initial clustering centers for all the subjects come from the final k-means clustering center of one template subject.

Here, the emphasis is that the total number of the k-means clusters is defined through Principal component analysis (PCA) of those main skeleton fibers obtained from each individual. Using main skeleton with 5000 fibers as an example, very impressively, the number of the principle components is very robust and is fixed on 11 across the subjects. Thus, the number of the groupwise k-means clusters is set to 11 in this work.

4.2.6 Structural Connections Consistency Analysis of Local Fiber Patterns

In this work, the 'trace-map' of DTI-derived axonal fiber bundles (e.g., as similar to those in the literature (Zhu et al., 2012a; Chen et al., 2013; Gorski et al., 2005) is adopted to represent the brain fiber patterns. Here, the 'trace-map' representation and comparison of the DTI-derived structural fiber connection pattern is briefly demonstrated. The "trace-map" method is shown in Figure 4.3 by projecting each beginning and ending point for each fiber from fiber bundles (Figure 4.3b) onto the uniform spherical surface. Then we divide the surface into 48 equally areas and construct histogram for each area, and list them as the vectors. A 48 dimensional histogram vector $tr = [d_1, d_2 \ldots d_{48}]$ containing 48 density values, namely 'trace-map' (Figure 4.3d), is finally obtained as the structural connectivity profile of a landmark.

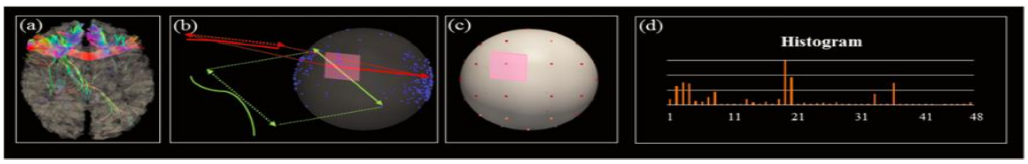

Figure 4.3. Pipeline of 'trace-map' representation of the fiber bundle of the landmark for representation of structural profile. (a) An example of fiber bundle and cortical surface. (b)

Points distribution by projection of the principal orientation of each fiber in the fiber bundle on the uniform spherical surface. (c) 48 equally areas from one uniform spherical surface are represented. (d) 48 vectors are used to represent one fiber bundle.

Using the trace-map method, fiber bundles can be represented by a one dimensional vector, it will be more convenient and efficient to do the comparison between different fiber bundles. Thus, Pearson correlation is adopted here to compare the similarity of different fiber patterns using their unique trace-map vectors.

4.2.7 Functional Consistency Analysis of Local Fiber Patterns

In this work, functional consistency will be measured through overlap rate between different functional networks. In details, to compare the overlap between different functional networks, two steps are included. The first step is to collect functional networks which are corresponding to the certain local fiber pattern. Specifically, the structural connection for each functional network has been recorded. Thus, regarding to specific local fiber pattern, by going through all the structural connections of all the functional networks, those functional networks which cover that local fiber pattern are picked up. The second step is to register those picked up functional networks onto the standard template and then calculate the overlap rate of those registered functional networks. It is worth noting that it is quite straightforward to calculate the overlap rate of those registered functional networks. In this chapter, Jaccard overlap rate is adopted to calculate the similarity from networks, it is represented as below:

$$J(A,B) = \frac{|A \cap B|}{|A|+|B|-|A \cap B|} \tag{4-8}$$

where A and B are the different functional networks. For each local fiber pattern, related functional networks are picked up across the subjects and average Jaccard overlap rate is

calculated among those functional networks. Higher Jaccard overlap rates will show higher correlation among those functional networks.

4.3 Experimental Results

4.3.1 The Main Skeleton of the Fiber Connections of Human Brain

According to Section 4.2.2 to 4.2.4, the main skeleton of the fiber connections from one subject is obtained at three different connectome levels, which are shown in Figure 4.4. Three different connectome levels have 500 fibers (Figure 4.4B), 5,000 fibers (Figure 4.4C) and 10,000 fibers (Figure 4.4D), respectively. Although the number of the extracted fibers is largely different, the connectome pathway is relative robust as found. For example, the fiber connections in the frontal lobe are obvious and consistent across those three levels. These connectome pathways are named as the skeleton of the fiber connections of human brain. It needs to be emphasized that, in this work, we use the main skeleton with level of 5,000 fibers as the standard and further analyses are also based on this level. The reason of choosing level of 5000 is that it has the clearness and robustness of the fiber connectome pathway. In details, level of 500 occupies only 0.25% from whole brain fibers, thus this number is too small to clearly and completely represent the connectome pathway. Level of 10,000 holds about 5% fibers from whole brain, but among those 10,000 fibers, some fibers are not very active, thus the sparsity of the connection matrix Y is only about 0.0035, which is too small from the experience. In contrast, level of 5,000 accounts for nearly 2.5% and the sparsity of the connection matrix is about 0.008, thus, level of 5000 is chosen.

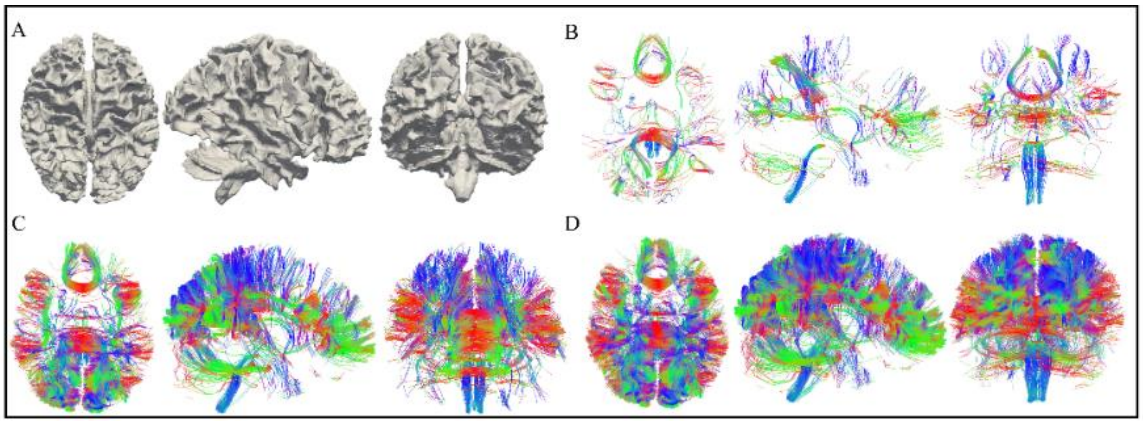

Figure 4.4. The main skeleton of the fiber connections of one individual case. (A) The cortical surface of the brain. (B) Main skeleton of the fiber connections on level of 500. (C) Main skeleton of the fiber connections on level of 5,000. (D) Main skeleton of the fiber connections on level of 10,000.

4.3.2 The Consistency of the Main Skeleton of the Fiber Connections Across Different Subjects

In order to check the robustness of the main skeleton of the fiber connections we obtained, we adopted our framework on HCP dataset. The main skeletons are obtained for each subject and 24 of them are shown as examples in Figure 4.5 to present their consistency across the subjects.

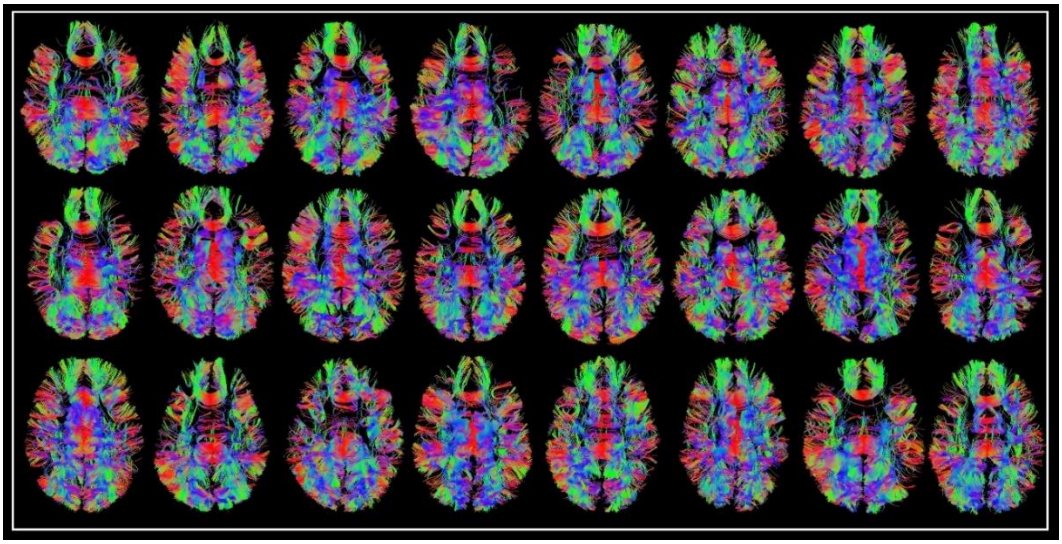

Figure 4.5. The main skeleton of the fiber connections of 24 subjects on level of 5000. Each main skeleton is shown separately.

From Figure 4.5, it can be seen that the main skeleton of the fiber connections is clear and consistent across the subjects. Compared with whole brain fibers (as shown in Figure 4.1), these 5,000 most activated fibers describe clearer connectome pathway for the fiber connectomes. Those connections represent the most important connection patterns under task performance and they connect significant brain regions. This result is interesting, since the functional networks and whole brain fibers are from each individual and the way to obtain main skeletons is totally possessed individually. Impressively, the patterns of the skeleton are quite similar across these subjects. By adopting the trace-map method from 4.2.6, the average similarity of those main skeleton of fiber connections is obtained and listed in Table 4.1. To our best knowledge, results successfully demonstrated the consistency of those main skeleton of the fiber connections.

Table 4.1 Similarity of fiber skeleton across the subjects using trace-map algorithm

Mean	0.6195
Standrad Deviation	0.1790

4.3.3 Explore Major Local Fiber Patterns from the Main Skeleton of the Fiber Connections

Using the approaches from the Section 4.2.5, fiber connections for each functional network at the level of 5,000 fibers from Y_s can be obtained, and the aim is to investigate how the main skeleton of the fiber connections participated in the functional networks. Thus, for each subject, equation 4-7 will be applied on the corresponding main skeleton fiber connection matrix Y_s. After applying the groupwise k-means algorithm to cluster the main skeleton fiber connections, 11 major local patterns are identified from the main skeleton and are shown in the

Figure 4.6B. These local patterns are reasonably consistent across subjects, and they compose the main skeleton.

To show the consistency of those local fiber patterns, 6 subjects are randomly picked up and their 11 local fiber patterns are presented in Figure 4.7 accordingly. In addition, the similarity of every local fiber pattern across the subjects is measured through trace-map method, the results are summarized into Table 4.2. By checking the results from Figure 4.7 and Table 4.2, we can infer that not only the main fiber skeleton is consistent across the subjects, their local fiber patterns are also consistent.

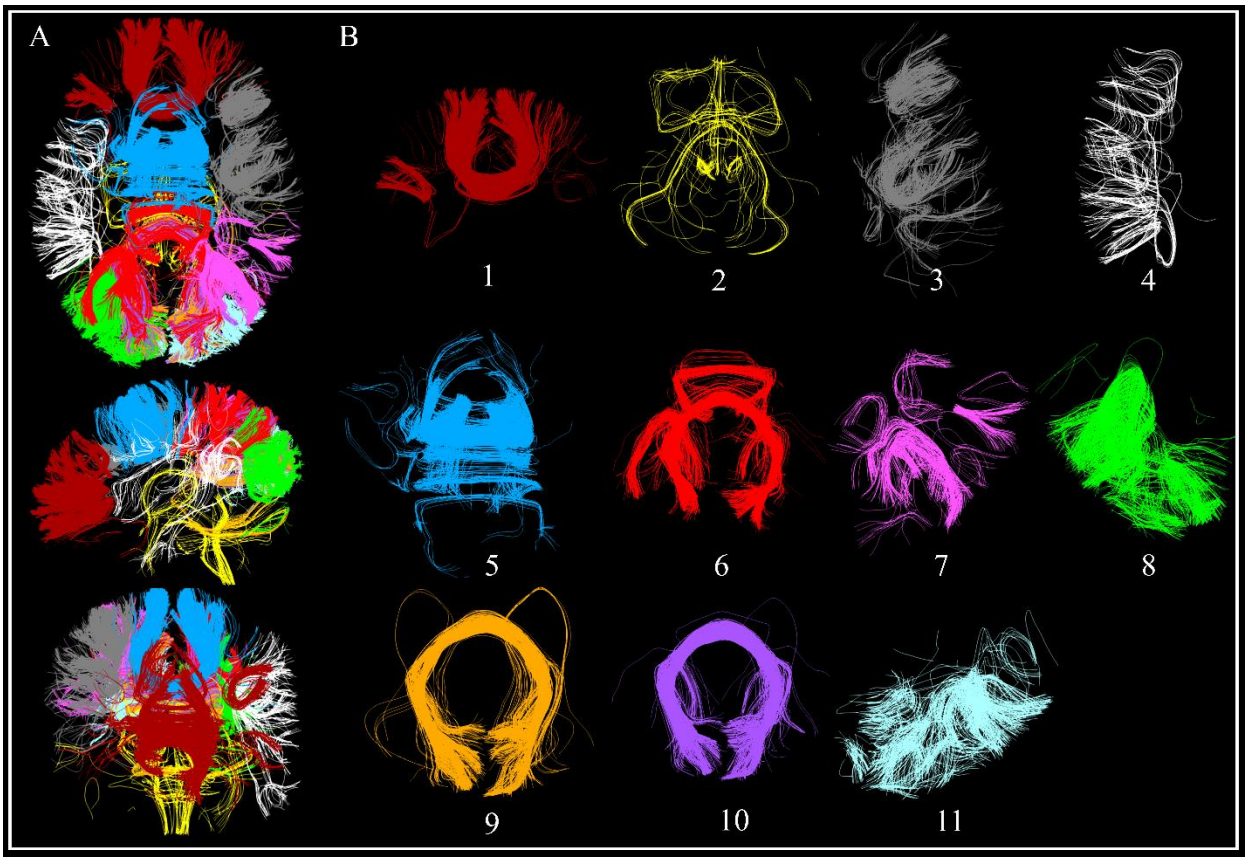

Figure 4.6. An example of the main skeleton and its local fiber patterns. (A) The main skeleton of the fiber connections. (B) 11 consistent local fiber patterns. Index of local pattern is provided.

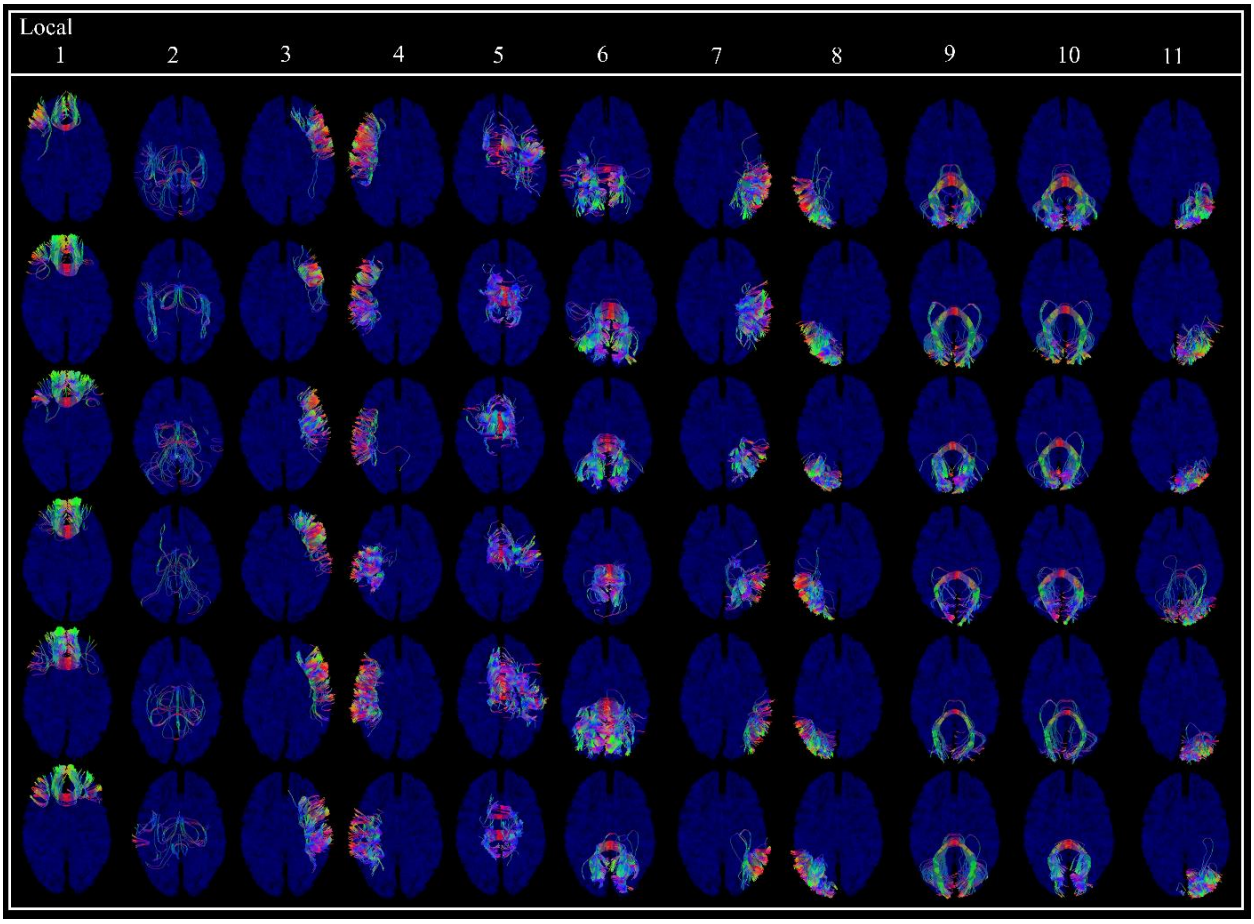

Figure 4.7. Local fiber patterns across the subjects. Each row represents the 11 local fiber patterns from one subject. Six subjects are randomly picked up. Index of the local fiber patterns are provided too.

Table 4.2. Similarity of local fiber patterns across the subjects through trace-map algorithm.

Cluster	1	2	3	4	5	6	7	8	9	10	11
Mean	0.61	0.37	0.45	0.36	0.68	0.52	0.3	0.44	0.60	0.55	0.36

4.3.4 Corresponding Functional Networks for Major Local Patterns

It is interesting to know whether the corresponding functional networks of those local fiber connections are consistent. It is worth noting that local pattern fibers are from the main skeleton fiber connection matrix Y_s. However functional networks are corresponding to the

whole brain fiber connection matrix Y, $Y \gg Y_s$. So it is not necessary that the corresponding functional networks of same local pattern fibers must be consistent. To exam functional consistency of local patterns, the fiber connections from Y_s and their corresponding functional networks are retrieved. We use local pattern #9 from Figure 4.6 as an example and illustrate them in Figure 4.8. From Figure 4.8, it is observed that the activation areas are consistent, and located in the occipital lobe. That is, for those local patterns, their corresponding function networks are also consistent. In addition to the local pattern #9 in Figure 4.6, other major local patterns have similar characteristics. Here, another three examples (Figures 4.9-4.11) are provided to show their consistency. Moreover, Jaccard overlap rate of these corresponding functional networks is calculated respectively and summarized into Table 4.3. From Table 4.3, it can be seen that for each local fiber pattern, the Jaccard overlap rate of their corresponding functional networks is about 0.3, which is quite a high value from our experience. Based on above experiments, it can be concluded that the local fiber patterns obtained from main skeleton of the fiber connections have both structural consistency and functional consistency.

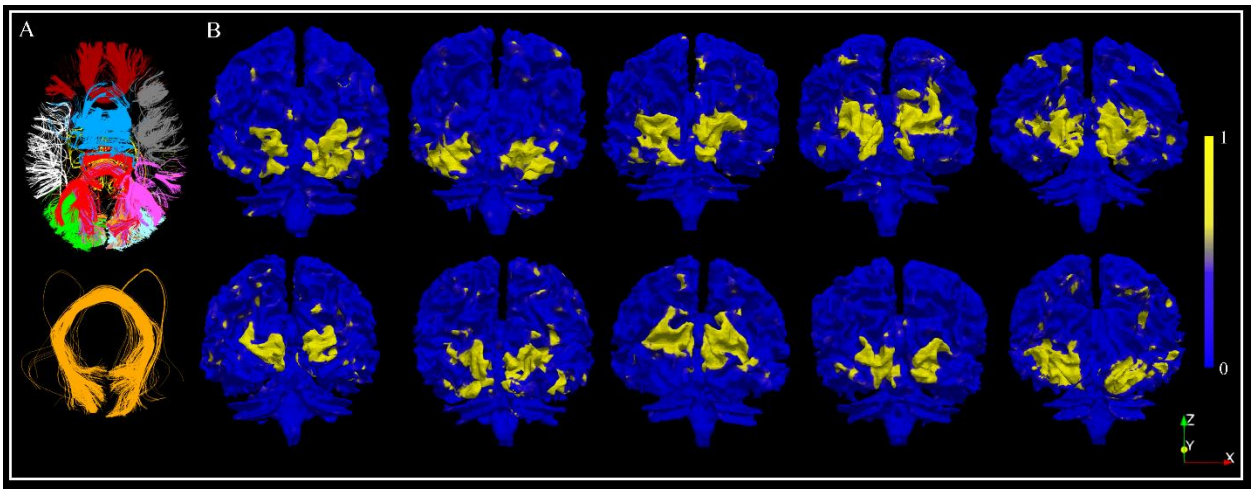

Figure 4.8. Local fiber pattern and its related functional networks. (A) An overview of fiber skeleton and an example of the local fiber pattern (B) Functional networks which corresponding to the local fiber patterns across the subjects. Color bar is shown on the right.

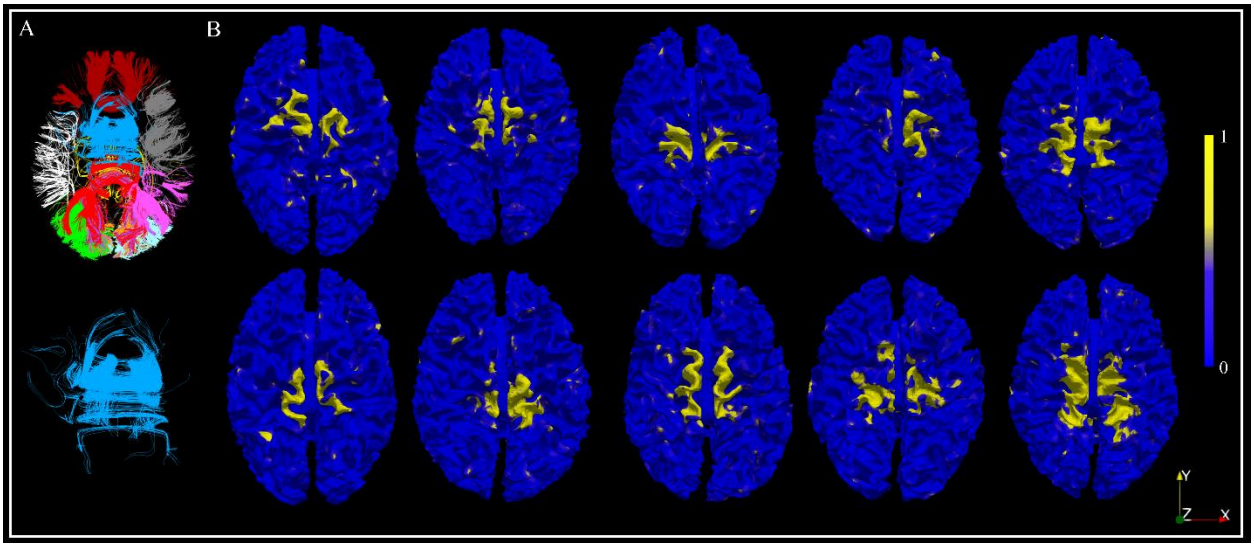

Figure 4.9. Local fiber pattern and its related functional networks. (A) An overview of fiber skeleton and an example of the local fiber pattern (B) Functional networks which corresponding to the local fiber patterns across the subjects.

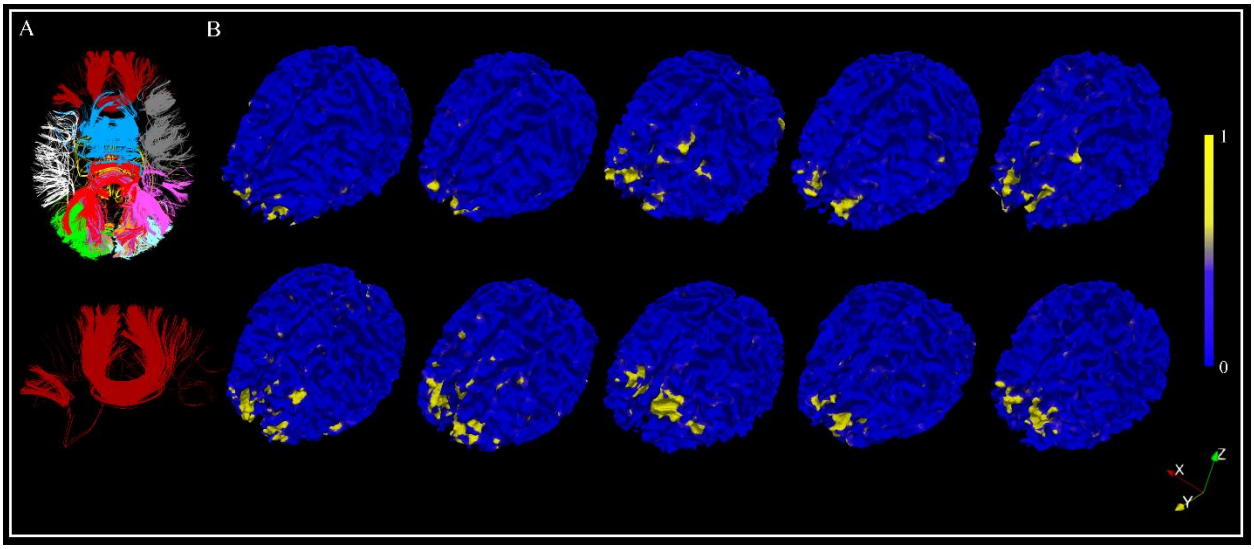

Figure 4.10. Local fiber pattern and its related functional networks. (A) An overview of fiber skeleton and an example of the local fiber pattern (B) Functional networks which corresponding to the local fiber patterns across the subjects.

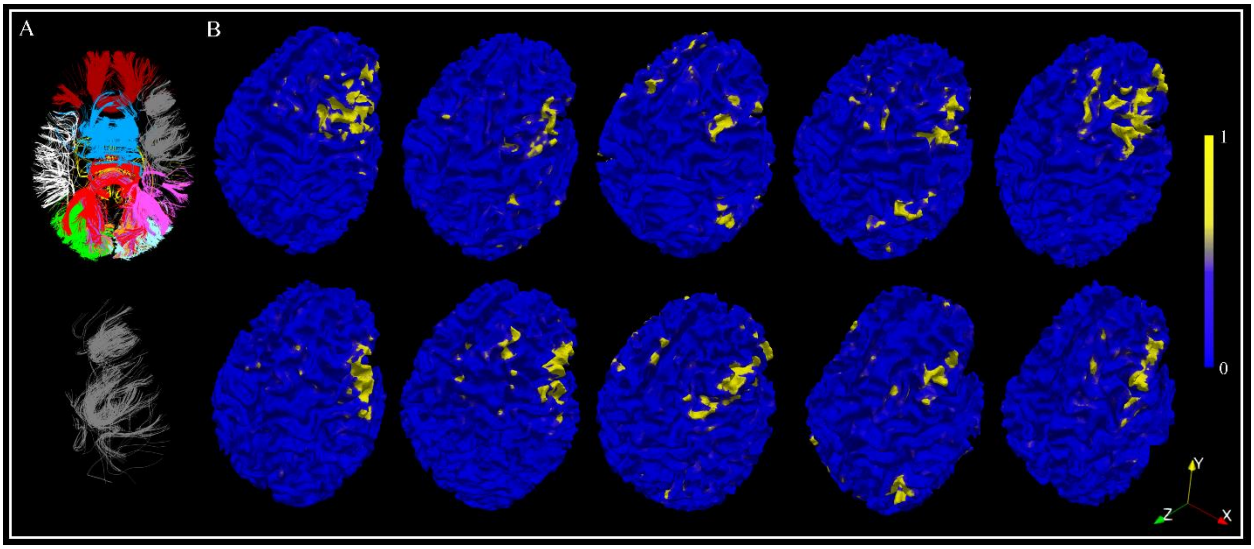

Figure 4.11. Local fiber pattern and its related functional networks. (A) An overview of fiber skeleton and an example of the local fiber pattern (B) Functional networks which corresponding to the local fiber patterns across the subjects.

Table 4.3. Average Jaccard overlap rate of functional networks which corresponding to the local fiber patterns.

Cluster	1	2	3	4	5	6	7	8	9	10	11
Mean	0.27	0.25	0.26	0.36	0.38	0.30	0.30	0.32	0.35	0.35	0.32

4.4 Discussion and Conclusion

In this chapter, we proposed a novel framework for joint representation of structural connectivity and functional networks to explore the fiber skeleton of the brain. The major advantage of our framework is that it enables learning connections by multimodality (both fMRI and DTI) to investigate the most activated fibers and then derive the main skeleton of fiber connections. The analysis of the framework on HCP multimodal DTI/fMRI data suggests that main skeleton of the fiber connections can be robustly identified. In addition, through studying the main skeleton of the fiber connections, typical local patterns can be discovered and studied. Those local fiber patterns and their connected brain regions show great consistency both on the

structural and functional perspective, thus, they can be used to generate common architecture of the human brain at the local region scale.

For the 11 major local patterns, some local fiber patterns are always shown on the same functional network, meaning that some functional networks have much stronger activation levels and they may include 2 or more simpler functional networks, e.g. # 6, #9 and #10 from Figure 4.6. This is an interesting evidence for the hierarchical theory of functional networks. Another interesting finding is about the fiber connectome between left and right hemispheres. As #1, #5, #6, #9 and #10 from Figure 4.6, the main fiber connections between left and right hemispheres are from corpus callosum. Apart from corpus callosum, there are many fiber bundles connecting left and right hemispheres, however, they do not belong to the main skeleton. In summary, those local patterns will help to not only present both functional and structural consistency across the subjects, but also provide a new insight to understand the mechanism of the fiber connectome of the brain.

Acknowledgement

T. Liu was supported by NIH DA033393, NIH AG042599, NSF IIS-1149260, NSF CBET-1302089 and NSF BCS-1439051.

CHAPTER 5

DISCOVERING HIERARCHICAL COMMON BRAIN NETWORKS VIA MULTIMODAL DEEP BELIEF NETWORK[4]

[4]Shu Zhang, Qinglin Dong, Wei Zhang, Heng Huang, Dajiang Zhu, Tianming Liu. Discovering Hierarchical Common Brain Networks via Multimodal Deep Belief Network.

Submitted to IEEE Transactions on Medical Imaging, May 21, 2018.

Abstract

Studying a common architecture reflecting both brain's structural and functional organizations across individuals and populations in a hierarchical way has been of significant interest in the brain mapping field. Recently, deep learning models exhibited superiority in extracting meaningful hierarchical structures from brain imaging data, e.g. fMRI and DTI. However, deep learning models have not been used to explore the relation between brain structure and function yet. In this chapter, a novel multimodal deep believe network (DBN) model is proposed to discover and quantitatively represent the hierarchical organizations of common and consistent brain networks from both fMRI and DTI data. A prominent characteristic of DBN is that it is able to extract meaningful features from complex neuroimaging data with a hierarchical manner. With this proposed DBN model, three hierarchical layers of hundreds of common and consistent brain networks across individual brains are successfully constructed through learning a large dimension of representative features derived from fMRI/DTI data.

5.1 Introduction

Inspired by the relation of brain structure and function (e.g. Passingham et al., 2002; Von, 1994), constructing a common architecture reflecting both brain's structural and functional organizations across individuals and populations has been of significant interest in the brain mapping field. With the help of advanced multimodal neuroimaging techniques, whole-brain structural (e.g., mapping fiber connections using diffusion tensor imaging (DTI) (Le et al., 1985; Hagmann et al., 2003; Schmahmann et al., 2007; Hagmann et al., 2008; Zhu et al., 2012a; Zhu et al., 2014b; Jiang et al., 2015b; Zhang T et al., 2016)) and functional profiles (e.g., mapping

functional localizations using functional MRI (fMRI) (Ogawa et al., 1992; Belliveau et al., 1991; Calhoun et al., 2001; Beckmann et al.,2005; Calhoun et al., 2009; Lv et al., 2015a; Zhao et al., 2015; Zhang S et al., 2016; Zhao et al., 2016)) of the brain are able to be quantitatively represented, for instance, from a structural perspective, our previous studies have identified hundreds of cortical landmarks across different populations, each of which possesses consistent DTI-derived fiber connectivity patterns (Zhu et al., 2012a). Meanwhile, functional connectome-scale brain networks were also effectively and robustly reconstructed by using sparse learning method applied to fMRI data (Lv et al., 2015a).

Multimodal fusion is becoming more and more popular to study the brain functional and structural information simultaneously. Given the complementary information embedded in structural and functional connectomics data, it is natural and well-justified to combine multimodal information together to investigate brain connectivities and their relationships simultaneously (Chen et al., 2013; Zhu et al., 2014a), for instance, Zhang et al. (2017a) and Zhang et al. (2017b) proposed novel multimodal fusion frameworks to identify common and consistent cortical landmarks by jointly representing connectome-scale functional and structural profiles from the brain; Zhang et al. (2018a) proposed a novel multimodal fusion framework to explore the relationship among cortical folding, structural connectivity and functional networks, they observed that structural connectivity based brain parcellations and sparse dictionary learning derived functional networks exhibited deeply rooted regularity across individuals, but cortical folding patterns were substantially more variable; Zhang et al. (2018b) also proposed a novel framework to explore fiber skeletons via joint representation of functional networks and structural connectivity. This joint representation guided the identification of the main skeletons

of whole-brain fiber connections, which contributed to a better understanding of brain architecture of structural connectome and its local pathways.

So far, based on the existing multimodal fusion studies (e.g. Zhu et al., 2014b; Sui J et al., 2012; Rykhlevskaia et al., 2008, Zhang et al., 2017a and Zhang et al., 2017b, Zhang et al., 2018), we strongly believe that multimodal brain connectomics research will revolutionize the fundamental understanding of the structure and function of the brain and their relationships, and eventually shed novel insights into how to treat, cure, and prevent many devastating brain disorders. However, multimodal integration of brain connectomics is also widely considered a grand challenge due to the significant variability across individuals and populations, both on spatial and temporal perspective (He et al., 2013). Because of the requirement of tremendous computing ability, those variabilities will be hardly measured from abovementioned models when more precise and comprehensive analysis is needed. Hence, it is a huge barrier for researchers to further reveal the fundamental understanding of the brain structure, function and their relationships.

Inspired by recent great success of deep learning methods and their superb computing power (Bengio et al., 2012; Goodfellow et al., 2014; Graves et al., 2013; Greff et al., 2017; He et al., 2016; He et al., 2017; Hinton 2002; Hinton et al., 2006; Hinton and Salakhutdinov 2006), recently, our group has developed several deep learning models, such as 1D CNN model for fMRI time series (Huang et al., 2017), RBM and DBN models for fMRI time series data (Hu et al., 2018; Lei et al., 2018), 3D CNN models for spatial brain networks, and applied them on fMRI data (Zhao et al., 2017a, Zhao et al., 2017b, Zhao et al., 2018). Our previous studies have showed that deep learning models exhibited superiority in extracting meaningful hierarchical structures from fMRI data, for instance, Huang et al. (2017) has proved that their Deep

Convolutional Auto-Encoder (DCAE) model is superior in representing fMRI signals, and as the model goes deeper, a better abstraction of data can be achieved; Li et al. (2018) has proposed a blind source separation (BSS) model based on DBN with two hidden layers of RBM, their experimental results showed that the proposed two layers' model is capable of identifying not only latent components related to distinct brain systems, but also the ones related to functional interactions across brain systems. In parallel, on the structural perspective, Chen et al. (2015) applied hierarchical structures in the 3-D reference atlas of Allen Mouse Brain Atlas to study brain fiber pathways across the individuals. Three different scales were provided, on the finest scale, 300 regions were selected to parcellate the whole mouse brain, these regions were then combined to obtain 96 regions and 69 region parcellation schemes. Their corresponding fiber pathways at different scales have shown that structural brain networks also exhibit hierarchical organization patterns.

However, our previous deep learning models have not explored the relation between brain structure and function yet, thought it has been well known that structural and functional brain networks are closely related. It is even more interesting to explore if/how such multimodal brain networks exhibit hierarchical organization patterns. To achieve the above-mentioned viewpoints, here we proposed a novel computational framework to explore both functional and structural connectivity on voxel level and thus to learn hierarchical latent features and associated representations via Deep Belief Network (DBN) model. Three major advantages of our proposed framework are provided below. First, DBN is famous for its surpassing power in learning hierarchical latent features and associated representations (Brosch et al., 2014; Lee et al., 2009; Palm et al., 2012; Li et al., 2018). In this work, the shallow RBM model is extended as building blocks into a DBN with multi-layer structure to better model the intrinsic hierarchical features of

the brain architecture. Second, deep learning algorithms possess strong learning power: the more training samples we have, the better results we could achieve (Chen and Lin, 2014; LeCun et al., 2015). The proposed voxel level analysis will thus take the advantage of large-scale training samples. Generally speaking, around 100K vertices from one cortical surface are collected from each subject in the Human Connectome Project (HCP) dataset as well as their common features (functional and structural trace-map values) (Chen et al., 2013; Zhu et al., 2012a), with the help of such superb learning power, consistency could be identified from the tremendous variable input data. Third, we proposed a novel multimodal fusion model to combine DTI and fMRI data and then explore common cortical architecture of human brain considering both functional and structural aspects. In the joint model, for each modality, an efficient feature descriptor is developed to describe the corresponding connectivity for each vertex, and representative features for both brain functional and structural information will be generated using the proposed feature descriptors at the voxel level.

In this work, 100, 50 and 25 common brain networks are obtained from 3-layer DBN model, respectively. The number of the networks for each layer is decided by using the low-rank decomposition algorithms (Wen et al., 2012) and will be mentioned later. The obtained common brain networks are proved to be functional and structural consistent across different subjects. Interestingly, obvious hierarchical relationships are observed from layer 1 to layer 3. Moreover, repetitive experiments indicate that our proposed framework works well when using different datasets and most common brain networks are still repeatable. The comparison between hierarchical brain networks and Holistic Atlases of Functional Networks and Interactions (HAFNI) (Lv et al., 2015a) components provides a better way to understand how the hierarchical architecture organized inside brains. More comparison experiments including using meta-

analysis are designed and adopted to examine and interpret obtained common brain networks on both functional and anatomical domains. All of the above analyses suggest that the proposed DBN model can successfully identify the hierarchical architecture of human brains by exploring the common brain networks in each hierarchical layer.

5.2 Materials and Methods

5.2.1 Overview

In this section, we briefly introduce the framework of our proposed method. The flowchart is shown in Figure 5.1 as an illustration of proposed algorithm, details are further shown in each subsection. As shown in Figure 5.1, to explore the hierarchical and common brain networks across populations through multimodalities, our method contains three major steps. The first two steps compute the structural and functional connectivity at voxel level. The third step is to combine those structural and functional connectivity profiles together and feed them into a carefully designed DBN model to discover the hierarchical description of the brain networks.

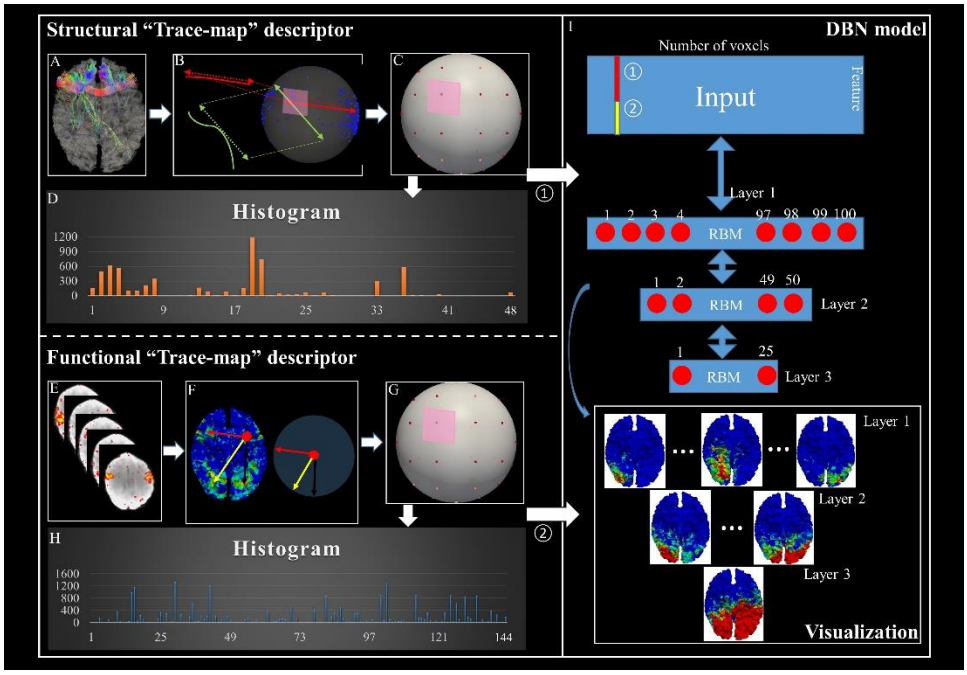

Figure 5.1. The flowchart of the proposed method. (A-D) steps to get the structural trace-map for single vertex. (E-H) steps to get the functional trace-map for single vertex. (I) the 3-layer DBN model using the functional and structural profiles acquired from A-H as the inputs to achieve the hierarchical representation across the subjects. Step A: extracting fiber bundles passing through the seed vertex. Step B: projecting each fiber's direction to a uniform spherical surface. Step C: dividing the surface of sphere into 48 equal areas. Step D: computing the histogram of structure trace-map within each area and generating a feature vector for each seed vertex (Chen et al., 2013). Step E: identifying individual functional brain networks via HAFNI (Lv et al., 2015a). Step F: generating functional connection intensity map for each vertex and then projecting each connection to the uniform spherical surface. Step G: dividing the surface of sphere into 144 equal areas. Step H: computing the histogram of functional trace-map within each area and generating a feature vector for each seed vertex.

5.2.2 Data Description and Preprocessing

The dataset used in this study was obtained from the Human Connectome Project (HCP) (Barch D M, et al., 2013; Van Essen DC, et al., 2013). The acquisition parameters of task fMRI (tfMRI) data are as follows: 90×104 matrix, 220mm FOV, 72 slices, TR=0.72s, TE=33.1ms, flip

angle = 52°, BW=2290 Hz/Px, in-plane FOV = 208×180 mm, 2.0 mm isotropic voxels. For tfMRI images, the preprocessing pipelines included skull removal, motion correction, slice time correction, spatial smoothing, and global drift removal. All of these steps were implemented by FMRIB Software Library (FSL) FEAT (Woolrich et al., 2009). For DWI data, the parameters are as follows: Spin-echo EPI, TR 5520 ms, TE 89.5 ms, flip angle 78 deg, refocusing flip angle 160 deg, FOV 210x180 (RO x PE); matrix 168x144 (RO x PE), slice thickness 1.25 mm, 111 slices, 1.25 mm isotropic voxels, Multiband factor 3, and Echo spacing 0.78 ms. Please refer to (Uğurbil K et al., 2013; Barch D M, et al., 2013) for more details.

5.2.3 Structural Connectivity Descriptor "structure trace-map"

The motivation of designing a structural trace-map descriptor is to measure the similarity of different fiber bundles. The fiber bundles are within 3d space and it is extremely difficult to compare them directly. In this study, the aim is to construct the similarities between the 'trace-maps' of DTI-derived fiber bundles for those initialized landmarks, with a similar way as proposed in Chen H et al., 2013 and Zhu D et al., 2012a. To be self-contained, we briefly describe the 'trace-map' representation and comparison of the DTI-derived structural fiber connection pattern. The "trace-map" method is shown in Figure 5.1A-D by projecting each beginning and ending point of each fiber from fiber bundles (Figure 5.1B) onto a uniform spherical surface. Then, we divide the surface into 48 equal areas and construct a histogram for each area, which are then represented as the feature vectors. A 48-dimensional histogram vector $tr = [d_1, d_2 \dots d_{48}]$, containing 48 density values, namely 'trace-map' (Zhu D et al., 2012a), is finally obtained as the structural profile of the landmark under consideration. By constructing trace-map, the fibers penetrating to the landmark can thus be represented as vectors with

dimension of 48, instead of 3D shapes. Through this way, structural connectivity patterns and similarities between landmarks can be quantitatively measured.

5.2.4 Functional Connectivity Descriptor "function trace-map"

In the previous HAFNI work (Lv et al., 2015a), hundreds of latent brain networks have been successfully identified and different brain functions are organized as their spatial overlaps and temporal interactions. Though these HAFNI derived networks are ideal to be treated as individual functional profiles, they are difficult to be compared across subjects. Inspired by the "structural trace-map" mentioned above, here, we proposed a new functional descriptor, "functional trace-map", based on HAFNI networks to measure the functional connectivity between seed vertex and all the other vertices in the brain. Moreover, "functional trace-map" can dramatically reduce the dimension of 3D functional connectivity maps into 1D feature vectors. At the same time, we can preserve the necessary spatial information for quantitatively measuring the functional connectivity. In the HAFNI project (Lv et al., 2015a), we demonstrated that in a specific functional network (e.g. task fMRI derived network), vertices in the activation regions are considered to have similar functional meaning and have stronger functional connection among each other. Thus, given 7 functional tasks (there are 2800 functional networks in total for each subject and those networks are illustrated in Appendix B Part I) (Lv et al., 2015a), they can be projected onto the cortical surface for each subject to explore a potential functional connectivity map for each vertex on the cortical surface.

Here are the details of how to generate a functional connectivity map: Each vertex is linked with some counters that store the number of the networks it is involved and are initialized as 0 at the beginning. For each vertex v_i on the cortical surface, it is treated as a seed voxel. All the 2800 networks are examined and those networks are selected in which the seed vertex v_i is

activated. For each selected network, we record all the activated vertices v_{active} (exclude v_i) and update the counters of all those v_{active} by adding 1. Thus a connectivity map can be constructed for the seed vertex v_i that contains the counters of all v_{active}. We named this map as a functional connectivity map f_i of the seed vertex v_i (as shown in the Figure 5.1F). More details about generating the functional connectivity map are provided in Appendix B Part II. Then, based on this functional connectivity map f_i , the seed vertex v_i is made as the center of a unit sphere. We connect v_i and all the vertices in v_{active} and project this direction to the uniform spherical surface as a unit vector. The projection dots represent the value of counters (Figure 5.1F). At last, we divide the uniform spherical surface into 144 equal areas and construct histogram of dots for each area in sequence, which are then represented as functional feature vectors. A 144-dimensional histogram vector $tr = [d_1, d_2 \dots d_{144}]$, containing 144 density values, namely "function trace-map", is finally obtained as the function connectivity of the seed vertex. By constructing the function trace-map vectors, seed vertex's functional connectivity map can be represented by 144 feature vectors instead of using around 100k dimension vectors, more details of the "functional trace-map" descriptor are provided in Appendix B Part II. Most importantly, this functional trace-map can efficiently preserve major spatial information of the seed vertex, more details and evaluations of the functional trace-map descriptor are provided in Appendix B Part III.

5.2.5 DBN Model of Joint Representation of Structural and Functional Profiles

Deep Belief Network (DBN) (Hinton 2009) is built up with a stack of probabilistic model called Restricted Boltzmann Machine (RBM) (Smolensky et al., 1986) as shown in the Figure 5.1I. In general, RBM is an energy-based model with the joint probability distribution that can learn probability distribution from input data. A typical RBM consists of two layers, that is, the

visible layer v and the hidden layer h. The visible layer is directly connected to the input data, and each of visible nodes accepts one dimension of the input. The number of hidden layer nodes is denoted by *k*, each of which represents a latent variable. The space of latent variables is spanned by the hidden nodes. The connection between these two layers is represented by the weight W, the size of which is *n* × *k*. RBM defines the probability by the energy of the system, E(v,h), such that:

$$p(v) = \sum_h p(v,h) = \sum_h \frac{1}{Z} \exp^{-E(v,h)} \tag{5-1}$$

where $Z = \sum_{v,h} exp^{-E(v,h)}$, is the partition function (Smolensky et al., 1986). To estimate normally distributed real data, *E(v,h)* is defined in Gaussian- Bernoulli RBM (GB-RBM) as:

$$E(v,h) = -\sum_{ij} \frac{1}{\sigma_i} v_i w_{ij} h_j - \sum_i \frac{(a_i - v_i)^2}{\sigma_i^2} - \sum_j b_j h_j \tag{5-2}$$

where w_{ij} is the weight between the visible variable v_i and the hidden variable h_j. a_i and b_j are the bias of visible and hidden variables. σ_i is the standard deviation of a quadratic function for each v_i centered on its bias a_i.

RBMs are trained by using the contrastive divergence (CD) learning procedure (Carreira-Perpinan, et al., 2005). Each RBM layer is trained by using the previous layer's hidden units (h) as input/visible units (v). Inputs are modeled by RBMs via latent factors expressed through the interaction between hidden and visible variables. Thus, DBNs can be trained greedily, one layer at a time, which leads to great hierarchical representation (Hu et al., 2018; Li et al., 2018). In details, the learning gradient is computed from feature of a single vertex, while the algorithm will go through the complete dataset with number of epochs (all subjects together); one procedure of going through the complete dataset is called an "epoch". For each data point presentation, each visible variable is assigned with the value of the corresponding vertex. Then, a truncated, iterative version of Gibbs sampling called contrastive divergence (CD) is applied to

the complete set of variables. This is done in an alternating sequence of hidden and visible variables, using the current values of the weights to calculate sampling probabilities of each layer. The difference between the values of the hidden and visible variables at the beginning and the end of the Gibbs chain is used to compute the learning gradients, which are then used to update the values of the weights before the next fMRI data point is presented. In addition, other penalty functions, such as L1 penalty on the weights or sparsity of simultaneously active hidden units can also be considered here.

In this work, for training dataset, the vertices coming from 10 subjects are collected and treated as a standard training dataset. For each vertex, 192 feature vectors (48 from structure and 144 from function) are obtained from both functional trace-map and structural trace-map. In total, around 1 million vertices are considered from 10 subjects as the input. The inputs can be represented as below:

$$I = [sbj1_1, sbj1_2 \dots sbj1_{n_1}, sbj2_1, sbj2_2 \dots sbj2_{n_2}, \dots \dots sbj10_{n_{10}}]' \quad (5\text{-}3)$$

Where n_i is the total number of vertices of *i*-th subject. Each element in the equation 5-3 represents a column vector with dimension of 192. The DBN model in this work has three hidden layers that have 100, 50 and 25 hidden nodes, respectively. The number of the nodes is decided by using the low-rank decomposition algorithms (Wen et al., 2012), the rank of the input is around 50. Therefore, we give this low rank more redundancy by multiply the rank by 2, then the nodes for the first layer is set to 100. Similar for the second and third layer. The major parameter settings are shown as below: base epsilon: 0.0001, initial momentum: 0.5, final_momentum: 0.9, momentum_change_steps: 3000, l1_decay: 0.1, activation: TANH, gibbs_steps: 1, training steps: 50000. Notably, the weight decay L1 plays an important role in our experiments, in that it controls the sparsity of the functional network. By applying the weight

decaying rate in each iteration, less vital connections are forced to be small and only the most important ones are preserved, yielding the weights, i.e., functional networks, to be sparse.

5.2.6 Common Network Analysis

As mentioned, the outputs from the DBN model are the weights of each hidden layer. Here, layer 1 is used as an example: the dimension of the inputs is $(n_1 + n_2 + \cdots + n_{10}) * 192$, where n_i is the total number of vertices of *i*-th subject. Because the number of nodes in layer 1 is 100, the dimension of the weights obtained will be $(n_1 + n_2 + \cdots + n_{10}) * 100$. In this way, we can extract the weights *w* for each subject by simply dividing the weights matrix into 10 parts, *w* is consisted of $[w_1, w_2, w_3 \ldots w_{10}]'$ and the dimension of w_i is n_i*100. In other words, w_i contains 100 brain networks for subject *i*, and each brain network can be easily visualized by simply assigning the values in w_i to the corresponding vertices. At last, 100 common brain networks can be achieved for each subject. Similar to the output of layer 2 and layer 3, 50 and 25 brain networks can be obtained for each subject as well.

After the brain networks have been observed and identified, it is needed to quantitatively measure their functional and structural consistency. Here, two methods are adopted: in order to evaluate the structural consistency, shape of fiber bundles that passing through those activation areas are compared by calculating the Pearson correlation between structural trace-map features; regarding the functional consistency, because the identified brain networks are under individual space, we need to perform the registration first: we register those brain networks (activation vertices) from individual space into the MNI standard space using FLIRT (Jenkinson et al., 2001). Then those activation vertices can be compared by simply calculating the ratio of overlap.

5.2.7 Hierarchical Model of Common Brain Networks

DBN is a hierarchical neural network that can learn probabilistic structure from the inputs. That is to say, different layers can represent information with different generalization level. In the proposed algorithm, DBN has 3 layers in this work, as suggested from existing studies such as Erhan et al., 2009 and Salakhutdinov et al., 2010, mentioning that three hidden layers are usually the basic model of the DBN. And then, the obtained brain networks from these 3 layers should follow a hierarchical structure. the relationship between brain networks derived from different layer is measured by directly computing their overlap. The networks in the higher-level should be more abstract and might have global activation area which tend to contain some specific networks from the lower-level. The ratio of overlaps is defined between lower-level derived brain networks and those from higher-level as L-overlap rate:

$$L = Overlap(A, B)/(A) \tag{5-4}$$

Here, network A represents the lower level networks and B stands for the higher-level networks. Through this way, for each higher-level brain network, most related lower-level brain networks can be identified. It is hypothesized that the hierarchical brain networks should possess both functional and structural hierarchical characteristics simultaneously.

5.2.8 Validation of the DBN Model

In this work, a validation experiment is designed by using extra data and one used subject data is kept to generate a new input. The reason to keep one used subject is that it will be convenient to do the comparison from two inputs at later steps. In general, it is needed to examine whether the same common brain networks can be achieved from different inputs. Next, commonly used Jaccard overlap (Lv et al., 2015a, Zhao et al., 2016) is adopted to discover the correspondent networks from different inputs based on the similarity of the brain networks. The

frequency of the common brain networks obtained from different inputs can be used to estimate the reproducibility of the proposed model.

5.2.9 Relationship between Common Brain Networks and HAFNI Maps.

The hierarchical architecture can be observed and identified from Section 5.2.7. However, one important issue is how to understand and interpret those hierarchical architectures. For example, what is the neuroscience meaning behind each layer and what's the relationship between different layers. In this work, we perform a comparison between hierarchical networks and HAFNI components identified in our previous work to illustrate the modular organization of how our brain works. In the HAFNI work, the individual HAFNI components include concurrent functional networks of both task-evoked and resting state related functional maps, which can be reproduced across individuals (Lv et al., 2015a). In addition, group-wise HAFNI components are also available and contained much more global information. Thus, they can be treated as functional templates which could be used to evaluate the similarity with the hierarchical brain networks.

Specifically, we compared the common brain networks from 3 layers with individual HAFNI components and groupwise HAFNI components by computing the overlap of the activation areas on the cortical surface. Thus, for each HAFNI component (from both individual and group-wise), we can identify most correlated common brain networks in each of 3 hierarchical layers. Lastly, we outline the relationship between hierarchical model and HAFNI components, and further illustrate the architecture of the brain module organization.

5.2.10 Explore the Functional Meaning of Common Brain Networks through Meta-analysis

We applied several algorithms to check the functional and structural consistency of those common brain networks obtained across different subjects. To further explore the functional

meaning of those networks, “meta-analysis” is adopted to analyze the functional roles of those obtained networks. “Sleuth” is a widely used toolbox from the BrainMap ((Laird et al., 2005; Fox et al., 2002; Fox et al., 2005)) that can search related publications/reports and screen their corresponding meta-data to plot their results as coordinates within standard Talairach space (also can be converted to MNI space). By searching from thousands of related function brain imaging studies, meta-analysis can perform the statistics of the reported functional meaning (behaviors) of ROIs we selected. In this work, the areas are selected with highest intensity in the common brain networks as the ROIs to do the meta-analysis and integrate the corresponding roles of those functional networks. After the functional meaning of those networks is obtained, the comparison across the subjects can be done to examine whether they have consistent functional roles and/or whether they have consistent anatomical locations. This is another validation approach to reveal the consistency of the networks we obtained from the DBN model. The details about how to use the sleuth software to search for papers of interest could be found on the website: http://www.brainmap.org/sleuth/.

5.3 Experimental Results

In this work, the model is developed upon deepnet package to train the DBN model. One GPU (NVIDIA Corporation GP102 GeForce GTX 1080 Ti) was used to speedy training the dataset. As mentioned in the method section, a 3-layer DBN model was constructed and the number of nodes from layer 1 to layer 3 were 100, 50, 25, respectively. The training process lasted for around 5 hours for each run of the inputs.

5.3.1 Common Brain Networks

As mentioned in method Section 5.2.6, the number of the hidden nodes controls the number of the obtained brain networks for each subject. The identified networks from the same node display great consistency across different subjects (Figure 5.2 – Figure 5.4). We obtained 100 networks from layer 1, 50 networks from layer 2 and 25 networks from layer3 for each subject. Note that the correspondence of networks is automatically obtained from the DBN model and we visualized all the networks based on the nodes in each layer and showed on the website:

Homepage: http://hafni.cs.uga.edu/multimodality_DBN/DBN.html

Layer1: http://hafni.cs.uga.edu/multimodality_DBN/layer1.html

Layer2: http://hafni.cs.uga.edu/multimodality_DBN/layer2.html

Layer3: http://hafni.cs.uga.edu/multimodality_DBN/layer3.html

Here, eight randomly selected brain networks of ten subjects from layer 1 to layer 3 are showed. The color bar in each figure is set from 0.1 to 0.6 (blue to red). It can be seen that for each common brain network, it shows significant consistency across different subjects as we expected. Note that our experiment was designed and processed within the individual space, which means no registration is needed. Functional consistency has been evaluated for all identified common brain networks from three layers (method part 5.2.6). Quantitatively, the average functional consistency from layer 1 to layer 3 are 0.61, 0.68 and 0.88, respectively, which are quite high given the variability of brain functions.

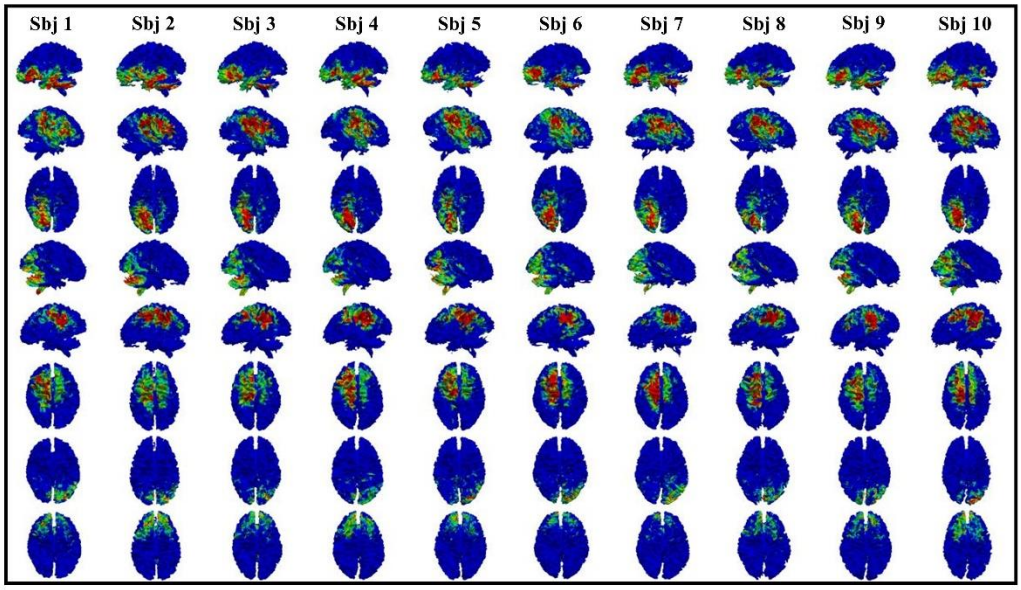

Figure 5.2. Eight examples of common brain networks obtained from DBN model layer 1. Each row represents a corresponding network from 10 subjects. The average functional consistency for all the common networks in layer 1 is 0.61.

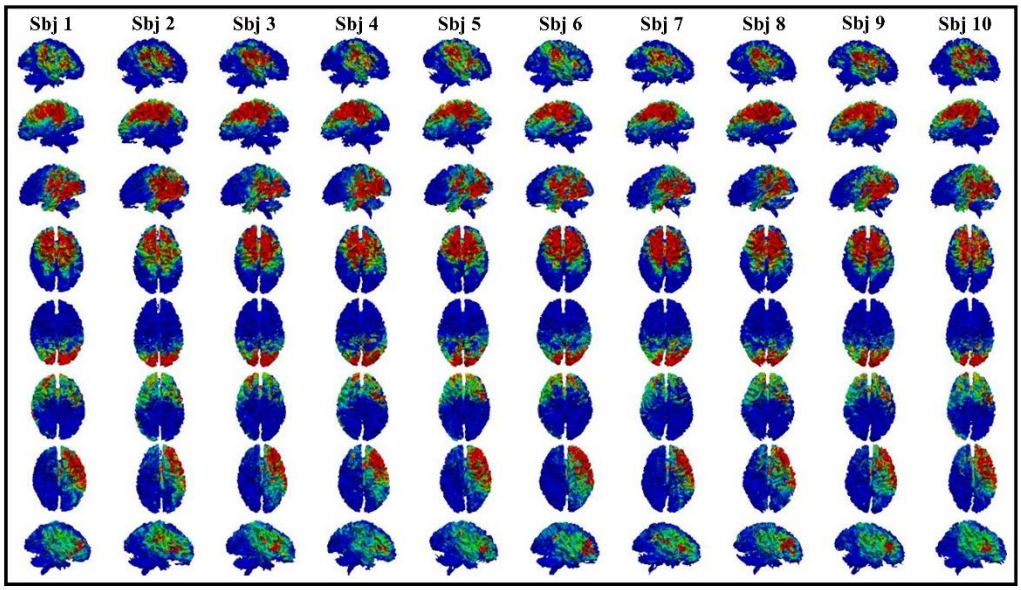

Figure 5.3. Eight examples of common brain networks obtained from DBN model layer 2. The average functional consistency for all the common networks in layer 2 is 0.68.

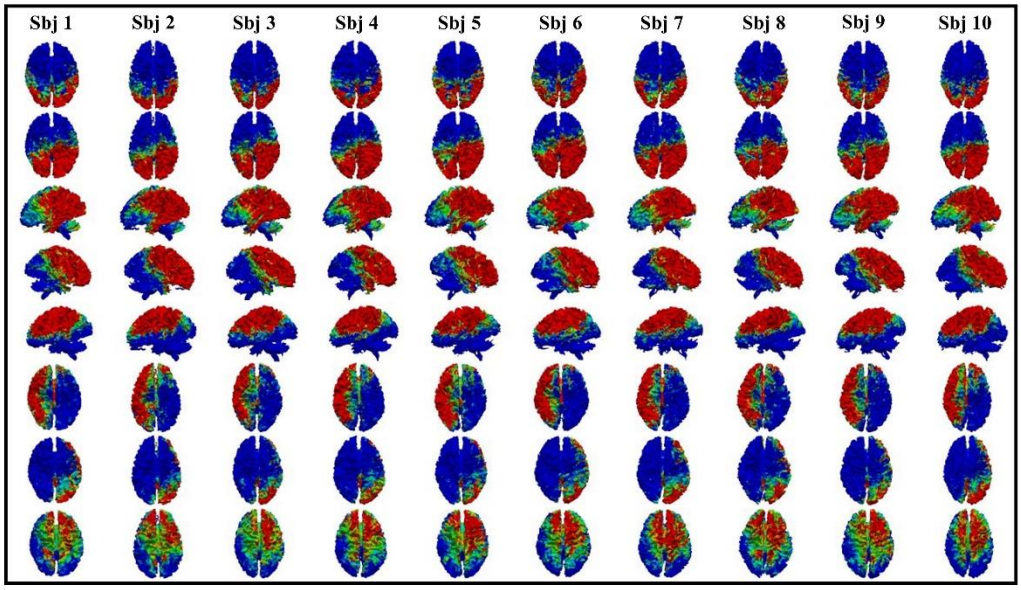

Figure 5.4. Eight examples of common brain networks obtained from DBN model layer 3. The average functional consistency for all the common networks in layer 3 is 0.88.

As indicated by numerous studies (e.g. Honey et al., 2009; Koch et al., 2010), there is close relationship between brain function and structure. For example, Park et al., 2013 mentioned that network analysis suggests that hierarchical modular brain networks are particularly suited to facilitate local (segregated) neuronal operations and the global integration of segregated functions and functional connectivity is highly constrained by structural connectivity. Similarly, our work had similar findings and proved that functional networks had close relationship with the structural connections. From the Figure 5.5, it can be seen that the shape of the fiber bundles is very consistent. To quantitatively represent their similarity, we used structure trace-map method, mentioned in the Section 5.2.3, the average similarity among 4 networks are 0.45, 0.54, 0.42 and 0.57 respectively. The functional consistency is also listed in the Figure 5.5, for example, 0.703 from the subject 1 in the first network represents the average consistency when comparing the subject 1 with the other 9 subjects. To our best knowledge, those networks have

great functional and structural consistency at the same time across different subjects. This is the first contribution of this work.

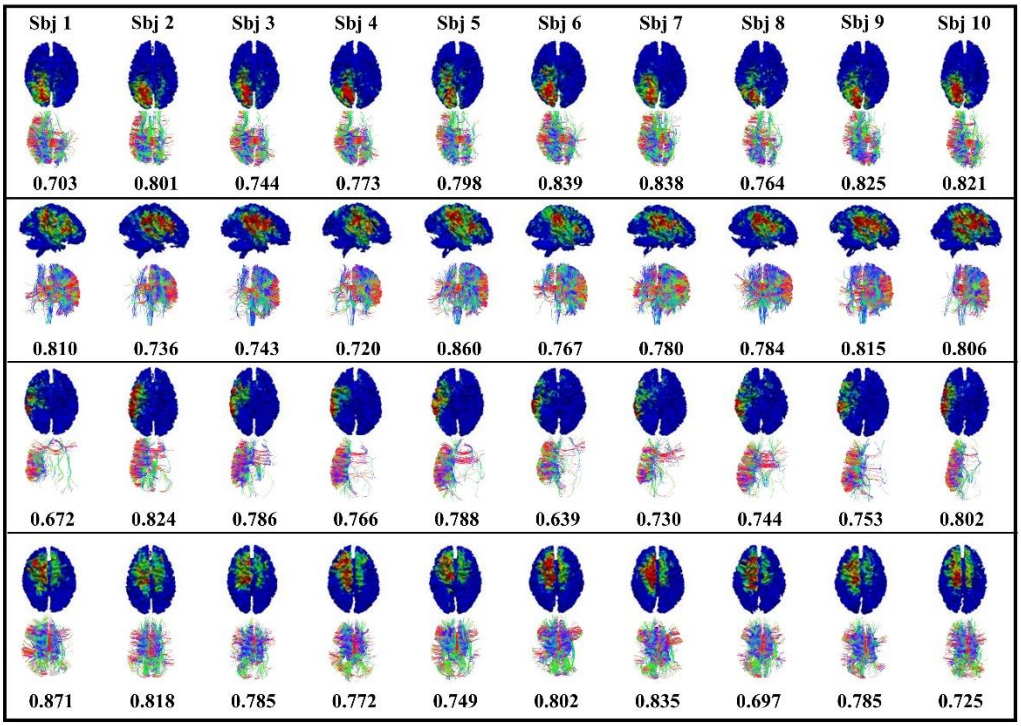

Figure 5.5. Examples of presenting functional and structural consistency for common brain networks. Shape of the fiber bundles is used to present the structural consistency; network overlap rates are used to present the functional consistency.

5.3.2 Hierarchical Brain Networks

Interestingly, hierarchical representations are observed from the common brain networks in both structural and functional perspectives. By studying those hierarchical representations, it is confirmed that the consistency from 3 layers keeps climbs from lower layer to the higher layer. In addition, in the hierarchical model, the higher layer represents more global information and this global information will have more consistency across the subjects. As seen from Figure 5.6, DBN has three layers and corresponding common brain networks are obtained from each layer. In details, following the steps in Section 5.2.7, for the common brain networks from layer 3, a set

of related brain networks from layer 2 are picked up, furthermore, some related networks from layer 1 are also identified. Then those networks are represented in a tree model as shown in Figure 5.6. In the meantime, fiber connections of those functional patterns are also provided. In order to evaluate the performance of how higher DBN-layer networks could represent lower DBN-layer networks, L-ratio from equation 5-4 is used here. For example, in the network 1 of Figure 5.6, the network A covers 70% of the network B and 100% of the network C, the network B covers 65% of D; in the network 2, L covers 80% of M, 80% of N and 100% of O. M covers 72% of Q. In general, all the hierarchical networks obtained from 3-layer DBN model have a relatively high L-rate which reaches to 65% as a lower band. Thus, the networks from 3 DBN layers can successfully represent the hierarchical characteristics. An important conclusion is that the higher-layer can represent more global information and this global information will have more consistency across the subjects, on the contrary, lower layers will represent more local information and have less consistency across the subjects. This is another contribution of this work. All the hierarchical representation results are shown on the website:

Hierarchical representation between layer 1 and layer 2:

http://hafni.cs.uga.edu/multimodality_DBN/hierarchical.html

Hierarchical representation between layer 2 and layer 3:

http://hafni.cs.uga.edu/multimodality_DBN/hierarchical2.html

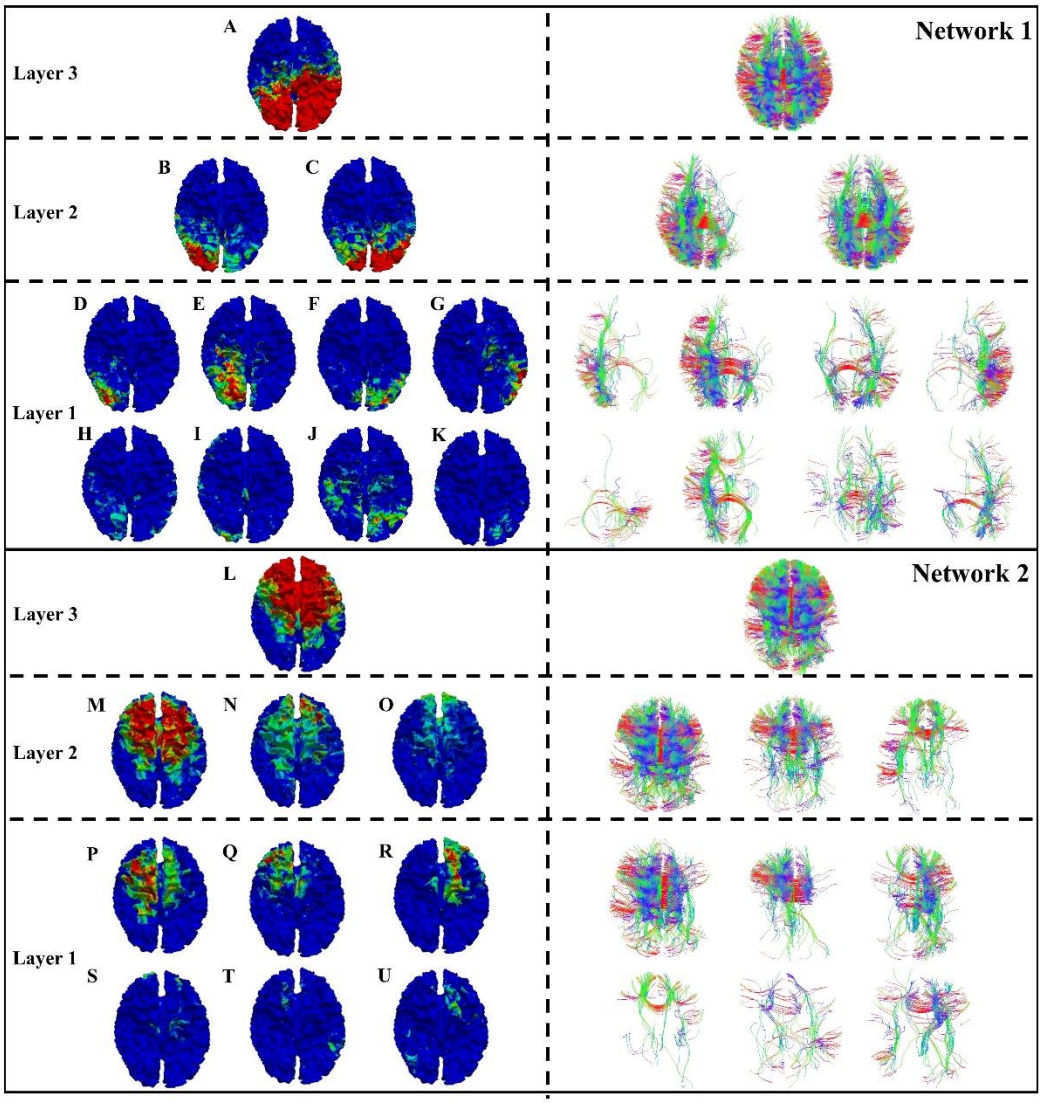

Figure 5.6. Two examples of hierarchical representation for specific common brain networks in top layer (layer 3). Functional and structural profiles are corresponding from left to right. A-U are networks from corresponding layers.

5.3.3 Validation Experiments

One important issue is if the consistent networks obtained using one dataset can be reproduced on another. To address this concern, a validation experiment is added in this section. We adopted extra data (10 subjects) to be the test-bed. Parameters are exactly the same with the previous experiment, 3 layers are also designed, the number of nodes from layer 1 to layer 3 are

still 100, 50, 25. After the proposed method is employed on the new data, common networks are successfully obtained for each layer. Same statistical analysis is done to examine the functional and structural consistency within the validation experiment. Similar results are obtained and their correspondence of networks is automatically constructed from the DBN model.

In the layer 1, 48 out of 100 networks are consistent across the experiments and they have 0.25-0.5 Jaccard overlap rate; in the layer 2, 37 out of 50 networks have about 0.25-0.66 Jaccard overlap rate; in the layer 3, 25 out of 25 networks have about 0.25-0.81 Jaccard overlap rate. Thus, it is confirmed that those consistent common networks can be reproduced from validation experiment. It is worth noting that, to measure the correspondence among different experiments, one subject will be used as the bridge, so this subject is retained in the validation dataset, in this way, common networks from different experiments can be compared directly on this common subject (sbj1 in this work). To best keep the differences between two groups, only one common subject is accepted. 8 example common networks are provided in the Figure 5.7. From the Figure 5.7, original experiment results and the validation experiment results are presented from left to right.

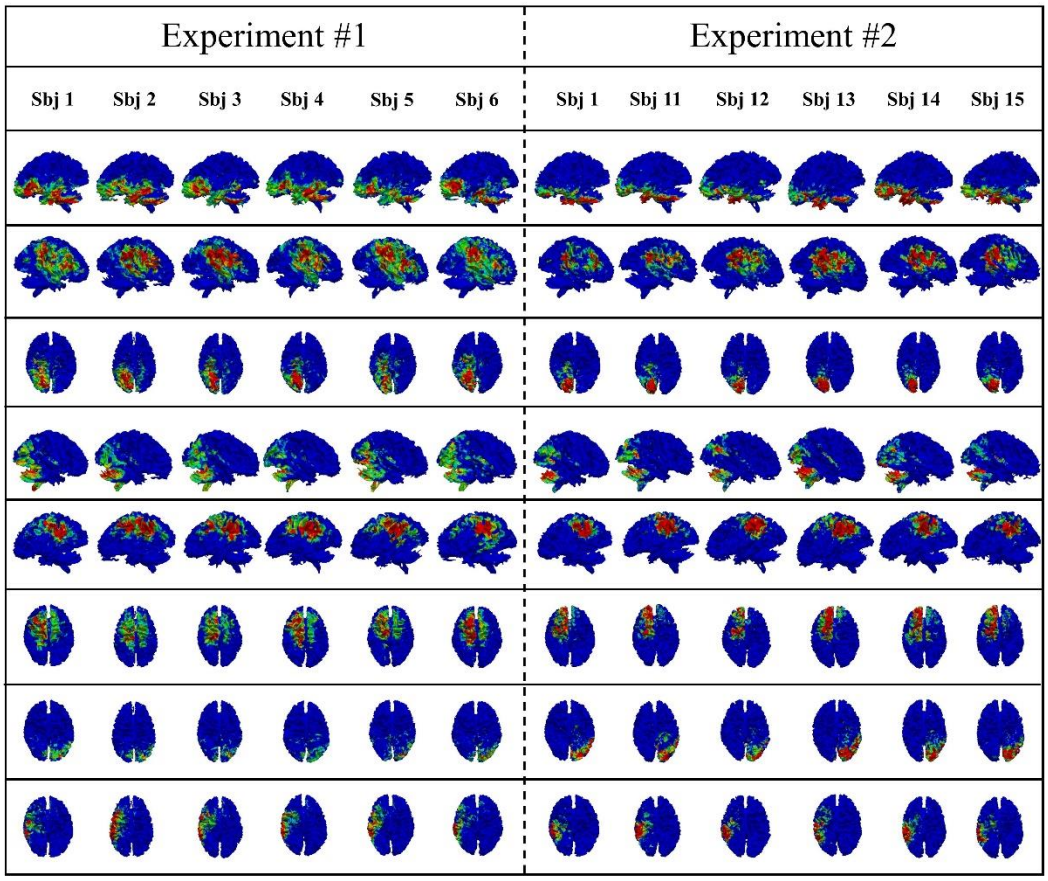

Figure 5.7. Validation of proposed algorithm by comparing the corresponding common brain networks obtained in layer 1 from two experiments. The Jaccard overlap rate of those 8 networks is 0.57, 0.53, 0.50, 0.49, 0.45, 0.41, 0.37 and 0.36, respectively.

5.3.4 Explore the Hierarchical Model via HAFNI Maps

HAFNI maps include a large number of reproducible and robust functional networks, they are simultaneously distributed in distant neuroanatomic areas while substantially spatially overlapping with each other, thus forming an initial collection of holistic atlases of functional networks and interactions. It is very interesting that common networks obtained from the proposed algorithms are also reproducible and robust across the subjects. The difference is that HAFNI maps are obtained from functional MRI only, however common networks obtained from

this work are correlated with both function and structure. Thus, the relationship between HAFNI and our DBN common networks is of interest.

As mentioned in Section 5.2.9, common networks from 3 layers are compared with the individual HAFNI components and group-wise HAFNI components by comparing the overlap of the activation area on the cortical surface. By checking the relationship between each layer from the DBN model and HAFNI components, it is concluded that in the DBN model, networks from layer 1 are more relevant to the HAFNI individual components and networks from layer 2 are much more correlated with the HAFNI group-wise components. One example is shown in the Figure 5.8. In details, DBN networks from layer 1 are still quite localize and related to specific cortical regions. When the layer comes to the second, the activation area is enlarged by presenting more abstract information from the first layer's DBN maps, then those second layer DBN maps are much like the HAFNI group-wise average maps, which are the higher-level representations based on HAFNI individual maps. So, the concept that higher layer brings much more global information is also suitable for the brain modular organization. Similar to the third DBN layer for the visual function in Figure 5.8, much more abstract representation is observed based on the second level, which almost covers the occipital lobe and parts of the parietal lobe.

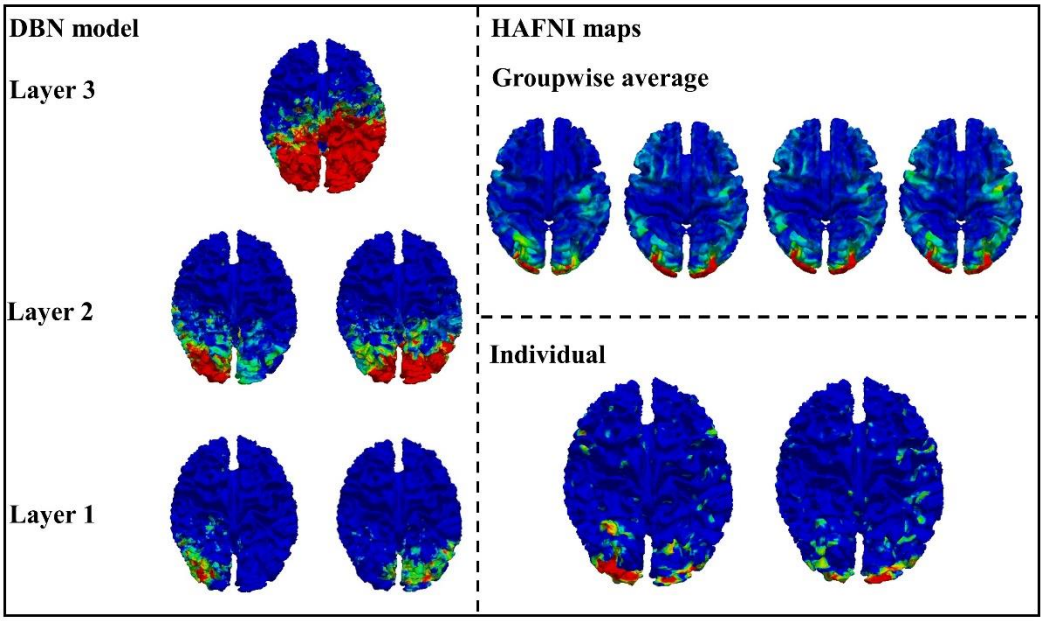

Figure 5.8. Comparison of DBN maps and HAFNI maps in visual function.

5.3.5 Explore the Function Meaning of Common Brain Networks via Meta-analysis

To further explore the functional roles of the identified common brain networks, we performed meta-analysis which is widely adopted in brain mapping field. In this work, corresponding common brain networks are examined via meta-analysis, three examples with their functional behaviors and anatomical locations are reported in Figure 5.9. Using the first network in the Figure 5.9 as an example, it is located on the Parietal lobe and precuneus and the related functional roles are: cognition, language, perception and emotion. In addition, these functional roles are very consistent across the subjects. Results for other common networks are also obtained and they also have consistent functional roles. Besides comparison with the HAFNI components in result part D, this is another important evidence that the common brain networks obtained from DBN model not only possess functional and structural consistency but also have consistent neuroscience meanings.

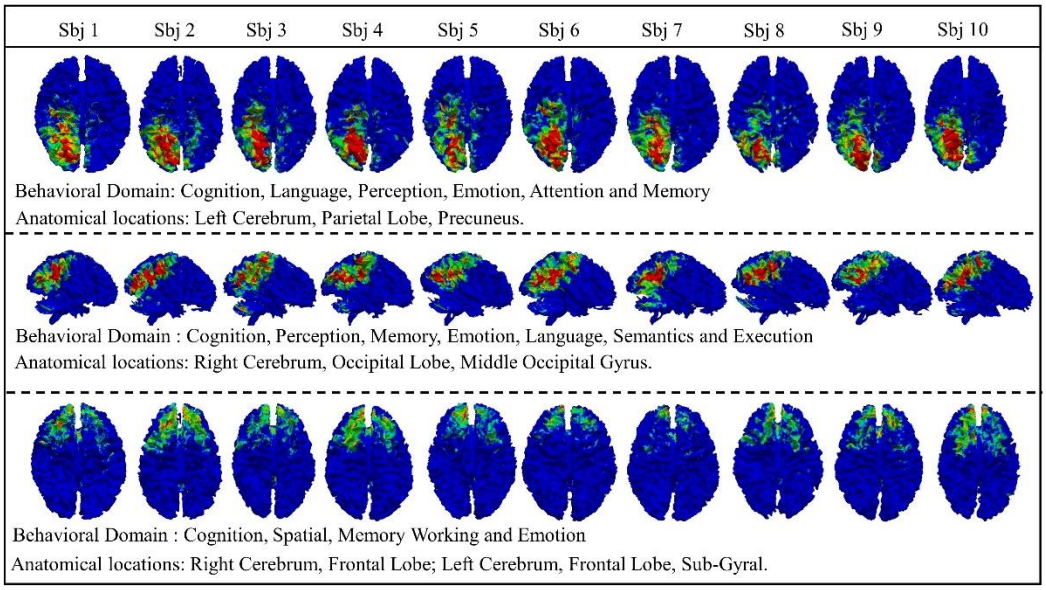

Figure 5.9. Meta-analysis results of three typical functional networks.

5.4 Discussion and Conclusion

In this chapter, we proposed a novel DBN model combining structural and functional connectivity profiles together to jointly represent the hierarchical common brain networks across different individuals. Three hierarchical layers are designed and represented across the 10 subjects with 100, 50 and 25 networks, respectively. Those common brain networks are further confirmed though the analysis including DBN analysis, hierarchical analysis and validation experiments. Then, by comparing the results between HAFNI components and the DBN results, we found a potential interpretation of the identified hierarchical organization. That is, lower level networks are more related to individual functional characteristics and higher-level networks tend to reflect global functional organization at population level. To better understand the functional meaning and anatomical information of those networks, we performed the meta-analysis using Sleuth software from BrainMap to explore the functional and anatomical explanations of all

common brain networks derived. The results suggest that corresponding common networks across different subjects tend to have consistent functional meanings and similar anatomical locations.

The major contributions and advantages of our proposed method are two-fold: First, our DBN model can effectively and successfully identify the hierarchical brain networks. Second, our proposed method considers both functional and structural profiles to build a fusion model for single vertex. For the hierarchical representation, there is already numerous evidence that brain networks have a hierarchical organization. However, we are lacking of effective method and computational model to discover this at the voxel level. Effective method could help to dig out the architecture of the brain image data correctly. Great computing engine has ability to deal with the tremendous data dimension at group level, more data will bring more information to build the architecture much more accurate and consistent across the subjects. DBN model is the right method to be used. One thing, DBN is highly recognized for its unsupervised learning of hierarchical representations, architectures can be revealed by DBN automatically. The other thing, DBN is a classical deep artificial neural networks which can be easily applied onto GPU. With the help of hardware GPU, the computing performance goes extremely high and way better than the traditional computing algorithms. For the fusion model, multimodal information will be complementary to each other, thus, features generated will have both functional and structural characteristics. Then the networks obtained should have both functional and structural consistency which are confirmed later. This is a new insight to do the fusion of the functional and structural profiles and explore the joint representation with the help of the powerful deep learning algorithms.

Despite its advantages in latent feature learning and the outperformance in DBN model demonstrated in this study, our model still has some places to be improved in the future. First, currently, our DBN model is still rather simple and straightforward. For the architecture, we fix the number of the layers to 3 due to the prior knowledge. And we set the hidden nodes by consulting from the low-rank of the inputs data. In the future, more knowledge will be discussed from neuroscience and neuroimaging field to decide the architecture of the DBN model. Second, in this work, the connectivity features for each vertex is fused by both functional and structural connectivity and then they are used to train DBN model, however, another scenario is that functional and structural connectivity can be trained separately using DBN model, and then at some time point, those features are combined together and connected with another DBN model to train the joint representation profiles, this could be another improvement for the DBN model.

Acknowledgements

In this chapter, we trained RBMs using the DeepNet package (https://github.com/nitishsrivastava/deepnet). This research was supported by the National Institutes of Health (DA-033393, AG-042599) and by the National Science Foundation (NSF CAREER Award IIS-1149260, CBET-1302089, BCS-1439051 and DBI-1564736).

CHAPTER 6

DISCUSSION AND CONCLUSION

This dissertation systematically studied the identification of common architectures of the brain through our proposed novel frameworks, those common architectures are obtained and reflected both brain structural and functional organizations across individuals and populations at different scales.

The major contributions of this dissertation are two-fold:

First, 4 novel computational frameworks are designed to identify the common architecture of the brain from three difference scales. At the landmark scale, inspired from DICCCOL and HAFNI, Chapter 2 proposes a novel computational framework to jointly represent connectome-scale functional (HAFNI Peaks) and structural connections (DICCCOL trace-map) for the identification of a set of consistent and common cortical landmarks with both reasonably accurate structural and functional correspondences across different macaque brains based on multimodal DTI and fMRI data. Then, Chapter 3 proposes an effective computational framework, which is designed to optimize the framework in the Chapter 2. By adding the groupwise registration step, this effective computational framework works better on the big dataset. At the local region scale, Chapter 4 proposes a novel framework to combine functional networks and structural connections together to obtain the most active fiber connection patterns of the brain. The novelty of this framework is to describe the functional characteristics for each individual fiber. Then, main skeleton of structural connections and their local fiber pattern are observed and identified. At the network scale, inspired from deep learning algorithms, Chapter 5

proposes a novel computational framework to explore both functional and structural connectivity on voxel level and thus to learn hierarchical latent features and associated representations of the whole brain via Deep Belief Network (DBN) model. This framework possesses strong learning power and surpassing power in learning hierarchical latent features and associated representations.

Second, experimental results have demonstrated that common architecture of brains can be successfully identified through proposed novel frameworks at landmark scale (Chapter 2 & 3), local region scale (Chapter 4) and the network scale (Chapter 5), respectively. In details, at the landmark scale, 100 consistent and common cortical landmarks are successfully identified via our proposed framework, each of which has reasonably accurate anatomical, structural fiber connection pattern, and functional correspondences across different macaque brains (Chapter 2), besides, 55 structurally and functionally common cortical landmarks can be successfully identified across different human brains (Chapter 3); at the local region scale, we identified main skeleton of whole-brain fiber connections and their eleven local common fiber patterns that are functionally and structurally consistent across individual brains (Chapter 4); at the network scale, with the proposed DBN model, three hierarchical layers of hundreds of common and consistent brain networks across individual brains are successfully constructed through learning a large dimension of representative features derived from fMRI/DTI data (Chapter 5). All of those common cortical landmarks, major fiber skeletons and common brain networks play an important role for us to understand the brain architectures fundamentally. Those common architectures will revolutionize our fundamental understanding of the structure and function of the brain and their relationships, and eventually shed novel insights into how to treat, cure, and prevent many devastating brain disorders.

This research topic can be further investigated in the future from two perspectives. First, more image modalities and information can be involved in the fusion model, currently, the focus is on the fMRI and DTI image data, however more useful data could be considered and adopted, for example, genetic data will be a good candidate to be investigated into the fusion model, cortical folding pattern is another interesting structural information which could be added into the fusion model. Second, in the future, common architecture could be used to distinguish the differences between healthy and disease subjects, in other words, common architecture could be treated as the biomarker, moreover, better understanding of the common architecture will shed novel insights into how to treat, cure, and prevent many devastating brain disorders.

REFERENCES

Anderson ML, Kinnison J and Pessoa L. 2013. Describing functional diversity of brain regions and brain networks. NeuroImage.73:50-58.

Abolghasemi V, Ferdowsi S, Sanei S. 2015. Fast and incoherent dictionary learning algorithms with application to fMRI. Signal, Image and Video Processing. 9(1): 147-158.

Armstrong Este, et al. 1991. "Cortical folding, the lunate sulcus and the evolution of the human brain." Journal of Human Evolution. 20.4: 341-348.

Barch D M, Burgess G C, Harms M P, et al. 2013. Function in the human connectome: task-fMRI and individual differences in behavior. Neuroimage. 80: 169-189.

Baaré William FC, et al. 2001. "Quantitative genetic modeling of variation in human brain morphology." Cerebral Cortex. 11.9: 816-824.

Baylis GC, Rolls ET, Leonard CM. 1987. Functional subdivisions of the temporal lobe neocortex. The Journal of Neuroscience. 7(2): 330-342.

Beckmann CF, DeLuca M, Devlin JT, Smith SM. 2005. Investigations into resting-state connectivity using independent component analysis. Philosophical Transactions of the Royal Society B: Biological Sciences. May 29;360(1457):1001-13.

Belliveau JW, Kennedy DN, McKinstry RC, Buchbinder BR, Weisskoff R, Cohen MS, Vevea JM, Brady TJ, Rosen BR. 1991. Functional mapping of the human visual cortex by magnetic resonance imaging. Science. Nov 1;254(5032):716-9.

Bengio, Y., Courville, A.C., Vincent, P. 2012. Unsupervised feature learning and deep learning: A review and new perspectives. CoRR, abs/1206.5538.

Brett M, Johnsrude I S, Owen A M. 2002. The problem of functional localization in the human brain. Nature reviews neuroscience. 3(3): 243-249.

Brosch T, Yoo Y, Li DK, Traboulsee A, Tam R. 2014. Modeling the variability in brain morphology and lesion distribution in multiple sclerosis by deep learning. InInternational Conference on Medical Image Computing and Computer-Assisted Intervention. Sep 14 (pp. 462-469). Springer, Cham.

Calhoun VD, Adali T, Pearlson GD, Pekar JJ. 2001. A method for making group inferences from functional MRI data using independent component analysis. Human brain mapping. Nov 1;14(3):140-51.

Calhoun VD, Liu J, Adalı T. 2009. A review of group ICA for fMRI data and ICA for joint inference of imaging, genetic, and ERP data. Neuroimage. Mar 1;45(1):S163-72.

Calhoun VD, Adali T. 2009. Feature-based fusion of medical imaging data. IEEE Transactions on Information Technology in Biomedicine. Sep;13(5):711-20.

Calabrese E, Badea A, Coe CL, Lubach GR, Shi Y, Styner MA, Johnson GA. 2015. A diffusion tensor MRI atlas of the postmortem rhesus macaque brain. NeuroImage. 117: 408-416.

Carreira-Perpinan MA, Hinton GE. 2005. On contrastive divergence learning. In Aistats, Jan 6 (Vol. 10, pp. 33-40).

Chen H, Zhang T, Guo L, Li K, Yu X, Li L, et al. 2012. Coevolution of gyral folding and structural connection patterns in primate brains. Cerebral Cortex. 23(5), 1208-1217

Chen H, Zhang T, Liu T. 2013. Identifying Group-Wise Consistent White Matter Landmarks via Novel Fiber Shape Descriptor. Medical Image Computing and Computer-Assisted Intervention–MICCAI 2013. Springer Berlin Heidelberg. 66-73.

Chen X W, Lin X. 2014. Big data deep learning: challenges and perspectives. IEEE access, 2: 514-525.

Chen, H., Li, K., Zhu, D., Jiang, X., Yuan, Y., Lv, P., ... & Liu, T. (2013). Inferring group-wise consistent multimodal brain networks via multi-view spectral clustering. IEEE Transactions on Medical Imaging. 32(9), 1576-1586.

Duffau H. 2015. Stimulation mapping of white matter tracts to study brain functional connectivity. Nature Reviews Neurology. 11(5): 255.

Eickhoff S B, Laird A R, Grefkes C, Wang L E, Zilles K, Fox P T. 2009. Coordinate-based activation likelihood estimation meta-analysis of neuroimaging data: A random-effects approach based on empirical estimates of spatial uncertainty. Hum Brain Mapp. 30, 2907-2926.

Erhan D, Bengio Y, Courville A, et al. 2009. Visualizing higher-layer features of a deep network. University of Montreal. 1341(3): 1.

Fischl B, Salat D H, Busa E, et al. 2002. Whole brain segmentation: automated labeling of neuroanatomical structures in the human brain. Neuron. 33(3): 341-355.

Felleman D J, Van Essen D C. 1991. Distributed hierarchical processing in the primate cerebral cortex. Cerebral cortex. 1(1): 1-47.

Ferry AT, Öngür D, An X, Price JL. 2000. Prefrontal cortical projections to the striatum in macaque monkeys: evidence for an organization related to prefrontal networks. Journal of Comparative Neurology. 425(3): 447-470.

Finn E S, Shen X, Scheinost D, et al. 2015. Functional connectome fingerprinting: identifying individuals using patterns of brain connectivity. Nature neuroscience. 18(11): 1664.

Fox P T, Lancaster J L. 2002. Mapping context and content: the BrainMap model. Nature Reviews Neuroscience. 3(4): 319-321.

Fox P T, Laird A R, Fox S P, et al. 2005. BrainMap taxonomy of experimental design: description and evaluation. Human brain mapping. 25(1): 185-198.

Galletti C, Fattori P, Gamberini M, Kutz DF. 1999. The cortical visual area V6: brain location and visual topography. European Journal of Neuroscience. 11(11): 3922-3936.

Goodfellow I J, Pougetabadie J, Mirza M, Xu B, Warde-Farley D, Ozair S, Bengio Y. 2014. Generative adversarial nets. In Advances in neural information processing systems. 3:2672-2680.

Gorski KM, Hivon E, Banday AJ, Wandelt BD, Hansen FK, Reinecke M, Bartelmann M. 2005. HEALPix: a framework for high-resolution discretization and fast analysis of data distributed on the sphere. The Astrophysical Journal. 622(2): 759.

Graves A, Mohamed A, Hinton G. 2013. Speech recognition with deep recurrent neural networks. In Ieee international conference on Acoustics, speech and signal processing. p. 6645-6649.

Greff K, Srivastava RK, Schmidhuber J. 2016. Highway and residual networks learn unrolled iterative estimation. arXiv preprint arXiv:1612.07771.

Hagmann P, Cammoun L, Gigandet X, Meuli R, Honey CJ, Wedeen VJ, Sporns O. 2008. Mapping the structural core of human cerebral cortex. PLoS biology. Jul 1;6(7):e159.

Hagmann P, Thiran JP, Jonasson L, Vandergheynst P, Clarke S, Maeder P, Meuli R. 2003. DTI mapping of human brain connectivity: statistical fibre tracking and virtual dissection. Neuroimage. Jul 1;19(3):545-54.

He, B., Coleman, T., Genin, G. M., Glover, G., Hu, X., Johnson, N., ... & Ye, K. 2013. Grand challenges in mapping the human brain: NSF workshop report. IEEE Transactions on Biomedical Engineering. 60(11), 2983-2992.

Huang H, Hu X, Zhao Y, Makkie M, Dong Q, Zhao S, Guo L, Liu T. 2017. Modeling Task fMRI Data via Deep Convolutional Autoencoder. IEEE transactions on medical imaging. Jun 15.

He, K., Zhang, X., Ren, S., Sun, J. 2016. Deep residual learning for image recognition. In IEEE conference on computer vision and pattern recognition. p. 770-778.

He, K., Gkioxari, G., Dollár, P., Girshick, R. 2017. Mask r-cnn. arXiv preprint arXiv:1703.06870.

Hinton GE. 2009. Deep belief networks. Scholarpedia. May 31;4(5):5947.

Hinton, GE 2002. Training products of experts by minimizing contrastive divergence. Neural computation. 14:1771-1800.

Hinton, GE, Osindero, S., Teh, Y.-W. 2006. A fast learning algorithm for deep belief nets. Neural computation. 18:1527-1554.

Hinton, GE, Salakhutdinov, R.R. 2006. Reducing the dimensionality of data with neural networks. Science. 313:504-507.

Honey CJ, Sporns O, Cammoun L, Gigandet X, Thiran J P, Meuli R, & Hagmann P. 2009. Predicting human resting-state functional connectivity from structural connectivity. PNAS. 106(6), 2035-2040.

Hu X, Huang H, Peng B, et al. 2018. Latent source mining in FMRI via restricted Boltzmann machine. Human brain mapping.

Howell BR, McCormack KM, Grand AP, Sawyer NT, Zhang X, Maestripieri D, Hu X, Sanchez M M. 2013. Brain white matter microstructure alterations in adolescent rhesus monkeys exposed to early life stress: associations with high cortisol during infancy. Biol Mood Anxiety Disord. 3(1):21.

Howell BR., McMurray MS, Guzman DB, Nair G, Shi Y, McCormack KM, Hu X, Styner MA, Sanchez MM. 2016. Maternal buffering beyond glucocorticoids: impact of early life stress on corticolimbic circuits that control infant responses to novelty. Social neuroscience. 1-15.

Jiang X, Zhu D, Li K, Zhang T, Wang L, Shen D, Guo L, Liu T. 2014a. Predictive Models of Resting State Networks for Assessment of Altered Functional Connectivity in Mild Cognitive Impairment. Brain Imaging and Behavior. 8(4):542-57.

Jiang X, Zhang X, Zhu D. 2014b. Intrinsic Functional Component Analysis via Sparse Representation on Alzheimer's Disease Neuroimaging Initiative Database. Brain connectivity. 4(8): 575-86.

Jiang X, Li X, Lv J, Zhang T, Zhang S, Guo L, Liu T. 2015a. Sparse representation of HCP grayordinate data reveals novel functional architecture of cerebral cortex. Human brain mapping. 36(12): 5301-5319.

Jiang X, Zhang T, Zhu D, Li K, Chen H, Lv J, Hu X, Han J, Shen D, Guo L, Liu, T. 2015b. Anatomy-Guided Dense Individualized and Common Connectivity-Based Cortical Landmarks (A-DICCCOL). Biomedical Engineering, IEEE Transactions on. 62(4): 1108-1119.

Jiang X, Zhang T, Zhao Q, Lu J, Guo L, Liu T. 2015c. Fiber Connection Pattern-guided Structured Sparse Representation of Whole-brain FMRI Signals for Functional Network Inference. Medical Image Computing and Computer-Assisted Intervention. 9349: 133-141.

Khachaturian M H. 2010. A 4-channel 3 Tesla phased array receive coil for awake rhesus monkey fMRI and diffusion MRI experiments. Journal of biomedical science and engineering. 3(11): 1085.

Jbabdi S, Woolrich M W, Behrens T E J. 2009. Multiple-subjects connectivity-based parcellation using hierarchical Dirichlet process mixture models. NeuroImage. 44(2): 373-384.

Jenkinson M, Smith S. 2001. A global optimization method for robust affine registration of brain images. Medical image analysis. Jun 1;5(2):143-56.

Johansen-Berg H, Behrens T E J, Robson M D, et al. 2004. Changes in connectivity profiles define functionally distinct regions in human medial frontal cortex. Proceedings of the National Academy of Sciences of the United States of America. 101(36): 13335-13340.

Koch K, Wagner G, Dahnke R, Schachtzabel C, Güllmar D, Reichenbach J R, & Schlösser R G M. 2010. Structure-function relationships in the context of reinforcement-related learning: a combined diffusion tensor imaging–functional magnetic resonance imaging study. Neuroscience. 168(1), 190-199.

Kolster H, Mandeville JB, Arsenault JT, Ekstrom LB, Wald LL, Vanduffel W. 2009. Visual field map clusters in macaque extrastriate visual cortex. The Journal of Neuroscience. 29(21): 7031-7039.

Laird A R, Lancaster J J, Fox P T. 2005. Brainmap. Neuroinformatics. 3(1): 65-77.

Le Bihan D, Breton E. 1985. Imagerie de diffusion in-vivo par résonance magnétique nucléaire. Comptes-Rendus de l'Académie des Sciences. Dec;93(5):27-34.

Lee L, Harrison LM, Mechelli A. 2003. A report of the functional connectivity workshop, Dusseldorf 2002. Neuroimage. 19(2): 457-465.

Lee H, Grosse R, Ranganath R, Ng AY. 2009. Convolutional deep belief networks for scalable unsupervised learning of hierarchical representations. In Proceedings of the 26th annual international conference on machine learning. Jun 14 (pp. 609-616). ACM.

LeCun Y, Bengio Y, Hinton G. 2015. Deep learning. Nature. 521(7553): 436-444.

Li L, Hu X, Huang H, He C, Wang L, Han J, Guo L, Liu T. 2018. Latent Source Mining of fMRI Data via Deep Belief Network. ISBI.

Li C, Zhang X, Komery A, Li Y, Novembre FJ, Herndon JG. 2011. Longitudinal diffusion tensor imaging and perfusion MRI investigation in a macaque model of neuro-AIDS: a preliminary study. Neuroimage. 58(1): 286-292.

Li K, Guo L, Faracoc C, Zhu D, Chen H, Yuan Y, Lv J, Deng F, Jiang X, Zhang T, Hu X, Zhang D, Miller S, Liu T. 2012. Visual analytics of brain networks. NeuroImage. 61(1): 82-97.

Li K, Guo L, Faraco C, et al. 2010. Individualized ROI optimization via maximization of group-wise consistency of structural and functional profiles. Advances in Neural Information Processing Systems. 1369-1377.

Li K, Zhu D, Guo L, Li Z, Lynch ME, Coles C, Hu X, Liu T. 2013. Connectomics signatures of prenatal cocaine exposure affected adolescent brains. Human brain mapping. 34(10): 2494-2510.

Liu T. 2011. A few thoughts on brain ROIs. Brain imaging and behavior. 5(3): 189-202.

Li X, Chen H, Zhang T, Yu, X., Jiang X, Li K., Li K, Razavi MJ, Wang X, Hu X, Han J, Guo L, Hu X, Liu T. 2016. Commonly preserved and species-specific gyral folding patterns across primate brains. Brain Structure and Function. 1-15.

Li G, Guo L, Nie J, et al. 2009. Automatic cortical sulcal parcellation based on surface principal direction flow field tracking. NeuroImage, 46(4): 923-937.

Logothetis NK. 2008. What we can do and what we cannot do with fMRI. Nature. 453(7197): 869-878.

Lv J, Jiang X, Li X, Zhu D, Zhang S, Zhao S, Chen H, Zhang T, Hu X, Han J, Ye J, Guo L, Liu T. 2015a. Holistic Atlases of Functional Networks and Interactions Reveal Reciprocal Organizational Architecture of Cortical Function. IEEE Transactions on Biomedical Engineering. 62(4): 1120-1131.

Lv J, Jiang X, Li X, Zhu D, Chen H, Zhang T, Zhang S, Hu X, Han J, Huang H, Zhang J, Guo L, Liu T. 2015b. Sparse representation of whole-brain FMRI signals for identification of functional networks. Medical image analysis. 20(1): 112-134.

Lv J, Jiang X, Li X, Zhu D, Zhao S, Zhang T, Hu X, Han J, Guo L, Li Z, Coles C, Hu X, Liu T. 2015c. Assessing effects of prenatal alcohol exposure using group-wise sparse representation of fMRI data. Psychiatry Res. 233:254–68.

Lyon D C, Kaas J H. 2002. Connectional evidence for dorsal and ventral V3, and other extrastriate areas in the prosimian primate, Galago garnetti. Brain, behavior and evolution. 59(3): 114-129.

Mairal J, Bach F, Ponce J, Sapiro G. 2010. Online learning for matrix factorization and sparse coding. The Journal of Machine Learning Research. 11:19-60.

Mantini D, Gerits A, Nelissen K, Durand JB, Joly O, Simone L, Sawamura H, Wardak C, Orban GA, Buckner RL, Vanduffel W. 2011. Default mode of brain function in monkeys. The Journal of Neuroscience. 31(36):2954-12962.

McCormack K, Howell BR, Guzman D, Villongco C, Pears K, Kim H, Gunnar MR, Sanchez MM. 2015. The development of an instrument to measure global dimensions of maternal care in rhesus macaques (Macaca mulatta). American journal of primatology. 77(1), 20-33.

Mori S, Zhang J. 2006. Principles of diffusion tensor imaging and its applications to basic neuroscience research. Neuron. 51(5): 527-539.

Oikonomou VP, Blekas K, Astrakas L. 2012. A sparse and spatially constrained generative regression model for fMRI data analysis. IEEE Transactions on Biomedical Engineering. 59(1): 58-67.

Ogawa S, Tank DW, Menon R, Ellermann JM, Kim SG, Merkle H, Ugurbil K. 1992. Intrinsic signal changes accompanying sensory stimulation: functional brain mapping with magnetic resonance imaging. Proceedings of the National Academy of Sciences. Jul 1;89(13):5951-5.

Palm RB. 2012. Prediction as a candidate for learning deep hierarchical models of data. Technical University of Denmark.

Park HJ, Friston K. 2013. Structural and functional brain networks: from connections to cognition. Science. Nov 1;342(6158):1238411.

Passingham R. 2009. How good is the macaque monkey model of the human brain?. Current opinion in neurobiology. 19(1): 6-11.

Passingham R E, Stephan K E, Kötter R. 2002. The anatomical basis of functional localization in the cortex. Nature Reviews Neuroscience. 3(8): 606-616.

Paxinos G, Franklin KBJ. 2004. The mouse brain in stereotaxic coordinates. Gulf Professional Publishing.

Pessoa L. 2012. Beyond brain regions: Network perspective of cognition–emotion interactions. Behavioral and Brain Sciences. 35(03): 158-159.

Preuss T M, Goldman‐Rakic PS. 1991. Architectonics of the parietal and temporal association cortex in the strepsirhine primate Galago compared to the anthropoid primate Macaca. Journal of Comparative Neurology. 310(4): 475-506.

Rettmann M E, Han X, Xu C, et al. 2002. Automated sulcal segmentation using watersheds on the cortical surface. NeuroImage, 15(2): 329-344.

Rohlfing T, Kroenke CD, Sullivan EV, Dubach MF, Bowden DM, Grant KA, Pfefferbaum A. 2012. The INIA19 template and NeuroMaps atlas for primate brain image parcellation and spatial normalization. Frontiers in neuroinformatics. 6: 27.

Salakhutdinov R, Larochelle H. 2010. Efficient learning of deep Boltzmann machines. Proceedings of the Thirteenth International Conference on Artificial Intelligence and Statistics. 693-700.

Schmahmann JD, Pandya DN, Wang R, Dai G, D'arceuil HE, de Crespigny AJ, Wedeen VJ. 2007. Association fibre pathways of the brain: parallel observations from diffusion spectrum imaging and autoradiography. Brain. Feb 9;130(3):630-53.

Shen D, Davatzikos C. 2002. HAMMER: hierarchical attribute matching mechanism for elastic registration. IEEE transactions on medical imaging. 21(11): 1421-1439.

Smolensky P. 1986. Information processing in dynamical systems: Foundations of harmony theory. COLORADO UNIV AT BOULDER DEPT OF COMPUTER SCIENCE.

Schoenemann PT. 2006. Evolution of the size and functional areas of the human brain. Annu. Rev. Anthropol.. Oct 21;35:379-406.

Sereno MI, Tootell RB. 2005. From monkeys to humans: what do we now know about brain homologies?. Current opinion in neurobiology. Apr 30;15(2):135-44.

Sporns O, Tononi G, Kötter R. 2005. The human connectome: a structural description of the human brain. PLoS computational biology. Sep 30;1(4):e42.

Sui J, Adali T, Yu Q, et al. 2012. A review of multivariate methods for multimodal fusion of brain imaging data. Journal of neuroscience methods. 204(1): 68-81.

Stankiewicz P, Lupski J R. 2010. Structural variation in the human genome and its role in disease. Annual review of medicine. 61: 437-455.

Shi Y, Budin F, Yapuncich E, Rumple A, Young JT, Payne C, Zhang X, Hu X, Godfrey J, Howell B, Sanchez, MM, Styler MA. 2017. UNC-Emory Infant Atlases for Macaque Brain Image Analysis: Postnatal Brain Development through 12 Months. Frontiers in Neuroscience. 10, 617.

Uğurbil K, Xu J, Auerbach E J, et al. 2013. Pushing spatial and temporal resolution for functional and diffusion MRI in the Human Connectome Project. Neuroimage. 80: 80-104.

Van Essen D C, Smith S M, Barch D M, et al. 2013. The WU-Minn human connectome project: an overview. Neuroimage. 80: 62-79.

Van Essen DC, Glasser MF, Dierker DL, Harwell J. 2011. Cortical parcellations of the macaque monkey analyzed on surface-based atlases. Cerebral Cortex. bhr290.

Van Essen DC, Lewis JW, Drury HA, Hadjikhani N, Tootell RB, Bakircioglu M, Miller MI. 2001. Mapping visual cortex in monkeys and humans using surface-based atlases. Vision research. 41(10): 1359-1378.

Van Essen DC. 2004. Surface-based approaches to spatial localization and registration in primate cerebral cortex. Neuroimage. 23: S97-S107.

Van Essen DC. 2005. A population-average, landmark-and surface-based (PALS) atlas of human cerebral cortex. Neuroimage. Nov 15;28(3):635-62.

Von Der Malsburg C. 1994. The correlation theory of brain function. InModels of neural networks. Springer, New York, pp. 95-119.

Wang J, Zuo X, et al. 2013. Disrupted functional brain connectome in individuals at risk for Alzheimer's disease. Biological psychiatry. Mar 1;73(5):472-81.

Wang Q, Chen L, Yap P T, et al. 2010. Groupwise registration based on hierarchical image clustering and atlas synthesis. Human brain mapping. 31(8): 1128-1140.

Woolrich M W, Jbabdi S, Patenaude B, Chappell M, Makni S, Behrens T, Beckmann C, Jenkinson M, Smith S M. 2009. Bayesian analysis of neuroimaging data in FSL. NeuroImage. 45:S173-86.

Wen Z, Yin W, Zhang Y. 2012. Solving a low-rank factorization model for matrix completion by a nonlinear successive over-relaxation algorithm. Mathematical Programming Computation: 1-29.

Yuan Y, Jiang X, Zhu D, Chen H, Li K, Lv P, Yu X, Li X, Zhang S, Zhang T, Hu X, Han J, Guo L, Liu T. 2013. Meta-analysis of functional roles of DICCCOLs. Neuroinformatics. 11(1): 47-63.

Zilles K, Armstrong E, Schleicher A, Kretschmann HJ. 1988. The human pattern of gyrification in the cerebral cortex. Anatomy and embryology. Nov 1;179(2):173-9.

Zhang D, Guo L, Zhu D, Li K, Li L, Chen H, Zhao Q, Hu X, Liu T. 2013. Diffusion tensor imaging reveals evolution of primate brain architectures. Brain Structure and Function. 218(6): 1429-1450.

Zhang X, Li C. 2013. Quantitative MRI measures in SIV-infected macaque brains. Journal of clinical & cellular immunology.

Zhang S, Jiang X, Liu T. 2017a. Joint Representation of Connectome-Scale Structural and Functional Profiles for Identification of Consistent Cortical Landmarks in Human Brains, International Conference on Medical Image Computing and Computer-Assisted Intervention. Springer, Cham. 398-406.

Zhang S, Li X, Lv J, et al. 2013. Sparse representation of higher-order functional interaction patterns in task-based FMRI data. International Conference on Medical Image Computing and Computer-Assisted Intervention. Springer, Berlin, Heidelberg, 626-634.

Zhang S, Li X, Lv J, et al. 2016. Characterizing and differentiating task-based and resting state fMRI signals via two-stage sparse representations. Brain imaging and behavior. 10(1): 21-32.

Zhang S, Zhao Y, Jiang X, et al. 2017b. Joint representation of consistent structural and functional profiles for identification of common cortical landmarks. Brain Imaging and Behavior. 1-15.

Zhang S, Zhang T, Li X, Guo L, Liu T. 2018a. Joint Representation of Cortical Folding, Structural Connectivity and Functional Networks. ISBI.

Zhang S, Liu T, Zhu D, 2018b. Exploring Fiber Skeletons via Joint Representation of Functional Networks and Structural Connectivity, MICCAI.

Zhang T, Zhu D, Jiang X, et al. 2016. Group-wise consistent cortical parcellation based on connectional profiles. Medical image analysis. 32: 32-45.

Zhang T, Guo L, Li G, Nie J, Liu T. 2009. Parametric representation of cortical surface folding based on polynomials. Medical Image Computing and Computer-Assisted Intervention–MICCAI. 184-91.

Zhao S, Han J, Lv J, et al. 2015. Supervised dictionary learning for inferring concurrent brain networks. IEEE transactions on medical imaging. 34(10): 2036-2045.

Zhao Y, Chen H, Li Y, et al. 2016. Connectome-scale group-wise consistent resting-state network analysis in autism spectrum disorder. NeuroImage: Clinical. 12: 23-33.

Zhao Y, Dong Q, Chen H, Iraji A, Li Y, Makkie M, Kou Z, Liu T. 2017a. Constructing fine-granularity functional brain network atlases via deep convolutional autoencoder. Medical image analysis. Dec 1;42:200-11.

Zhao Y, Dong Q, Zhang S, Zhang W, Chen H, Jiang X, Guo L, Hu X, Han J, Liu T. 2017b. Automatic Recognition of fMRI-derived Functional Networks using 3D Convolutional Neural Networks. IEEE Transactions on Biomedical Engineering. Jun 15.

Zhao Y, Ge F, Liu T. 2018. Automatic Recognition of Holistic Functional Brain Networks Using Iteratively Optimized Convolutional Neural Networks (IO-CNN) with Weak Label Initialization, in press, Medical Image Analysis.

Zhu D, Li K, Guo L, et al. 2012a. DICCCOL: dense individualized and common connectivity-based cortical landmarks. Cerebral cortex. 23(4): 786-800.

Zhu D, Li X, Jiang X, et al. 2013. Exploring high-order functional interactions via structurally-weighted LASSO models. IPMI. Springer, Berlin, Heidelberg: 13-24.

Zhu D, Li K, Terry D P, et al. 2014a. Connectome‐scale assessments of structural and functional connectivity in MCI. Human brain mapping, 35(7): 2911-2923.

Zhu D, Zhang T, Jiang X, et al. 2014b. Fusing DTI and fMRI data: a survey of methods and applications. NeuroImage. 102: 184-191.

Zhu D, Li K, Faraco C, Deng F, Zhu D, Jiang X, Chen H, Guo L, Miller S, Liu T. 2011. Discovering dense and consistent landmarks in the brain. Information Processing in Medical Imaging. Springer Berlin Heidelberg. 97-110.

Zhu D, Li K, Faraco C C, et al. 2012b. Optimization of functional brain ROIs via maximization of consistency of structural connectivity profiles. NeuroImage, 59(2): 1382-1393.

Appendix A

Supplemental Materials for Chapter 3

JOINT REPRESENTATION OF CONSISTENT STRUCTURAL AND FUNCTIONAL PROFILES FOR IDENTIFICATION OF COMMON CORTICAL LANDMARKS

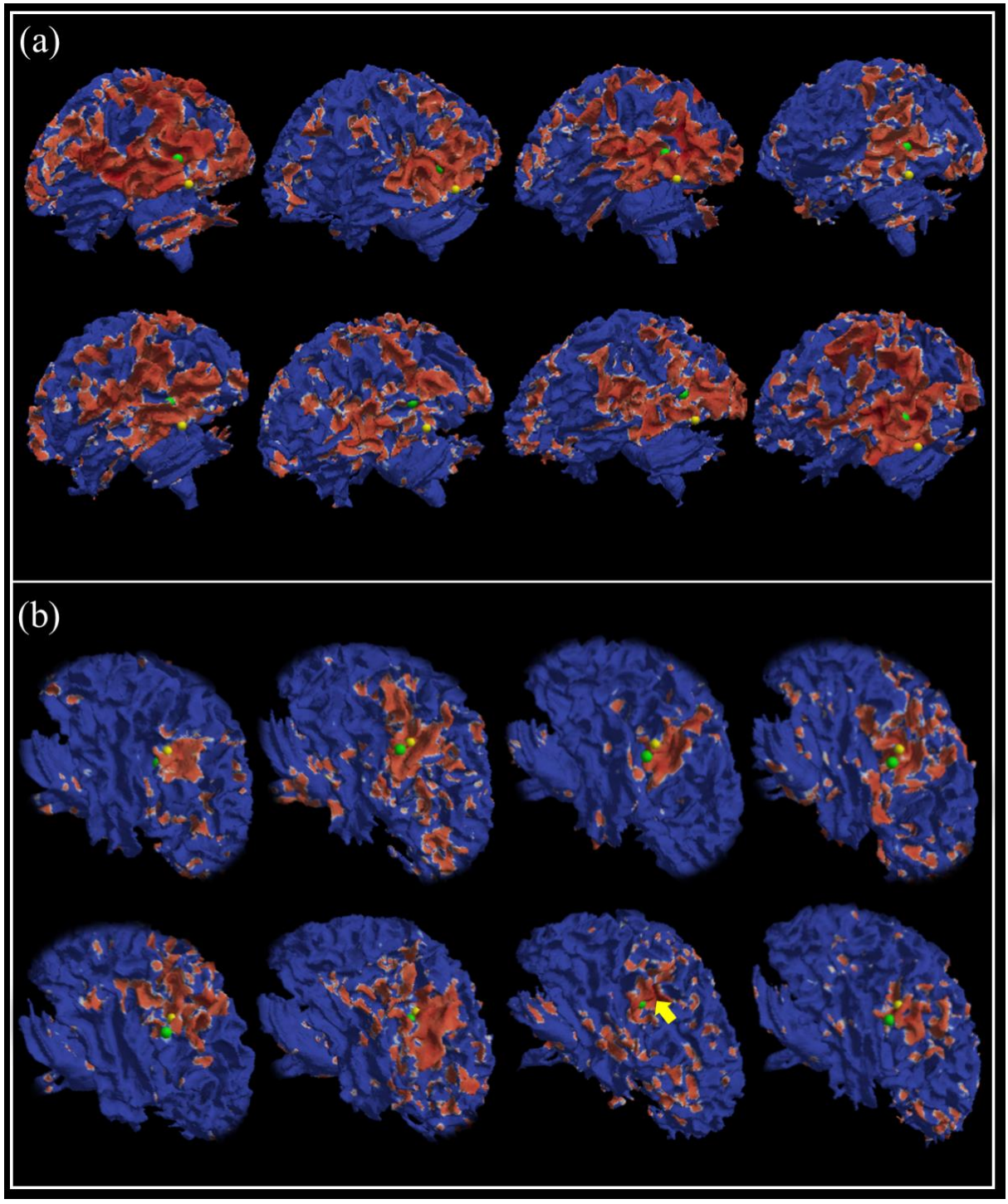

Figure A.1. Two examples of the landmarks before and after optimization. (a) is corresponding to S1 network in Figure 3.3 in the main text, and (b) is corresponding to M5 network in Figure 3.3 in the main text.

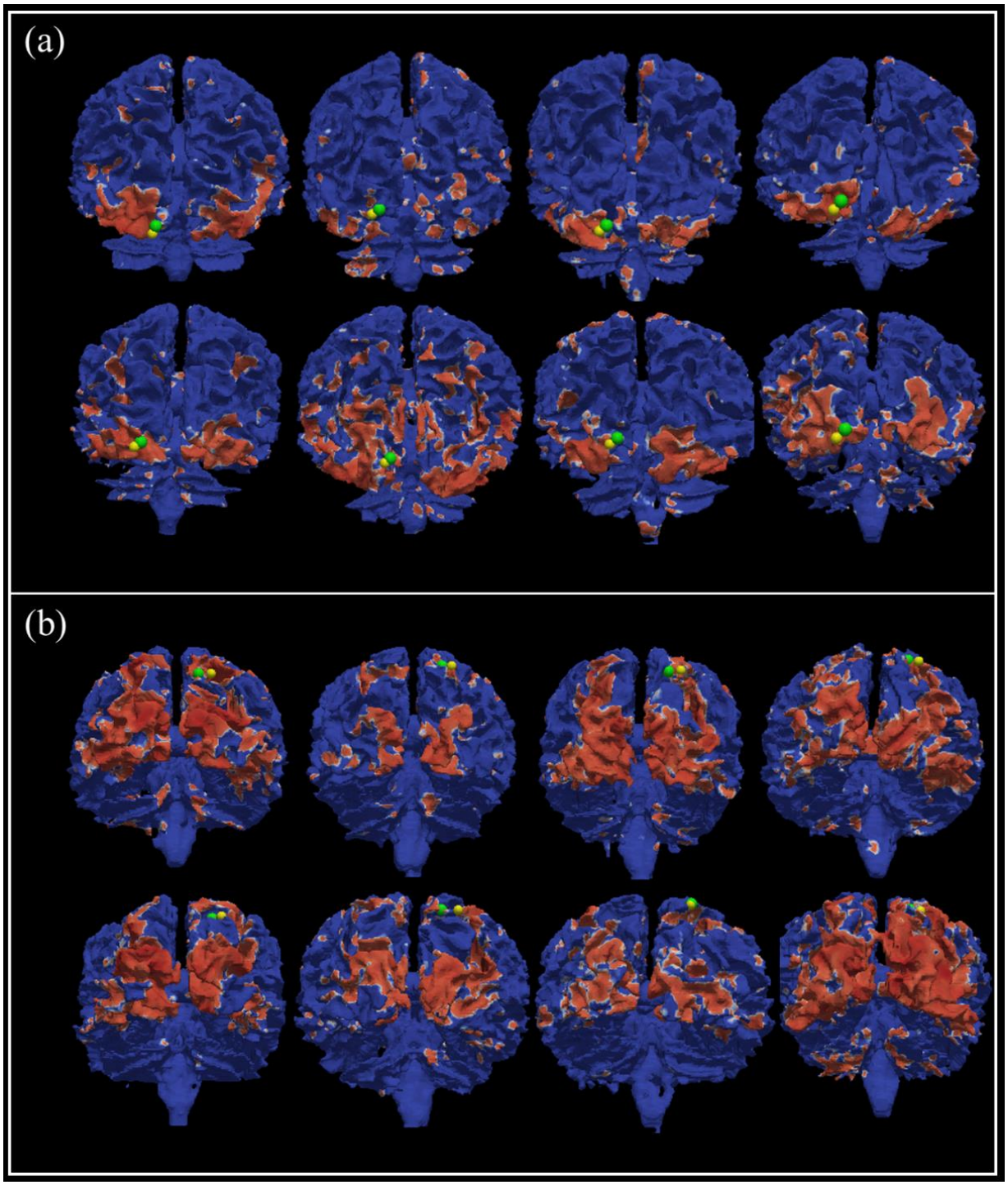

Figure A.2. Two examples of the landmarks before and after optimization. (a) is corresponding to E3 network in Figure 3.3 in the main text, and (b) is corresponding to R2 network in Figure 3.3 in the main text.

Table A.1. The locations of the 55 consistent cortical landmarks in MNI standard space (mm).

Index	x	y	z	Structure
1	-6	-91	-5	Left Cerebrum. Occipital Lobe. Lingual Gyrus.
2	13	-95	-2	Right Cerebrum. Occipital Lobe. Lingual Gyrus.
3	-10	-97	-6	Left Cerebrum. Occipital Lobe. Lingual Gyrus.
4	-21	-85	-13	Left Cerebrum. Occipital Lobe. Fusiform Gyrus. Brodmann area 19.* Fusiform Gyrus.*
5	10	-86	-8	Right Cerebrum. Occipital Lobe. Lingual Gyrus. Brodmann area 18.*
6	-53	-16	-26	Left Cerebrum. Temporal Lobe. Inferior Temporal Gyrus.
7	-33	38	-12	Left Cerebrum. Frontal Lobe. Sub-Gyral.
8	-48	-35	27	Left Cerebrum. Parietal Lobe. Inferior Parietal Lobule.
9	18	-66	32	Right Cerebrum. Occipital Lobe. Precuneus.
10	44	-54	29	Right Cerebrum. Temporal Lobe. Supramarginal Gyrus.
11	-20	-29	42	Left Cerebrum. Limbic Lobe. Cingulate Gyrus.
12	-51	-5	-11	Left Cerebrum. Temporal Lobe. Superior Temporal Gyrus. Brodmann area 38.*
13	51	-24	2	Right Cerebrum. Temporal Lobe. Superior Temporal Gyrus.
14	25	-34	46	Right Cerebrum. Parietal Lobe. Sub-Gyral.
15	-51	-12	-2	Left Cerebrum. Temporal Lobe. Superior Temporal Gyrus. Brodmann area 22.*
16	43	-20	2	Right Cerebrum. Sub-lobar. Insula. Brodmann area 13
17	-10	4	42	Left Cerebrum. Limbic Lobe. Cingulate Gyrus. Brodmann area 24
18	-30	-70	28	Left Cerebrum. Temporal Lobe. Sub-Gyral.
19	-4	-86	2	Left Cerebrum. Occipital Lobe. Lingual Gyrus.
20	36	-81	16	Right Cerebrum. Occipital Lobe. Middle Occipital Gyrus.
21	-15	-92	-11	Left Cerebrum. Occipital Lobe. Lingual Gyrus. Brodmann area 18.*
22	-36	-71	-15	Left Cerebrum. Occipital Lobe. Fusiform Gyrus.*
23	-13	-59	42	Left Cerebrum. Parietal Lobe. Precuneus.
24	15	-72	36	Right Cerebrum. Occipital Lobe. Cuneus. Brodmann area 7.
25	41	-79	-17	Right Cerebellum. Posterior Lobe. Declive. Occipital Lobe. Fusiform Gyrus.
26	-50	-59	-22	Left Cerebellum. Posterior Lobe. Declive.
27	-31	-82	13	Left Cerebrum. Occipital Lobe. Middle Occipital Gyrus.
28	11	-71	34	Right Cerebrum. Occipital Lobe. Cuneus.
29	45	-57	-7	Right Cerebrum. Occipital Lobe. Sub-Gyral.
30	-41	-61	-16	Left Cerebrum. Temporal Lobe. Fusiform Gyrus.
31	15	-95	-8	Right Cerebrum. Occipital Lobe. Inferior Occipital Gyrus. Brodmann area 17. Lingual Gyrus.
32	-41	-45	31	Left Cerebrum. Parietal Lobe. Supramarginal Gyrus.
33	-14	-9	47	Left Cerebrum. Frontal Lobe. Sub-Gyral.
34	-26	-84	2	Left Cerebrum. Occipital Lobe. Sub-Gyral.
35	-10	-92	-6	Left Cerebrum. Occipital Lobe. Lingual Gyrus.
36	9	-97	6	Right Cerebrum. Occipital Lobe. Cuneus. Brodmann area 17.
37	10	-97	-3	Right Cerebrum. Occipital Lobe. Lingual Gyrus.
38	-29	-51	39	Left Cerebrum. Parietal Lobe. Sub-Gyral.
39	-18	-86	-13	Left Cerebrum. Occipital Lobe. Lingual Gyrus. Brodmann area 18.
40	9	-90	-6	Right Cerebrum. Occipital Lobe. Lingual Gyrus.

41	19	-95	-11	Right Cerebrum. Occipital Lobe. Lingual Gyrus. Brodmann area 18.
42	14	-97	-6	Right Cerebrum. Occipital Lobe. Lingual Gyrus. Inferior Occipital Gyrus. Brodmann area 17
43	-35	-74	-17	Left Cerebellum. Posterior Lobe. Declive.
44	43	-77	-18	Right Cerebellum. Posterior Lobe. Declive.
45	10	-69	28	Right Cerebrum. Parietal Lobe. Precuneus.
46	49	-65	19	Right Cerebrum. Temporal Lobe. Middle Temporal Gyrus.
47	-44	-25	32	Left Cerebrum. Parietal Lobe. Inferior Parietal Lobule. Postcentral Gyrus.
48	-4	-16	37	Left Cerebrum. Limbic Lobe. Cingulate Gyrus. Brodmann area 24.
49	-58	-11	-21	Left Cerebrum. Temporal Lobe. Inferior Temporal Gyrus. Brodmann area 21.
50	59	-25	2	Right Cerebrum. Temporal Lobe. Superior Temporal Gyrus.
51	-46	-44	26	Left Cerebrum. Parietal Lobe. Inferior Parietal Lobule.
52	-35	7	27	Left Cerebrum. Frontal Lobe. Inferior Frontal Gyrus.
53	21	-77	28	Right Cerebrum. Occipital Lobe. Cuneus. Brodmann area 18
54	40	28	-25	Right Cerebrum. Frontal Lobe. Inferior Frontal Gyrus. Brodmann area 47.
55	54	-56	-25	Right Cerebellum. Posterior Lobe. Declive.

Table A.2. The functions of the 55 consistent cortical landmarks in MNI standard space (mm).

Index	x	y	z	Function
1	-6	-91	-5	Perception. Vision. Shape. Cognition. Motion.
2	13	-95	-2	Emotion. Cognition. Attention.
3	-10	-97	-6	Action. Execution. Speech. Cognition. Language. Emotion. Perception. Gustation.
4	-21	-85	-13	Emotion. Disgust. Cognition. Perception. Vision. Shape.
5	10	-86	-8	Cognition. Language. Speech. Semantics. Perception. Vision. Emotion.
6	-53	-16	-26	Cognition. Memory. Working.
7	-33	38	-12	Cognition. Emotion. Finger Tapping/Button Press. Stroop-Other. Counting/Calculation.
8	-48	-35	27	Perception. Somesthesis. Cognition. Attention. Interoception. Gastrointestinal/Genitourinary (GI/GU)
9	18	-66	32	Perception. Vision
10	44	-54	29	Cognition. Language. Orthography.
11	-20	-29	42	Emotion. Perception. Vision
12	-51	-5	-11	Perception. Vision. Shape. Cognition. Spatial. Language. Speech. Audition. Attention. Memory.
13	51	-24	2	Cognition. Language. Speech. Perception. Vision. Shape. Action. Rest. Emotion. Somatic.
14	25	-34	46	Perception. Audition
15	-51	-12	-2	Cognition. Language. Orthography. Music. Action. Inhibition. Attention.
16	43	-20	2	Emotion
17	-10	4	42	Action. Rest. Language. Semantics. Cognition. Speech.
18	-30	-70	28	Cognition. Language. Semantics. Memory. Explicit. Emotion. Social.
19	-4	-86	2	Cognition. Language. Semantics. Speech.
20	36	-81	16	Action. Observation. Imagination. Cognition. Emotion.
21	-15	-92	-11	Cognition. Language. Semantics. Orthography. Speech. Phonology.
22	-36	-71	-15	Cognition. Language. Orthography. Semantics. Speech
23	-13	-59	42	Emotion. Cognition. Social. Pain. Monitor/Discrimination. Language. Phonology.
24	15	-72	36	Cognition. Memory. Explicit. Perception. Somesthesis. Pain.
25	41	-79	-17	Perception. Vision. Motion. Cognition. Reasoning.
26	-50	-59	-22	Action. Execution. Speech. Cognition. Language. Orthography. Social.
27	-31	-82	13	Perception. Vision. Shape. Cognition. Spatial. Flanker, Finger Tapping/Button Press. Visual Object Identification
28	11	-71	34	Cognition. Memory. Working. Finger Tapping/Button Press. Visual Object Identification. Oddball Discrimination
29	45	-57	-7	Perception. Vision. Shape. Spatial. Language. Action. Observation. Memory. Cognition. Attention. Working. Motion.
30	-41	-61	-16	Cognition. Memory. Working. Perception. Vision. Shape
31	15	-95	-8	Cognition. Language. Orthography. Perception. Vision. Attention. Speech. Semantics.
32	-41	-45	31	Finger Tapping/Button Press. Counting/Calculation.
33	-14	-9	47	Action. Execution. Cognition. Memory. Explicit. Emotion. Perception. Audition.
34	-26	-84	2	Cognition. Memory. Working
35	-10	-92	-6	Interoception. Hunger. Perception. Vision. Shape.
36	9	-97	6	Cognition. Language. Semantics. Reasoning. Perception. Vision
37	10	-97	-3	Perception. Vision. Shape. Action. Rest.
38	-29	-51	39	Cognition. Language. Semantics. Speech. Orthography. Action. Execution. Finger Tapping/Button Press. Emotion Induction. Face Monitor/Discrimination.
39	-18	-86	-13	Cognition. Memory. Explicit.

40	9	-90	-6	Action. Observation. Language. Phonology. Cognition. Speech. Perception. Vision.
41	19	-95	-11	Cognition. Attention. Emotion.
42	14	-97	-6	Perception. Vision. Cognition. Attention. Passive Viewing.
43	-35	-74	-17	Emotion. Disgust. Cognition. Memory. Working. Passive Listening. Sleep.
44	43	-77	-18	Perception. Vision. Shape. Cognition. Attention.
45	10	-69	28	Finger Tapping/Button Press, n-back. Perception. Gustation.
46	49	-65	19	Cognition. Language. Semantics. Speech. Memory. Explicit. Emotion. Social Cognition.
47	-44	-25	32	Action. Rest. Cognition. Language. Orthography.
48	-4	-16	37	Emotion. Cognition. Memory. Explicit. Vestibular Stimulation.
49	-58	-11	-21	Action. Imagination. Cognition. Memory. Explicit. Finger Tapping/Button Press. Emotion Induction. Affective Pictures. Sleep. Passive Listening.
50	59	-25	2	Action. Execution. Speech. Cognition. Language. Execution. Observation. Perception. Audition. Somatic.
51	-46	-44	26	Cognition. Memory. Working.
52	-35	7	27	Emotion. Cognition. Attention.
53	21	-77	28	Perception. Vision. Motion. Action. Execution. Emotion.
54	40	28	-25	Cognition. Language. Speech.
55	54	-56	-25	Cognition. Emotion. Action. Execution.

Appendix B

Supplemental Materials for Chapter 5

DISCOVERING HIERARCHICAL COMMON BRAIN NETWORKS VIA MULTIMODAL DEEP BELIEF NETWORK

Part I.

In the Figure B.1 and Figure B.2, we illustrated where 2800 functional networks come from. Briefly speaking, in the HCP dataset, for each subject, 7 tasks are included, they are "Language", "Social", "Working memory", "Gambling", "Emotion", "Relational" and "Motor". By using online dictionary learning algorithm (ODL), fMRI time series are decomposed into two parts, as illustrated in Figure B.1, one is dictionary matrix and another one is coefficient matrix, for more details, please refer to Lv et al, 2015a. From Lv et al, 2015a, the number of the components is empirically set to 400. Thus, 2800 networks are obtained for one subject, as illustrated in Figure B.2.

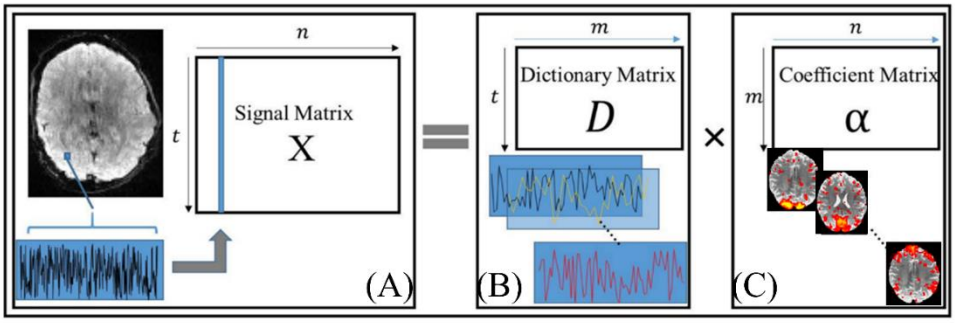

Figure B.1. The framework of applying ODL algorithm onto the fMRI signals. (A) Obtain signals from fMRI images. (B) Dictionary matrix. (C) Coefficient matrix.

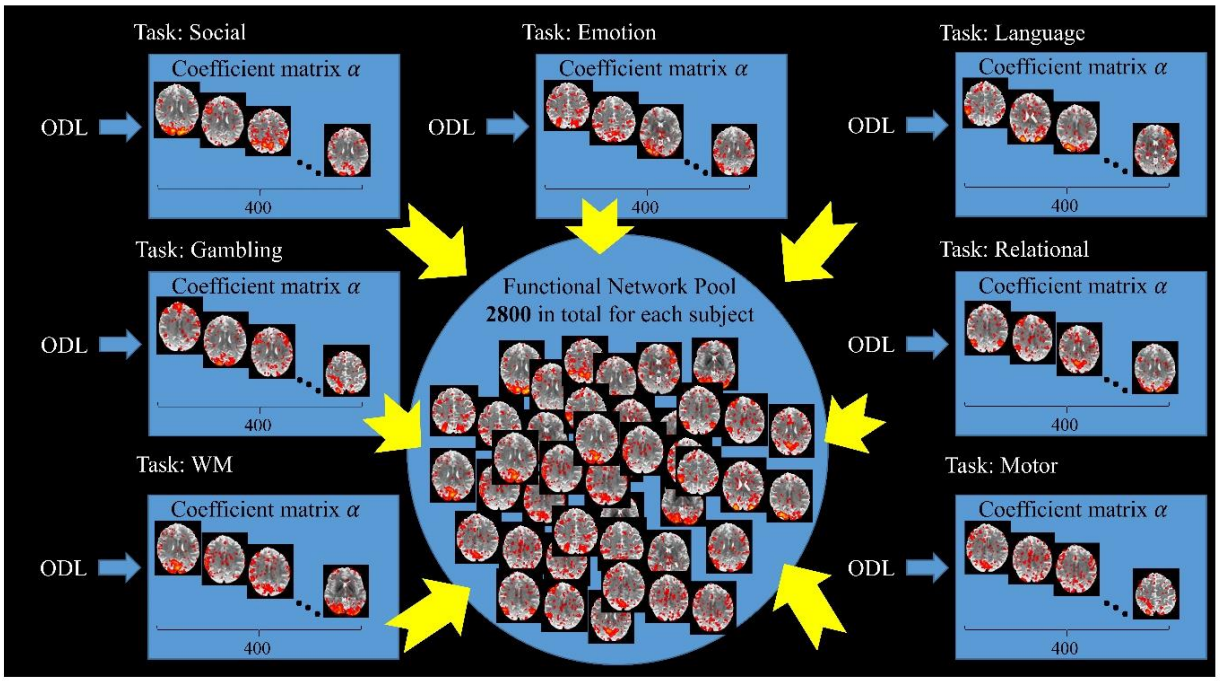

Figure B.2. The composition of 2800 functional networks from one subject.

Part II.

In this part, we show how to generate a functional connectivity map f_i for seed vertex v_i. Two main steps are mentioned in the Section 5.2.4 and they are also shown in the figure below. First step is to pick up all the functional networks (from 2800 functional networks) in which the seed vertex v_i is activated, selected networks are shown in Figure B.3B. Second step is to calculate the intensity of functional connectivity for all the vertices. For each network from Figure B.3B, we record all the activated vertices v_{active}(exclude v_i) and update the counters of all those v_{active} by adding 1. Two examples are shown in Figure B.3D, contours for v_j and v_k are added by 1 separately, because they are the activated vertices from the functional networks in Figure B.3B.

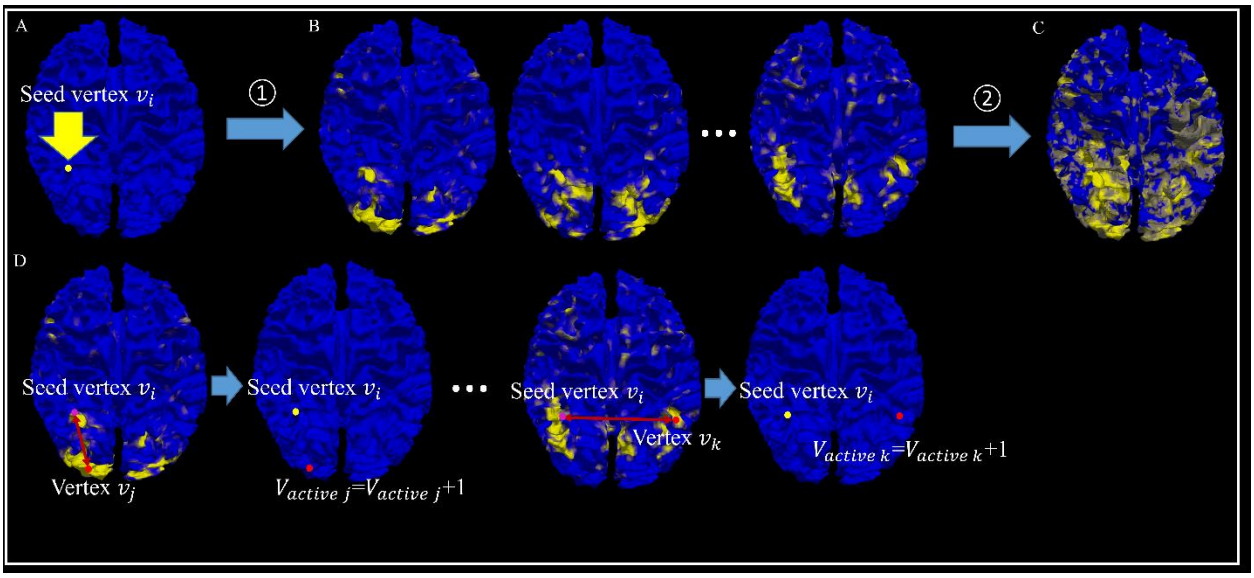

Figure B.3. The process of generating functional connectivity map for one seed vertex. (A) The location of seed vertex. (B) Selected functional networks. Yellow regions on the cortical surface are the activation areas. (C) Functional connectivity map of seed vertex. (D) Two examples about how functional connectivity maps are generated.

Thus, after we go through whole brain vertices for each selected functional network and then go through all the picked up functional networks, the final intensity for each vertex will be recorded by contours, then the functional connectivity map for seed vertex v_i is shown in Figure B.3D.

Next step is using functional trace-map descriptor to describe the seed vertex's functional connectivity map. The details are shown in the Figure B.4. It is worth noting that we will project every direction between seed vertex and activated vertices from the functional connectivity map onto the uniform spherical surface, the intensity of the activated vertex will determine the number of the projection times for this direction (direction between seed vertex and current vertex). In the end, as shown in Figure B.4E, a 144-dimensional histogram vector $tr =$

$[d_1, d_2 \ldots d_{144}]$, containing 144 density values, is used to represent 3D functional connectivity map.

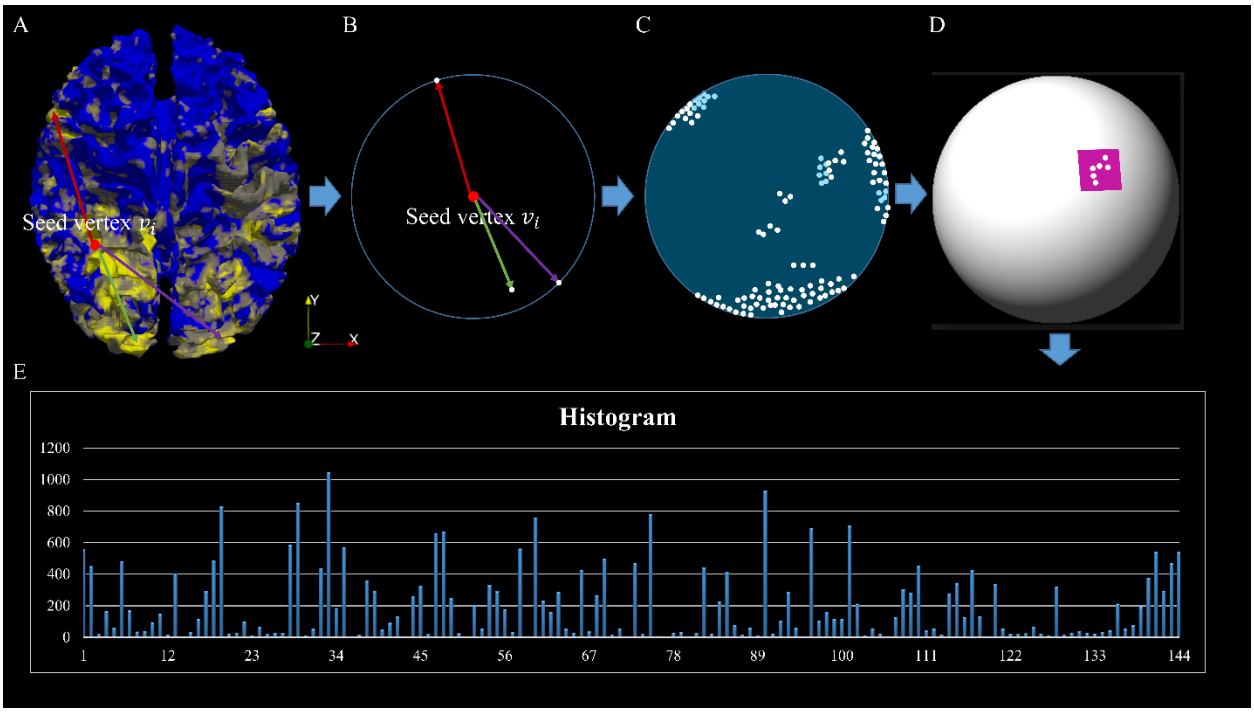

Figure B.4. The process of using functional descriptor to describe functional connectivity maps. (A) Functional connectivity map and its seed vertex. (B) Project each direction on the uniform spherical surface. (C) An example of uniform spherical surface with dots. (D) Divided the surface of the unit sphere into 144 equally area (one area is shown by the purple diamond). Each area contains certain number of dots. (E) The distribution of number of dots in each area.

PART III.

In this section, we evaluated the functional trace-map descriptor. As we mentioned, functional trace-map descriptor can correctly and effectively represent the function connectivity of the seed vertex. We designed two experiments to evaluate our proposed functional trace-map descriptor.

One experiment is to demonstrate the proposed functional trace-map descriptor can preserve major spatial information of the seed vertex. Three different kinds of functional connectivity maps are provided in the Figure B.5. Seed vertex is fixed and functional trace-map descriptor is adopted to describe those functional connectivity maps, then 144-dimensional histogram vectors are used to represent corresponding functional connectivity maps. Based on those 144-dimensional histogram vectors, Pearson correlation values are calculated within and between groups, results are shown in the Table B.1. Based on the Table B.1, it can be inferred that our functional descriptor indeed works to preserve major spatial information of the functional connectivity maps. Functional networks with similar pattern have quite higher correlation coefficient. Less correlation coefficient values will be obtained when the functional connectivity maps are largely different.

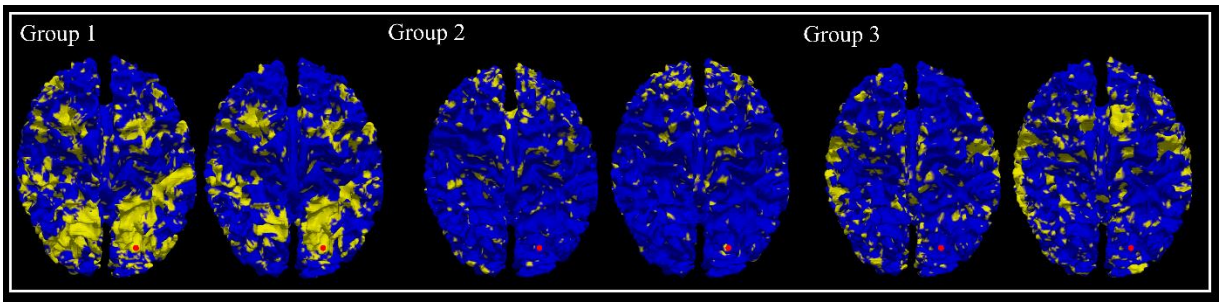

Figure B.5. Three different groups of functional connectivity maps. Each group contains two similar functional connectivity maps; seed vertex is fixed and shown as the red dots.

Table B.1. Correlation within group and between groups of functional connectivity maps from Figure B.5.

In group	Group1	Group2	Group3
Correlation	0.82	0.81	0.81
Between group	Group1&Group2	Group2&Group3	Group1&Group3
Correlation	0.22	0.25	0.35

Another experiment is to test the effectiveness of our functional trace-map descriptor, we randomly chose a subject and all the vertices on the cortical surface are used to obtain their corresponding “function trace-map”, a seed vertex is randomly chosen and other vertices will do the comparison to the seed vertex using the correlation of their “function trace-map”. Results are shown in the Figure B.6. From the Figure B.6B-C, we can infer that most of the “function trace-map” obtained from other vertices have significant differences in comparison with the seed vertex, that is, most of the regions in the cortex are blue. Considering the small neighborhood of the seed vertex we chose, the correlation of functional trace-map between the seed vertex and neighborhood vertices are roughly follow a Gaussian distribution. That is to say, the functional trace-map of a vertex is quite distinctive, which is needed to unambiguously characterize the current vertex.

By designing above mentioned two experiments, we believe that our proposed functional trace-map descriptor has the ability to correctly and effectively represent the features of the functional networks.

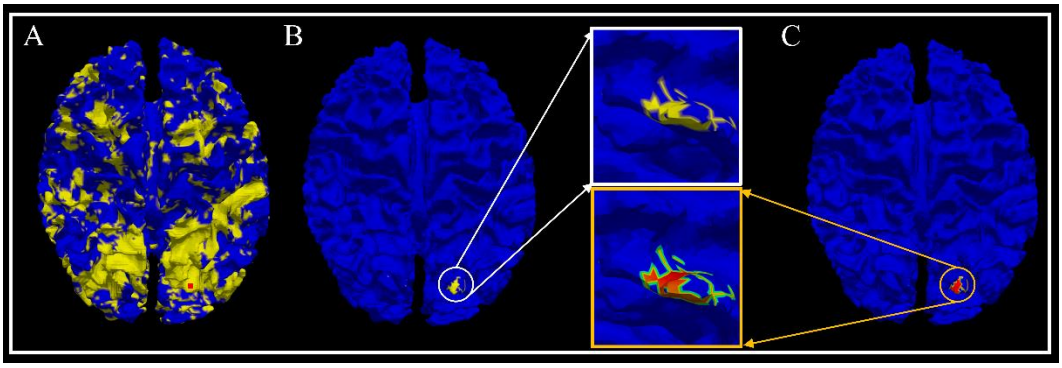

Figure B.6. Validation of the functional trace-map descriptor. (A) Functional connectivity map of the seed vertex (seed vertex is shown in red square). (B) Neighborhood vertices of the seed vertex (shown in the yellow). (C) Correlation of functional trace-map between seed vertex and all other vertices from the cortex. The color bar for C is 0.5 to 1 (green to red), smaller than 0.5 is set to blue.